SIMULATION STUDY OF A COLLOIDAL SYSTEM UNDER THE INFLUENCE OF AN EXTERNAL ELECTRIC FIELD

AHMAD MUSTAFA ALMUDALLAL

SIMULATION STUDY OF A COLLOIDAL SYSTEM UNDER THE INFLUENCE OF AN EXTERNAL ELECTRIC FIELD.

by:

Ahmad Mustafa Almudallal

B.Sc. Physics, Yarmouk University, 2000

M.Sc. Physics, Yarmouk University, 2004

A thesis submitted to the School of Graduate Studies in partial fulfillment of the requirements for the degree of Master of Science.

Department of Physics and Physical Oceanography

Memorial University of Newfoundland.

January 27, 2010

ST. JOHN'S NEWFOUNDLAND

Dedication

First of all, I would like to dedicate my thesis to my native home "PALESTINE"

Also, I would like to dedicate this thesis to my wonderful parents, Mustafa and Amneh, who gave me unconditional love, guidance and support.

Also, I would like to dedicate this thesis to my sister and my brothers and others in my family.

Finally, I dedicate my thesis to Memorial University of Newfoundland, especially the Department of Physics and Physical Oceanography, for giving me this unique opportunity to study in Canada and to do this work.

Acknowledgment

I would like to thank Dr. Saika-Voivod for giving me this unique opportunity to do this exciting work. He patiently guided this work, and he has been excellent supervisor, giving me support, encouragement and help.

Also, I would like to thank the examiners for their critical reading and for their comments and suggestions.

I also would like to thank Dr. Yethiraj for providing me very useful information through group meetings. Special thanks to Mr. Jason Mercer from the Computer Science Department for helping me in computer and software questions.

I express my absolute thankfulness to my father, mother, sister, brothers and others in my family for their support and encouragement in this work.

I would like also to thank my friends in Jordan and Canada and every person who enlightened me.

I hope I did not forget any one, so thanks to all.

Ahmad M. Almudallal, December, 2009.

Contents

List of Figures

List of Tables

Abstract

We perform Monte Carlo simulations to study an electrorheological fluid that consists of spherical dielectric particles in a solution of low dielectric constant under the influence of an external electric field. The electric field induces dipole moments in the colloids that align along to the electric field direction. At a sufficiently high electric field, the dipoles attract each other to form long chains along the electric field direction. The system can then be modeled as a 2D system of interacting disks, where each disk represents a chain of hard sphere dipolar particles viewed along the field axis. The disk-disk interaction varies with chain length, but has the general feature of strong short range attraction and weak long range repulsion. We perform simulations of the 2D fluid across a wide range of temperature and area fraction to study its structural properties and phase behaviour. Our model reproduces the clustered structures seen experimentally

In addition, a novel void phase has been seen by two experimental groups in a low volume fraction regime ($< 1\%$). The simulations of our model indicate that dipolar hard spheres, even with the addition of Yukawa and van der Waals interactions, do not produce the void phase. Further investigations employing toy potentials reveal qualitative features of the potential that can give rise to voids, but physical mechanisms that may produce these features remain speculative.

Key Words: Colloids, Dipolar Rods, Monte Carlo Simulation.

Chapter 1

Introduction

Colloidal suspensions, small particles dispersed within a second medium, are common in everyday life with examples ranging from toothpaste to paint, from milk to quicksand. From these examples we see that colloidal suspensions can exhibit both solid-like and liquid-like behaviour, i.e. support a weak shear on short timescales, while flowing on longer timescales, and therefore fall into the realm of soft condensed matter. From a materials perspective, colloidal suspensions offer a gateway to producing novel materials as the interaction between colloidal particles can often be tuned or manipulated. One recent advance in controlling colloids involves the application of an external electric field that induces a dipolar interaction between the colloidal particles. The interesting phase behaviour of such so-called electrorheological (ER) fluids is the subject of this thesis. In particular, we wish to see to what extent a simple model based on dipolar interaction can qualitatively reproduce the phases seen experimentally.

In this chapter we give a general overview of colloidal suspensions, including a description of some of the interactions that play an important role in dictating the material properties of colloids, as well some of the phenomenology motivating our work. We

conclude this chapter with an overview of the rest of the thesis.

1.1 Colloids

1.1.1 Overview

The first person who recognized the existence of colloidal particles and defined their common properties was Francesco Selmi in 1845. In the 1850s, Michael Faraday extensively studied a colloidal system which contained solid particles in water. Faraday, in his experiments, found that colloidal systems are thermodynamically unstable, since the coagulation process in these systems is irreversible. Also, he concluded that these systems must be stabilized kinetically since they can exist for many years after preparation. Although Selmi and Faraday were the discoverers of colloids, the word "colloid" was still unused at that time. In 1861, Thomas Graham gave the name "Colloid" to these particles [1, 2]. He also deduced the size of colloids from their motion in the solution. He emphasized the low diffusion rates of colloidal particles, and then concluded that the particles are fairly large (larger than 1 nm). On the other hand, the lack of sedimentation of the particles under the influence of gravity implied that these particles had an upper size limit of a few micrometers [1].

The colloidal system consists of two phases. The first phase includes suspended particles distributed in a medium, which is the second phase. Usually, the first phase is called the discontinuous phase or disperse, while the second one is called the continuous phase or dispersion medium. Since the first phase is dispersed in the second phase, the colloidal system may also be called colloidal dispersion or colloidal suspension. However, these two phases could be gas, liquid or solid [3], although some researchers prefer to not call

the system of solid dispersion medium as a colloidal suspension because the suspended particles will not be affected by the Brownian motion. The table below presents various types of colloidal dispersion with some common examples [3]. In addition, colloidal suspensions or colloidal materials are commonly used in daily life, e.g. milk, soap, paints, glue and others are all colloidal suspensions.

Table 1.1: The various types of Colloidal Dispersion with some common examples [3].

Disperse Phase	Dispersion Medium	Technical Name	Common Name
Solid	Gas	Aerosol	Smoke, dust
Liquid	Gas	Aerosol	Fog
Solid	Liquid	Sol or colloidal sol	Suspension, slurry, jelly
Liquid	Liquid	Emulsion	Emulsion
Gas	Liquid	Foam	Foam, froth
Solid	Solid	Solid dispersion	Some alloys and glasses
Liquid	Solid	Solid emulsion	
Gas	Solid	Solid foam	

Basically, colloidal science is a branch of soft condensed matter science. The term "soft condensed matter" is a name for materials which are neither simple liquids nor crystalline solids. Instead, soft materials have properties common to both liquid and solid materials [4]. These common properties lead to the soft materials gaining a new property which is viscoelasticity [4, 5]. The term viscoelasticity is a compound name from two concepts. The first one is viscosity, associated with liquids, and the second one is elasticity, which is associated with solids. The viscous property in soft materials is dominant at long time scales, on which the materials behave as liquids, while elasticity

is dominant at short time scales, during which the materials behave like solids.

1.1.2 Interactions in a Colloidal System

The definition of a colloidal system or colloidal dispersion can be concluded from section (1.1) as a heterogeneous system of particles of a size around 10μm or less that are dispersed in a solution. The colloidal dispersion is considered stable whenever the particles are suspended in the solution and are not aggregated, and maintaining stability is often a primary concern in colloidal science [4]. Common forces in colloidal suspensions that tend to destabilize the suspension are gravity, Van der Waals interactions, while Brownian motion, and electrostatic forces and polymer stabilization tend to improve stability. In addition to these forces, we will discuss drag forces and depletion interactions [1, 2, 4].

Gravity and Brownian Motion

Particles immersed in a fluid feel a buoyant force in the presence of gravity. This is no different for colloidal particles in a suspension. If the particles are less dense than the solution, they will tend to rise; denser particles will sink. When the sedimentation process is not the object of study, a stable suspension requires that the density of the continuous phase closely match the density of the discontinuous phase. While precise density matching may not always be achievable, Brownian motion tends to work against the sedimenting affects of gravity and makes the system more homogeneous. Brownian motion results from effectively random collisions between solution molecules and the colloidal particles, and gives rise to the tendency for particles to diffuse throughout the suspension. The strength of the Brownian motion depends inversely on the particle's size. If the dispersed particles are small enough, Brownian motion can overcome the

gravitational force and effectively prevent sedimentation. On the other hand, Brownian motion promotes collisions between colloidal particles themselves. In the presence of strong, but short-range attractions, this will aid in the aggregation of particles into clusters, destabilizing the suspension. To summarize, Brownian motion and gravitational forces must be considered together when discussing colloidal dispersion stability with respect to sedimentation, but other forces may lead to aggregation [2, 4].

Drag Force

At the same time, drag force plays a significant role against the gravitational force to keep the system stabilized. Dropping spherical, denser particles into a solution drives these particles to accelerate down under the gravitational force. If the solution is viscous, an upward frictional force affects these spherical particles. This frictional force is called the Stokes force, and it was derived by George Stokes from solving the Navier-Stokes equation in 1851. The Stokes force for one colloid is given by [2, 4],

$$F_s = 6\pi\eta a v \ , \tag{1.1}$$

where F_s, η, a and v are drag force, viscosity, colloid's radius and the colloid's velocity in the solution, respectively. Falling particles will reach a terminal velocity v_t, where gravitational and drag forces balance [4]. The gravitational force for a single colloid in a solution is given by,

$$F_g = \frac{4}{3}\pi a^3 \Delta\rho g \ , \tag{1.2}$$

where $\Delta\rho$ is the density difference between the colloids and the solution, and g is the constant acceleration due to gravity. The terminal velocity can be found from Eq. 1.1 and Eq. 1.2, and is given by,

$$v_t = \frac{2a^2\Delta\rho g}{9\eta} \ . \tag{1.3}$$

Van der Waals Interaction

One common interaction in colloidal suspensions is the van der Waals interaction. This interaction is attractive and it always operates between molecules. It arises from electron motion around the nuclei that allows for molecules to induce dipole moments within each other. The van der Waals force is quantum mechanical in nature, and it appears even if the atoms have no permanent dipole moment. The resultant interaction varies as the inverse sixth power of the separation r, as given by,

$$V(r) = -\frac{3}{4}\left(\frac{1}{4\pi\epsilon_0}\right)^2 \frac{\alpha^2}{r^6}\hbar\omega\,, \tag{1.4}$$

where ϵ_0, α and $\hbar\omega$ are dielectric constant of free space, polarizability, and ionization energy, respectively [1, 4].

For macroscopic bodies, the van der Waals interaction is the sum of all the induced-dipole - induced-dipole interactions between constituent atoms of each body. The total interaction energy becomes a function of the distance h between two bodies and is obtained by integrating over all interacting atomic pairs,

$$U(h) = \int\int -\frac{C}{|\vec{r}_1 - \vec{r}_2|^6}\rho_1 dV_1 \rho_2 dV_2, \tag{1.5}$$

where we have assumed for simplicity two identical bodies composed of the same atomic species, ρ_i is the (atomic) number density of, $\vec{r}_i$ is the position within, and dV_i a volume element of body i. The prefactor C is constant for the material given by

$$C = \frac{3}{4}\left(\frac{1}{4\pi\epsilon_0}\right)^2 \alpha^2\hbar\omega. \tag{1.6}$$

For two macroscopic spherical bodies of radii R_1 and R_2 and large separation, the van der Waals potential in Eq. 1.5 can be simplified to the following formula,

$$U(h) = -\left(\frac{4}{3}\right)^2 R_1^3 R_2^3 A(h + R_1 + R_2)^{-6}, \tag{1.7}$$

where $A = \pi^2 \rho_1 \rho_2 C$ is called the Hamaker constant with dimensions of energy, and h is the closest surface to surface distance between the spheres. At very short distances ($h << R_1, R_2$), the van der Waals interaction becomes more significant and it varies as the inverse power of h, as given by [1],

$$U(h) = -A\frac{R_1 R_2}{6(R_1 + R_2)}\frac{1}{h}. \tag{1.8}$$

In general, the Hamaker constant is a material property, and it has a value about $10^{-19}J$ for most materials. For two colloidal particles, the presence of the dispersion medium effectively changes the Hamaker constant, although the force remains attractive for two bodies of the same material. Indeed, the strength of the van der Waals interaction is directly proportional to the difference in the refraction index between the colloids and the solution, as seen in the following formula [6],

$$U(h) \approx -3k_B T\frac{\sqrt{3}h\nu}{4}\frac{\left(n_p^2 - n_s^2\right)^2}{\left(n_p^2 + 2n_s^2\right)^{3/2}}\frac{R^6}{r^6} \tag{1.9}$$

where h is the Planck's constant, ν is the absorption frequency of the medium, n_p and n_s are the refraction indices of the particles and the solution, respectively. R is the particles' radius, and r is the distance between any two particles in the system. Usually, experimentalists reduce the van der Waals interaction by matching the refraction index of the solution and colloids [6, 7]. Although fairly weak, especially at larger ranges, the van der Waals interaction is the primary cause of aggregation.

Electrostatic Interaction (Yukawa Interaction)

In solution, a colloidal particle's surface may become charged as surface chemical groups become ionized. These charged surfaces introduce an electrostatic interaction between colloids. The Coulomb interaction between the colloids is screened by free ions in solution.

The charged surfaces attract the free ions from the solution to form a layer of counter-ions near the charged surface. In particular, an electrostatic force will arise between the colloids and the screening counter-ions. In the following, we introduce this interaction in detail for one dimension for simplicity, and then quote results for three dimensions.

In the beginning, we need to determine the net charge of the counter-ions $\rho(x)$ at a distance x from the colloid's surface [4], which for this calculation is modeled as an infinite plane. Actually, $\rho(x)$ can be found by solving Poisson equation, which is given in Eq. 1.10 for the counter-ions at a distance x from the colloid's surface,

$$\rho(x) = -\epsilon_r \, \epsilon_0 \left(\frac{d^2\psi(x)}{dx^2} \right) , \tag{1.10}$$

where ϵ_r and ϵ_0 are relative dielectric permittivity of the solution and the permittivity of free space, respectively, and $\psi(x)$ is the electrostatic potential at a distance x away from the surface. On the other hand, the net charge of the counter-ions at a distance x from the surface can be determined from the Boltzmann distribution for counter-ions in solution $n(x)$, as follows,

$$\rho(x) = n(x) \; ze = n_0 \; ze \; \exp\left(\frac{-ze \; \psi(x)}{k_B \; T} \right) , \tag{1.11}$$

where n_0 and ze are the ionic concentration in the bulk solution without colloids and the charge of the ions, respectively, and k_B and T are Boltzmann constant and temperature, respectively. The ionic solution is also known as an electrolyte, where the counter-ions include both positive and negative ions. Hence, the ionic concentration for the two kinds of charges can be expressed as,

$$n_{\pm}(x) = n_0 \; \exp\left(\mp \frac{ze \; \psi(x)}{k_B T} \right) . \tag{1.12}$$

The net charge density of the counter-ions for the positive and negative ions is given by,

$$\rho(x) = n_0 \; ze \; \left[\exp\left(\frac{ze \; \psi(x)}{k_B T} \right) + \exp\left(\frac{-ze \; \psi(x)}{k_B T} \right) \right] . \tag{1.13}$$

Combining Eq. 1.10 and Eq. 1.13 gives the Poisson-Boltzmann equation for the potential,

$$\begin{aligned}\frac{d^2\psi(x)}{dx^2} &= \left(\frac{n_0\, ze}{\epsilon_r\, \epsilon_0}\right)\left[\exp\left(\frac{ze\,\psi(x)}{k_BT}\right) - \exp\left(\frac{-ze\,\psi(x)}{k_BT}\right)\right] \\ &= \frac{2\, n_0\, ze}{\epsilon\, \epsilon_0}\sinh\left(\frac{ze\,\psi(x)}{k_BT}\right). \end{aligned} \tag{1.14}$$

The Debye-Hückel approximation supposes that the potential $\psi(x)$ is small, and then $\sinh(ze\,\psi(x)/k_BT) \approx (ze\,\psi(x)/k_BT)$. So, Eq. 1.14 can be written as,

$$\begin{aligned}\frac{d^2\psi(x)}{dx^2} &= \frac{2n_0z^2e^2}{\epsilon_r\, \epsilon_0\, k_BT}\psi(x) \\ &= k^2\psi(x), \end{aligned} \tag{1.15}$$

where k^{-1} is called Debye screening length, and k has the value,

$$k = \left(\frac{2\, n_0z^2e^2}{\epsilon_r\, \epsilon_0\, k_BT}\right)^{1/2}. \tag{1.16}$$

Eq. 1.15 is a second order differential equation, and it has simple solution as follows,

$$\psi(x) = A\exp(-kx) + B\exp(kx). \tag{1.17}$$

Using the fact that $\psi(x)$ and $d\psi(x)/dx$ go to zero as x goes to infinity will reduce Eq. 1.17 to the following equation,

$$\begin{aligned}\psi(x) &= \psi_0\exp(-kx) \\ &= \psi_0\exp\left(-\frac{x}{k^{-1}}\right). \end{aligned} \tag{1.18}$$

This potential arises in the system as as a result of the interaction between the colloids and the free ions in the bulk solution (counter-ions). We can conclude from the boundary conditions that this potential is a short range one. Since the size of the colloid is much bigger than the counter ion size, the colloid will behave as an infinite plate in yz plane.

Therefore, the contribution from both y and z components will be very small, and x is the only component that significantly creates the potential. In this case, this potential seems as a 1D formula, where x represents the separation distance between the surfaces.

For a spherical colloid in three dimensions, the potential interaction has the following formula [1],

$$\psi(r) = \frac{ze}{4\pi\epsilon_r\epsilon_0}\frac{\exp\left[-k(r-\sigma/2)\right]}{r(1+k\sigma/2)}, \tag{1.19}$$

where r is the radial distance from the center of the colloid and σ is its diameter. The energy between two identical colloidal particles is called Yukawa potential energy and is often seen in the literature in the form [8],

$$u_Y(r) = \epsilon\frac{\exp\left[-k(r-\sigma)\right]}{r}, \tag{1.20}$$

where $\epsilon = z^2e^2/[4\pi\epsilon_r\epsilon_0(1+k\sigma/2)^2]$ gives the overall strength of the interaction.

As seen in Eq. 1.18 or Eq. 1.19 this potential energy is always repulsive, and it depends inversely on k^{-1}. At the same time, k^{-1} depends on the free ionic concentration in addition to the temperature. In other words, this repulsive potential can be enhanced be reducing the Debye screening length, which can be done either by removing the salt from the system or by increasing the temperature. Thus, salt concentration plays an important role in stability of the colloidal suspension against aggregation.

Polymer Stabilization

In this method, grafted polymers are added to the colloidal system in order to disperse the colloids away from each other. The basic idea behind this method is that the polymer chains are attached at one end to the colloid surface and stick out into the solution as shown in Fig. 1.1. As one of these colloids approaches another colloid, the concentration of the grafted polymers increases in the region between the two colloids. Accordingly,

the osmotic pressure increases and leads to a repulsive force that prevents the forming of aggregations or clusters [2, 4].

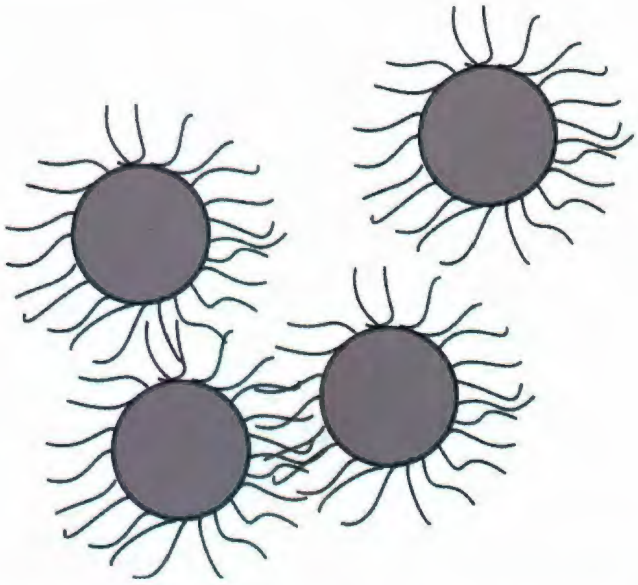

Figure 1.1: Attaching grafted polymers on the colloid surface as adapted from Ref. [4]. As the colloids get closed to each other, the polymer concentration between the colloids increases and leads to a repulsive force.

Three principle points must be taken into account regarding polymer stabilization. Firstly, some grafted polymers have an attractive interaction between the segments, which could drive the colloids to aggregate with each other. For that, a good solvent must be used in order to lower the attraction energy between the segments. Secondly, the range of the repulsive force can be controlled by the length of the polymer chain. Obviously, longer chains increase the repulsive force interaction. Thirdly, the grafted polymer chains attach to the colloids by either physical or chemical bonds. Regardless of the type of bond, the strength of the bond must be greater than the thermal energy k_BT. Otherwise, the grafted polymers will separate from the surfaces of the colloids.

Depletion Interactions

This interaction appears when particles of intermediate size between the colloids and the solvent molecule, are added to the colloidal system. Typically, the intermediate particles are dissolved polymers that do not attach on the colloid surface; instead, they form globules that move freely inside the solution. Modeling the polymers as spheres of radius a, there consequently arises a *depletion zone* around each colloid, into which no polymer center can enter. In Fig. 1.2, the grey spheres are the original colloids, while the white skin around the colloids is the depletion zones of thickness a. The small particles are the dissolved polymers depicted as spheres. When any two colloids get close enough, their depletion zones will overlap. Consequently, the polymer concentration in the area between these two colloids will be much less than the polymer concentration elsewhere around the colloids. This makes the osmotic pressure in the solution bigger than that in the overlapping region, pushing the two colloids together. So, the depletion interaction is attractive in contrast with electrostatics and polymer stabilization [4].

The total (attractive) depletion interaction potential can be expressed as,

$$U_{dep} = -P_{osm} V_{dep}, \tag{1.21}$$

where P_{osm} is the osmotic pressure that can be approximated from the ideal gas law for N polymer particles in a solution of volume V,

$$P_{osm} = \frac{N}{V} k_B T, \tag{1.22}$$

while V_{dep} is the depletion volume, which represents the total overlapping volume in the depletion region between colloids. V_{dep} for two overlapping spherical colloids is given by,

$$V_{dep} = \frac{4\pi}{3}(a+L)^3 \left(1 - \frac{3r}{4(a+L)} + \frac{r^3}{16(a+L)^3}\right), \tag{1.23}$$

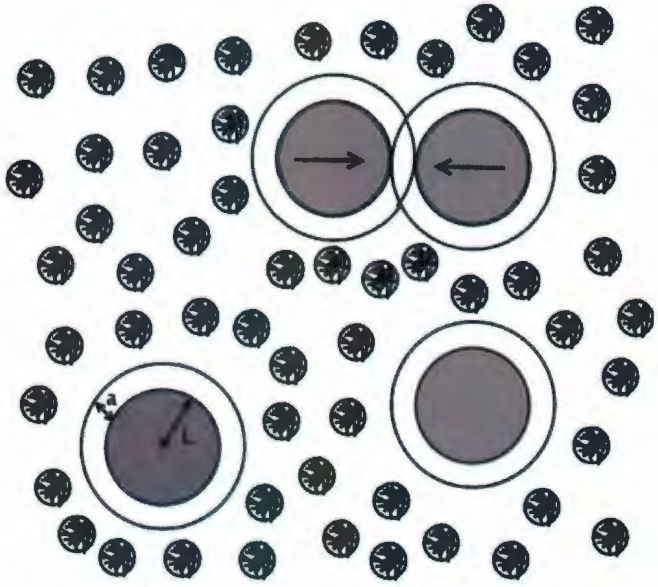

Figure 1.2: The depletion interaction as adapted from Ref. [4]. The small spheres are the polymer coils or the dissolved polymers. The grey spheres are the original colloids of radius R, while the white shell is the associated depletion region of thickness a.

where r is the center to center separation, applicable for the case $2R + a \leq r \leq 2R + 2a$. The magnitude of the depletion interaction increases with polymer concentration, while the range of attraction is controlled by a. Adding polymer can tune the attraction to be comparable to, or even much stronger than the thermal energy ($k_B T$).

1.2 Computer Simulation

1.2.1 Short History

Much of the history of computer simulation started during and after the Second World War in the development of nuclear weapons. At the time, "electronic computer machines" were very large but rather simple machines restricted to the military, where they were used to perform very heavy computation. In the 1950s, the electronic computing machines spread to nonmilitary usage, and this was the starting point for computer simulation studies. The first computer simulation, or numerical experiment, was done in 1953 at Los Alamos National Laboratory in the United States by Metropolis, Rosenbluth and

Teller. They used the most powerful computer of that time, called MANIAC, in order to study liquid structures [9, 10].

In 1953, Metropolis and coworkers employed a new technique which they called Monte Carlo (MC) Simulation, and which is still widely used today. The name aptly connects the dependence of MC on random numbers to one of the great gambling capitals of the world [9, 10, 11]. While today MC refers broadly to techniques based on the acceptance and rejection of randomly generated states, we employ in this thesis the original "Metropolis algorithm" to generate an ensemble of states in the canonical ensemble of our model.

Until 1957, MC was used to simulate ideal model systems, e.g. treating molecules as hard spheres. The results obtained by these early simulations were not directly comparable with experimental results on atomic or molecular liquids. In 1957, Wood and Parker were the first to carry out simulations with the Lennard-Jones interaction potential. These simulations were comparable to experiments on systems such as liquid argon [10].

MC is a powerful technique for obtaining structural and thermal properties of model systems interacting through some potential. On the other hand, MC is not used to solve equations of motion for the particles of a model system, and therefore dynamic properties are not accessible. This pushed Alder and Wainwright, starting in 1957, to design a new technique called Molecular Dynamics (MD) that does solve Newton's equations of motion. In 1964, Rahman used MD to study systems of Lennard-Jones particles. While there have been many developments in MC and MD since those pioneering times, the same basic ideas are behind today's simulations of simple fluids, biological molecules and other materials of varying degrees of complexity [10].

1.2.2 Computer Simulation: applications and motivations

Computer simulation experiments are useful for modeling natural systems in Physics, Chemistry, Biology, and Engineering. In Physics, few problems can be solved analytically, and often approximations are employed to make a problem more tractable. On the other hand, most problems, specifically in statistical mechanics, are neither soluble exactly nor treated adequately with approximations. Particularly difficult problems involve a large number of interacting particles. Therefore, computer simulation has become a very useful tool for solving many-body problems [10].

Computer simulations have a valuable role in providing essentially exact results for problems in statistical mechanics which would otherwise only be soluble by approximate methods. Computer simulations provide a way of testing theories in a virtual laboratory where all interactions are explicitly known. Also, computer simulation results can be compared with the real experimental results in order to support the experimental explanations and to assist in the interpretation of new results. Computer simulation aims to be a bridge between models and theoretical predictions on the one hand, and between models and experimental results on the other as illustrated in Fig. 1.3 for a liquid system [10]. Indeed, the theoretical predictions can be compared with experimental results by using directly a specific model, but definitely computer simulation allows you test the model itself.

1.3 Electrorheological (ER) Fluid

An electrorheological (ER) fluid is a kind of colloidal system, which is composed of non-conducting particles in an electrically insulating fluid, and responds to an external electric

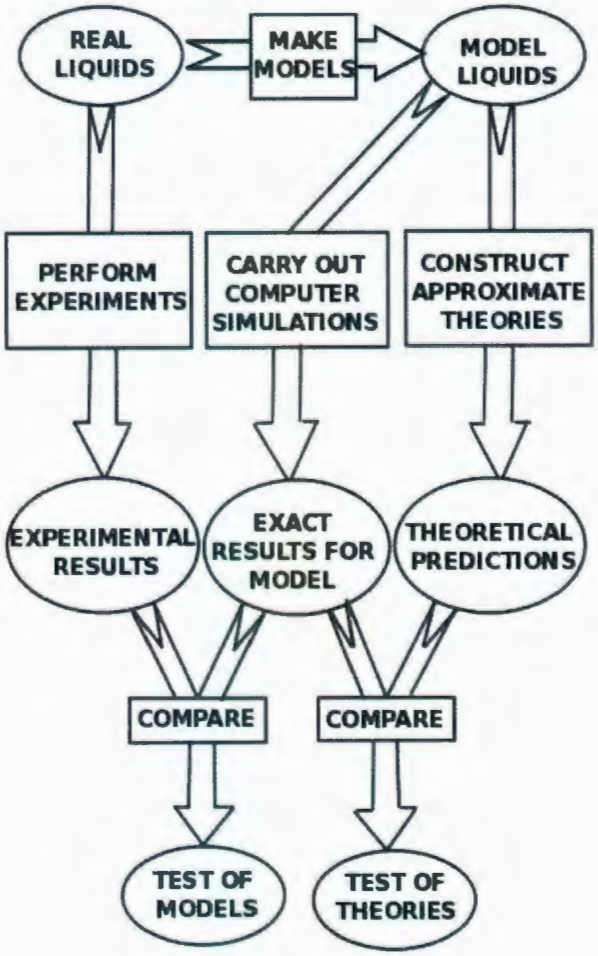

Figure 1.3: The connection between experiments, theory, and computer simulation, as adapted from Ref. [10].

field [12, 13, 14, 15]. As a result, the rheological properties of an ER fluid such as viscosity, shear stress and shear modulus can change several orders of magnitude with the applied electric field strength. This change depends basically on the physical properties of both the dispersed particles and dispersing medium [16].

Due to the fact that the mechanical properties of an ER fluid can be controlled over a wide range, ER fluids can be used in various industrial applications. Typically, ER fluids can be used as an electric and mechanical interface, for example, clutches, brakes, hydraulic valves, displays, and damping systems [17, 18, 19]. Also, ER fluids can be used to fabricate advanced functional materials such as photonic crystals, smart inks,

and heterogeneous polymer composites [16].

In the class of ER fluids with which we are concerned, the mismatch in dielectric constants between the colloidal particles and surrounding fluid results in what can effectively be described by a system of hard sphere particles interacting through induced dipole moments.

Electrorheological structures have been studied experimentally [7, 20, 21, 22], theoretically and using computer simulation [8, 23, 24, 25, 26]. In Ref [23], Tao and Sun proved using MC simulation that the ground state structure of a particular ER fluid in a strong electric field is a body centered tetragonal (bct) structure. Tao proved theoretically that above a certain critical field strength, the ER fluid experiences a phase transition to a solid state whose ideal structure is body centered tetragonal (bct) [24]. In Ref. [8], Hynninen *et al.* used MC simulation to study the phase behaviour of hard and soft spheres by changing the packing fraction and external field strength. Martin *et al.* in Ref [26] studied the structures obtained by applying two different types of external electric field: uniaxial and biaxial external electric fields. Kumar *et al.* in Ref. [21] reported experimentally a new phase at low volume fraction (1%) due to a pure dipolar interaction, and that new phase is called "void phase". Agarwal *et al.* in Ref. [22] also reproduce the void phase experimentally by applying an external electric field on a colloidal system al low volume fractions. They assume that the total interaction that could produce this phase must consists of long range repulsion and short range attraction, but they did not determine the exact interactions. More details about this phase behaviour will be presented in the next chapters.

1.4 Motivation

In 2005, a new phase of a cellular pattern consisting of particle-free domains enclosed completely by particle-rich walls was discovered by Kumar *et al.* [21]. Kumar *et al.* produced this phase by applying an external electric field on a colloidal system at very low volume fraction ($< 1\%$) as shown in Fig. 1.4(a). When the external electric field is applied, the colloids start to interact with each other via a dipole-dipole interaction and tend to form rod-like structures. After that, these dipolar rods attract and repel each other to form this phase. Kumar *et al.* assumed that all the effects of other competing

Figure 1.4: Formation of cellular patterns (or voids) in the plane perpendicular to the field direction. (a) is the void pattern obtained by using pure dipole-dipole interaction as Kumar *et al.* assumed in their work, while (b) is the void pattern obtained as a result of a total potential that includes long range repulsion and short range attraction as Agarwal *et al.* assumed.

forces were suppressed, implying that the dipole-dipole interaction is solely responsible for producing this phase. In fact, Kumar *et al.* were studying particles that were $100\mu m$ in size, so theirs was not a true Brownian system but a granular system (from the standpoint of theory they are probing energetics and not the free energy). So one could not call their structure a thermodynamic phase. Likewise, Agarwal *et al.* reproduced this interesting

phase at very low volume fraction but acknowledged that other forces may play a role, and they called this phase as the "void phase". They commented on the importance of long range repulsion and short range attraction for producing this phase, but they did not determine the exact interactions. The obtained void phase is presented in Fig. 1.4(b).

On the other hand, Ref [27] is a real-space study of structure formation in a colloidal suspension of silica and PMMA spheres under an external electric field at higher volume fractions. In this work, the authors reported *bct* (body centered tetragonal) crystallites in two systems, silica/water-glycerol at $\phi = 15\%$ and PMMA spheres/cyclo-heptyl bromide at $\phi = 25\%$, as shown respectively in Figs. 1.5(a) and 1.5(b). Also, Fig. 1.5(c) is unpublished work by A. Agarwal and A. Yethiraj that shows a structure of silica suspended in water:dimethyl sulfoxide under an external electric field at volume $\phi = 4.4\%$. One of our targets in this thesis is to reproduce these structures, using computer simulation of our simplified model, at area fractions equivalent to the volume fractions used in that experimental work.

In addition, Hynninen *et al.* in Ref. [8] used MC simulation to study the phase behaviour of an ER fluid under the influence of an external electric or magnetic field. Two different cases were considered by Hynninen *et al.*. In the first case, the particles in the colloidal system interact with each other via the dipole-dipole interaction alone (dipolar hard spheres), while in the second case the particles interact with each other via a pair potential that is a sum of the Yukawa interaction and the dipole-dipole interaction (dipolar soft spheres). Indeed, the dipole-dipole interaction is an anisotropic interaction that forms long chains along the direction of the applied electric field. It gives rise to long range attraction between the chains or between particles along the field axis, and it can be controlled by changing the external electric field. The Yukawa interaction gives

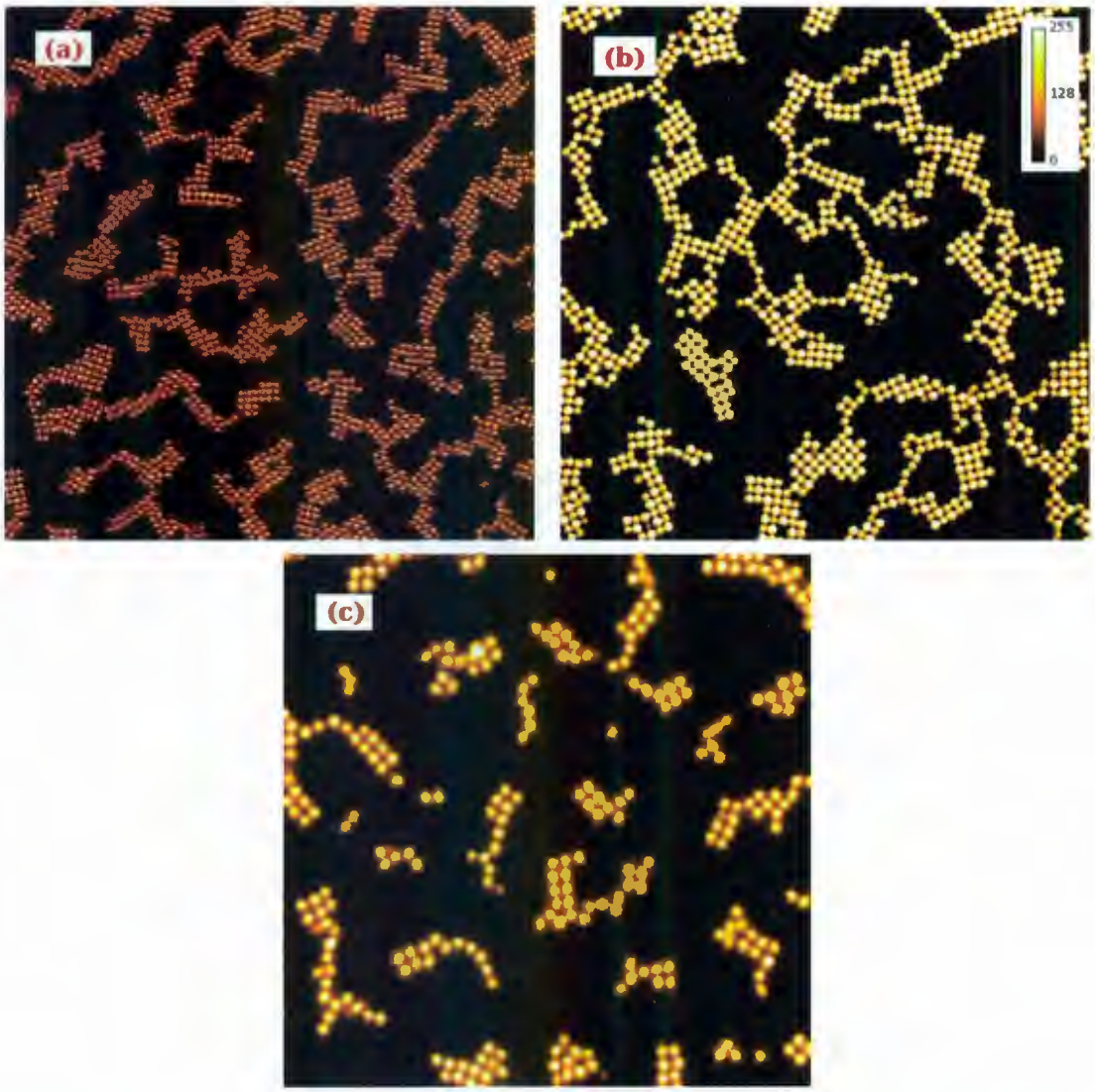

Figure 1.5: Fig. (a) and (b) are bct structures obtained in silica/water-glycerol and PMMA spheres/cyclo-heptyl bromide systems at volume fraction that equal 15% and 25%, respectively. (c) shows fluid-bct coexistence for silica solved in water:dimethyl sulfoxide under an external electric field effect at $\phi = 4.4\%$.

rise to a medium range repulsion interaction and it can be controlled by adding and removing salt from the solution. The phase diagrams depends basically on both dipole moment strength γ and packing fraction η. The phase diagram of dipolar hard spheres shows fluid, face-centered-cubic (fcc), hexagonal-close-packed(hcp), and body-centered-tetragonal (bct) phases. The phase diagram of dipolar soft spheres shows, in addition to the above mentioned phases, a body-centered-orthorhombic (bco).

In this thesis, we present a simplified model in which we assume a system in which chains of some fixed length are well formed, and consider interactions only between chains. Our simplified model, therefore, is essentially a two-dimensional one. We wish to see whether the simple physics of interacting dipolar chains can account for the structure typical of the experimental system, and in particular whether the void phase is recovered at low packing fraction. We also explore how other interactions that may be presented in experiments, such as Yukawa and van der Waals forces, affect the system.

1.5 Short Outline of the Thesis

In chapter 2, we discuss in detail the effect of an external electric field on a colloidal system. Then, we introduce the dipole-dipole interaction, and how it can be used to derive exact formulas for stacked and staggered dipolar interactions. After that, we describe Monte Carlo (MC) simulation technique, and how we use it to model the dipolar system. Finally, we introduce and discuss some structural quantities and theories that are useful in analyzing our data.

In chapter 3, we present data from MC simulations of our model over a broad range of temperature and area fraction. After that, we present the phase diagram obtained for the dipolar system as a function of temperature and area fraction, and we show different structures obtained in the phase diagram. We also use different tools, such as the two state model, structure factor and pressure calculations in order to check whether there is a phase transition. Finally, we compare our results with previous simulation studies on dipolar hard spheres and other interacting colloids.

In chapter 4, we introduce the void phase produced by two experimental groups, Kumar *et al.* and Agarwal *et al.*, at low volume fraction ($< 1\%$). After that, we discuss some physical interactions that could produce the void phase, such as the dipolar interac-

tion, Yukawa interaction, and van der Waals interaction. Then, we introduce some "toy" potentials that we have simulated in order to try to gain a qualitative understanding of the features of inter-chain interactions that may give rise to a void phase. Finally, we discuss our results and conclusions in Chapter 5.

Chapter 2

Theoretical Model

In this chapter, we introduce the dipole-dipole interaction and our reduction of a three dimensional system to a simplified two dimensional model. Then, we describe how we realize the model using Monte Carlo (MC) computer simulation. Finally, we discuss some structural quantities such as the pair correlation function, structure factor, fraction of percolating clusters, cluster size distribution, and mean square displacement.

2.1 Electrorheological Fluid and Colloids

An electrorheological (ER) fluid can be defined as a suspension of non-conducting particles of about a few micrometers in size in an electrically insulating fluid that responds to an external electric field [12, 13, 14, 15]. Applying an external electric field to a colloidal suspension induces dipole moments in the colloids that align with the field. If the dielectric constant of the particles is larger than the dielectric constant of the solution, the dipole moments will be parallel to the external electric field direction; if the dielectric constant of the particles is smaller than that of the solution, the dipole moments will be anti-parallel to the field. In either case, the particles will interact through a dipole-dipole interaction [8, 22, 24, 23]. In principle, when the field of neighbouring dipoles is included, the total field becomes spatially non-uniform. In a spatially non-uniform there is in principle also a dielectrophoretic force, which also is ignored in this study.

In this work, we consider a colloidal suspension under the influence of an external electric field. The colloidal system can be modeled as a system of dipole moments that are always pointing in the same direction, with each moment at the center of a hard sphere. The dipole-dipole interaction for two dipole moments, $\vec{P}_1$ and $\vec{P}_2$, is presented in Eq. 2.1, where ϵ_0 is the permittivity of the free space and $\vec{r}$ is separation vector between the two dipole moments [28, 29],

$$U(\vec{r}) = \frac{1}{4\pi\epsilon_0 r^3}\left(\vec{P}_1 \cdot \vec{P}_2 - 3(\vec{P}_1 \cdot \hat{r})(\vec{P}_2 \cdot \hat{r})\right). \tag{2.1}$$

In our case, all the colloids in the colloidal suspension are identical and point in the same direction as the external electric field direction, which defines our z-axis. Hence, $(\vec{P}_1 = \vec{P}_2)$, and then Eq. 2.1 can be written as in Eq. 2.2,

$$\begin{aligned} U(\vec{r}) &= \frac{P^2}{4\pi\epsilon_0 r^3}\left(1 - 3(\hat{P}_1 \cdot \hat{r})(\hat{P}_1 \cdot \hat{r})\right) \\ U(r,\theta) &= \frac{A_D}{r^3}\left(1 - 3\cos^2\theta\right), \end{aligned} \tag{2.2}$$

where θ is the angle between the dipole moment direction and $\vec{r}$, as illustrated in Fig. 2.1, and A_D is called the dipolar strength that equals,

$$A_D = \frac{P^2}{4\pi\epsilon_0}. \tag{2.3}$$

In terms of the material properties of the colloidal suspension and the applied field,

$$A_D = \frac{\pi\sigma^6\alpha^2\epsilon_s|E_{loc}|^2}{16} \tag{2.4}$$

where α is the polarizability of the particles, σ is the colloid's diameter, ϵ_s is the dielectric constant of the solvent, and $|\vec{E}_{loc}| = |\vec{E}_{ext}| + |\vec{E}_{dip}|$ where $\vec{E}_{dip}$ is the field due to neighbouring dipoles. For our simple model, we neglect the effect of $\vec{E}_{dip}$ as is done in [8]

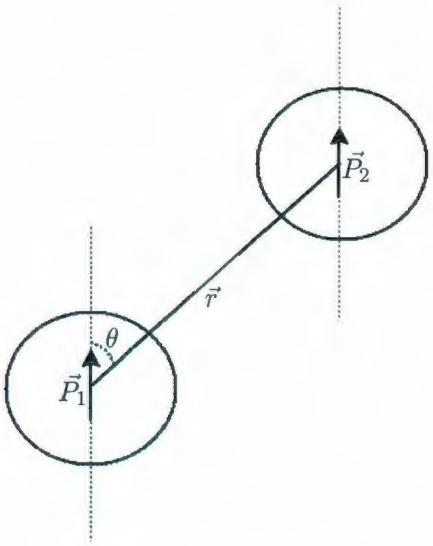

Figure 2.1: The interaction potential between two dipole moments, $\vec{P}_1$ and $\vec{P}_2$, separated by a distance $|\vec{r}|$. θ is the angle between the dipole moment and the separation vector $\vec{r}$.

The radial force component between the two dipole moments can be found as follows,

$$\begin{aligned} F_r(r,\theta) &= -\frac{\partial}{\partial r}U(r,\theta) \\ &= \frac{3A_D}{r^4}\left(1-3\cos^2\theta\right). \end{aligned} \tag{2.5}$$

Obviously, r in Eq. 2.5 determines the strength of the interaction, while θ determines whether the force is repulsive or attractive. In Fig. 2.2, we observe that when the angle between the two dipole moments is in the range [54.74°, 125.26°], the interaction is repulsive; otherwise the interaction is attractive. Therefore, the dipole-dipole interaction in the colloidal system induces anisotropic interactions, either attractive or repulsive depending on θ, as illustrated in Fig. 2.2.

In this interaction, the potential energy is minimized at either angle 0° or 180°. Therefore, in the presence of a strong external field, the colloids will arrange themselves into long chains along the external electric field direction. Experimentally, when the external electric field is sufficiently large, the system becomes one composed of such chains. In

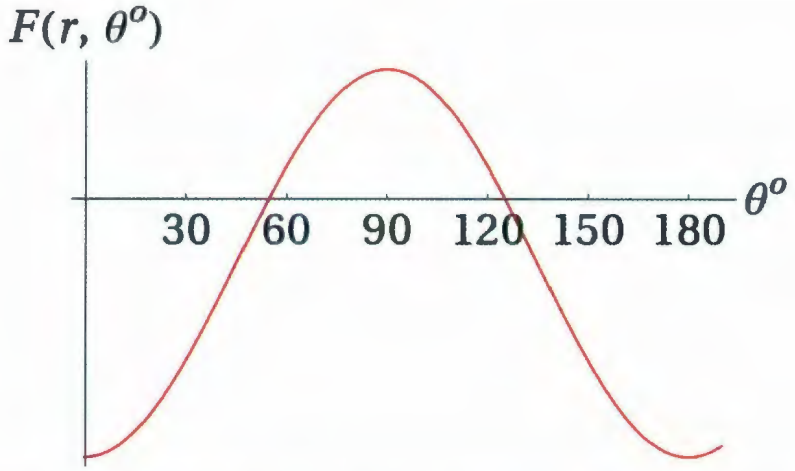

Figure 2.2: Radial component of the force between two dipoles. The interaction is attractive in the range $[0^o, 54.73^o]$ and $[125.27^o, 180^o]$, while it is repulsive in the range $[54.74^o, 125.26^o]$.

the work of Agarwal *et al.*, the length of the chains is roughly 50 particles on average. In this regime, the system effectively becomes two-dimensional when viewed down the field axis, and the chains appear as disks in a plane. As we explain below, the chains/disks tend to attract at very short distances and pack with square symmetry. Further, the chains tend to repel at larger range. This combination of short range attraction and long range repulsion between disks is made explicit by the reduction in dimension (i.e. this is not obvious on the level of individual particles, but becomes apparent when considering chains), and is responsible for the appearance of stable clusters in the system. While the paradigm of short range attraction and long range repulsion leading to finite clustering has emerged as an important concept in other colloidal systems, it has not been fully appreciated in the literature for the system we are modeling presently.

Furthermore, the novel "void" phase seen now by two experimental groups exists in the regime when chains are well formed and the system becomes essentially two-dimensional. It is one of the goals of this work to determine whether a system of dipolar colloids arranged in chains can form this void phase, or whether additional interactions are required.

2.2 Types of dipolar interaction

The interaction potential between any two dipole chains can be divided into two principle types. Typically, this division depends on how the dipoles in each chain encounter the other dipoles in the second chain. If the dipoles in the first chain encounter the opposite dipoles in the second chain "face to face", as shown in Fig. 2.3, we call this "stacked". On the other hand, if the particles in the second chain are shifted a distance of $\sigma/2$ in the $z-$direction, as shown in Fig. 2.6, they are "staggered". In this work, we study the structures obtained from the interaction between the chains that are either staggered or stacked with respect to each other. In the following two sections, we deal with each dipolar interaction.

2.2.1 Stacked Dipolar Interaction

In this type of interaction, the angle θ between any two dipoles at the same height but in different chains is 90^o, and the closest distance between the chains is σ, as shown in Fig. 2.3. The final formula of the dipolar interaction potential between any two chains can be obtained by summing all individual interactions of each dipole in the first chain with the other dipoles in the second chain. In the rest of this section, we will explain the derivation of the stacked dipolar interaction potential between two chains starting from the basic dipole-dipole interaction between two dipoles [29],

$$U_{12}(\vec{r}) = \frac{A_D}{r_{12}^3}\left(1 - 3\cos^2\theta_{12}\right), \tag{2.6}$$

where $r_{12} = |\vec{r}_{12}|$ is the distance between the two dipoles, and θ_{12} is the angle made between $\vec{r}_{12}$ and z-axis.

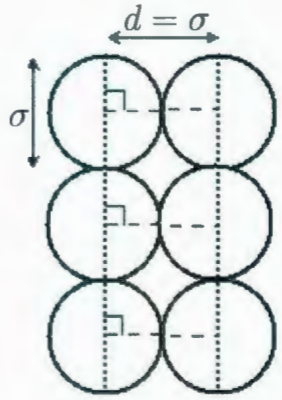

Figure 2.3: Two interacting chains via stacked dipolar interaction at the closest distance $d = \sigma$, where σ is the colloid's diameter.

From Fig. 2.4, the total stacked dipolar interaction potential between the dipole P_0 and the other dipoles in the second chain can be written as,

$$U_0(d) = A_D \sum_{n=1}^{L} \left[\frac{1 - 3\cos^2 \theta_{0n}}{r_{0n}^3} \right], \tag{2.7}$$

where d is the distance between the two chains, n is the particle's rank in the second chain, and L represents the total number of dipoles in that chain. Also, from Fig. 2.4, we can obtain the following relations,

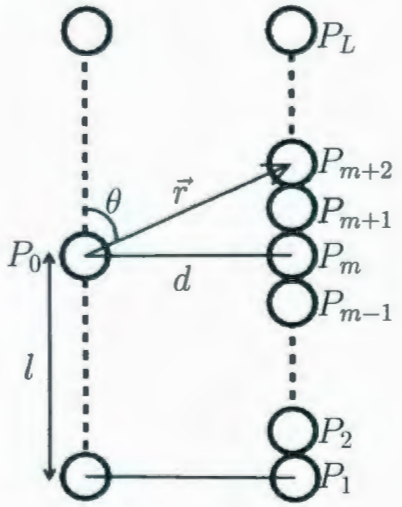

Figure 2.4: The interaction between two chains separated by a distance d via stacked dipolar interaction. P's are the dipole moments, $|\vec{r}|$ is the separation distance between two dipole moments in two different chains, and θ is the angle between the dipole moment and the separation distance $|\vec{r}|$, and l is the height of a specific dipole P_0 from the bottom.

$$r = \left((l-(n-1)\sigma)^2 + d^2\right)^{1/2} \tag{2.8}$$

$$\cos\theta = \frac{l-(n-1)\sigma}{r} = \frac{l-(n-1)\sigma}{\left((l-(n-1)\sigma)^2 + d^2\right)^{1/2}}. \tag{2.9}$$

Using Eqs. 2.8 and 2.9, and assuming that all the dipole moments have the same magnitude, we can rewrite Eq. 2.7 as follows,

$$U_0(d) = A_D \sum_{n=1}^{L} \left[\frac{d^2 - 2\left(l-(n-1)\sigma\right)^2}{\left((l-(n-1)\sigma)^2 + d^2\right)^{5/2}} \right]. \tag{2.10}$$

By considering all dipoles in the left chain in Fig. 2.4 and substituting $l = (m-1)\,\sigma$ in Eq. 2.10, the total interaction potential between two stacked chains is,

$$U_c(d) = A_D \sum_{n=1}^{L} \sum_{m=1}^{L} \left[\frac{d^2 - 2(m-n)^2\sigma^2}{\left(d^2 + (m-n)^2\sigma^2\right)^{5/2}} \right]. \tag{2.11}$$

Obviously, the stacked interaction depends on both the distance d between the chains and the total number of particles in each chain (L). We plot the total potential energy between two interacting chains of different values of L at a range of distances from 0 to 10 σ in Fig. 2.5. We observe from Fig. 2.5 that this interaction is repulsive at any distance d and for any L. In general, this interaction potential depends only weakly on L at large distances ($d > 4\sigma$), and for large L becomes roughly proportional to L at $d = \sigma$. Therefore, increasing the repulsion interaction at short range can be done by just increasing the number of particles L in each chain. The inset in Fig. 2.5 shows the expanded region from $\sigma = 1$ to $\sigma = 5$ in order to highlight the differences between the curves for different L.

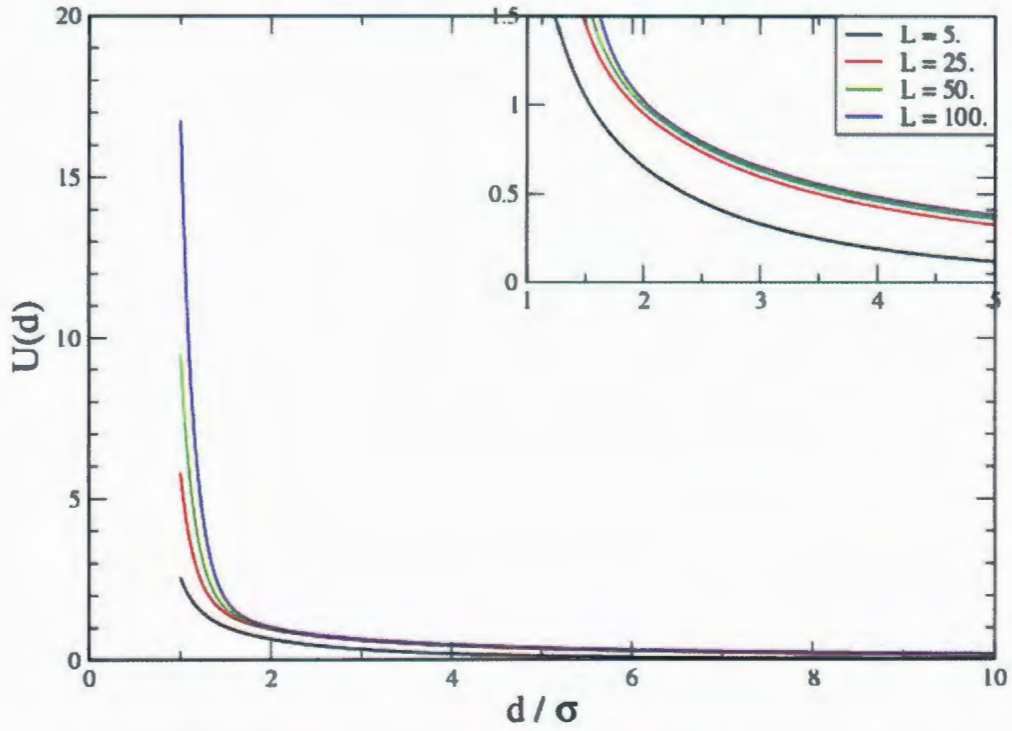

Figure 2.5: The stacked dipolar interaction potential for different values of L, where L is the number of particles in each chain. This interaction potential has a small repulsion at large distances d, and significantly high repulsion at short distances.

2.2.2 Staggered Dipolar Interaction

In the staggered configuration, the angle between any two adjacent dipoles in two different chains is 60^o or 120^o, and the closest distance between any two adjacent chains is $\sqrt{3}/2\sigma \approx 0.866\ \sigma$ as shown in Fig. 2.6. The final formula of the staggered interaction potential between two staggered chains can be obtained by summing all individual interactions of each dipole in a chain with other dipoles in the second chain, as seen in Fig .2.7. From this figure, we can obtain the following relations,

$$r = \left(\left(l - \left(n - \frac{1}{2}\right)\sigma\right)^2 + d^2\right)^{1/2} \tag{2.12}$$

$$\cos\theta = \frac{l - (n - \frac{1}{2})\sigma}{r} = \frac{l - (n - \frac{1}{2})\sigma}{\left(\left(l - (n - \frac{1}{2})\sigma\right)^2 + d^2\right)^{1/2}}. \tag{2.13}$$

Using Eqs. 2.12 and 2.13, and assuming the same dipole moments for all dipoles, the

interaction potential between the dipole P_0 and the second chain is given by the following equation,

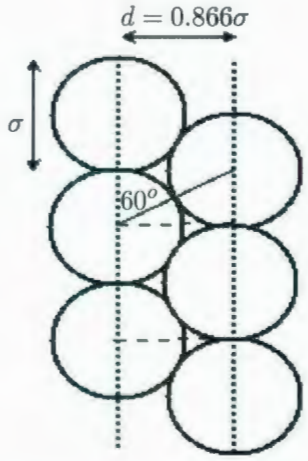

Figure 2.6: Two interacting chains via staggered dipolar interaction at the closest distance $d = 0.866\ \sigma$, where σ is the colloid's diameter.

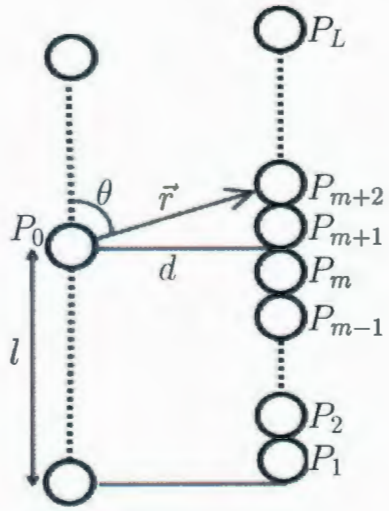

Figure 2.7: The interaction between two chains separated by a distance d via staggered dipolar interaction. P's are the dipole moments, $|\vec{r}|$ is the separation distance between two dipole moments in two different chains, θ is the angle between the dipole moment and the separation distance $|\vec{r}|$, and l is the height of a specific dipole P_0 from the bottom.

$$U(d) = A_D \sum_{n=1}^{L} \left[\frac{d^2 - 2\left(l - (n - \frac{1}{2})\sigma\right)^2}{\left(\left(l - (n - \frac{1}{2})\sigma\right)^2 + d^2\right)^{5/2}} \right]. \tag{2.14}$$

By considering all dipoles and substituting $l = m\sigma$ in Eq. 2.14, the total interaction potential between two staggered chains is,

$$U_g(d) = A_D \sum_{n=1}^{L} \sum_{m=1}^{L} \left[\frac{d^2 - 2\left(m - (n - \frac{1}{2})\right)^2 \sigma^2}{\left(d^2 + \left(m - (n - \frac{1}{2})\right)^2 \sigma^2\right)^{5/2}} \right]. \tag{2.15}$$

As with the stacked case, the staggered dipolar interaction depends on both the distance d between the chains and the total number of particles in each chain L. We plot the total potential energy between two interacting chains of different values of L at a range of distances from 0 to 10 σ in Fig. 2.8. We observe from the figure that this interaction for any L is repulsive at large distances and attractive at short distances. The repulsive barrier peaks near 1.5σ, although this distance increases with L. The difference between the interaction potentials for different values of L is most apparent at short distances ($d < 4\sigma$). Accordingly, increasing the attractive interaction can be done simply by increasing the number of particles L in each chain. The inset in Fig. 2.8 shows the expanded region from $\sigma = 1$ to $\sigma = 5$ in order to highlight the differences between the curves for different L.

2.3 Energetics of Clustering.

The short range attraction and long range repulsion of the staggered pair potential complete in such a way as to give rise to finite clustering rather than to a homogeneous condensed phase. To understand this qualitatively, consider an existing compact cluster composed of several disks. Another disk brought into contact with the cluster will feel a strong attraction from its nearest neighbours, but will feel a small repulsion from the rest of the disks in the cluster. Whether the addition of the disk lowers the energy of the cluster depends on the strength of nearest neighbour bonds relative to numerous

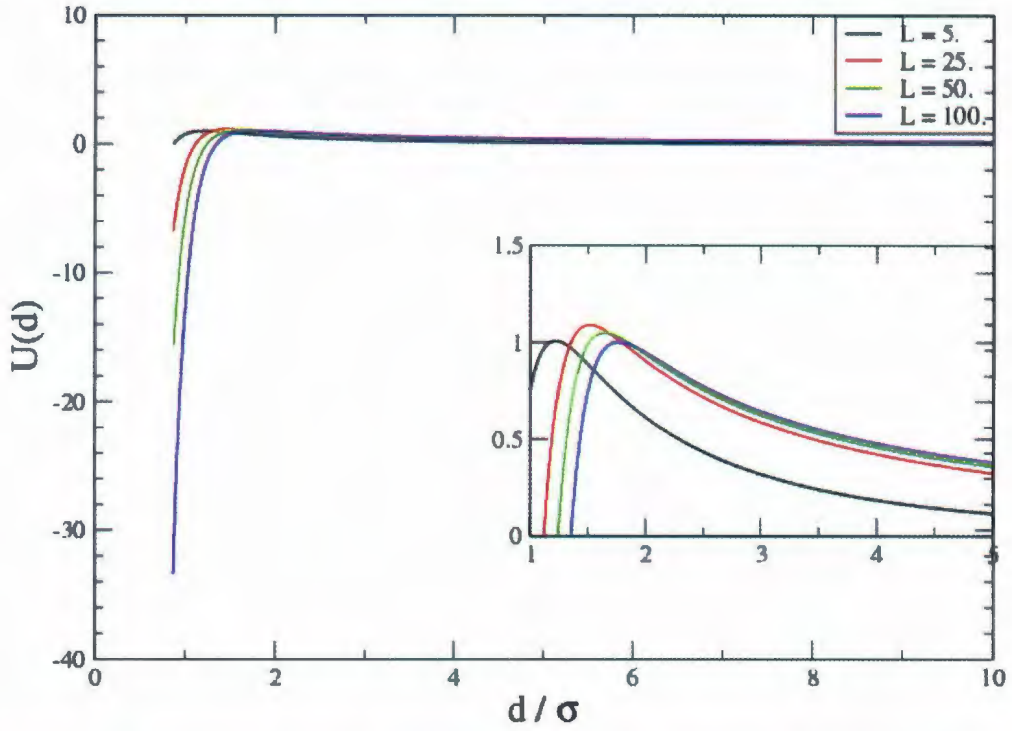

Figure 2.8: The staggered dipolar interaction potential for different values of L, where L is the number of particles in each chain. This interaction potential has a small repulsion at large distances d, and significantly high attraction at short distances.

unfavorable interactions with the rest of the cluster.

Although clusters within the system are not isolated (but rather interact with other parts of the system), and furthermore are subject to thermal fluctuations and entropy considerations, it is nevertheless useful to examine isolated clusters at zero temperature to gain a perspective on what structures may be expected to occur in the system. To this end we calculate the energy of rectangular clusters m particles wide and n particles long with all nearest neighbours at contact (0.866σ). In Fig. 2.9 we plot the potential energy as a function of n for a few values of m. We observe that for narrow structures ($m = 1, 2, 3$), the energy keeps decreasing with increasing length. For more compact structures ($m = 4, 5, 6$), we find a length beyond which it is energetically unfavorable to grow. For $m \times m$ square clusters, the energy increase beyond $m = 7$. Thus, we should not be surprised to see in our system long quasi-one-dimensional structures as well as

fairly small compact clusters.

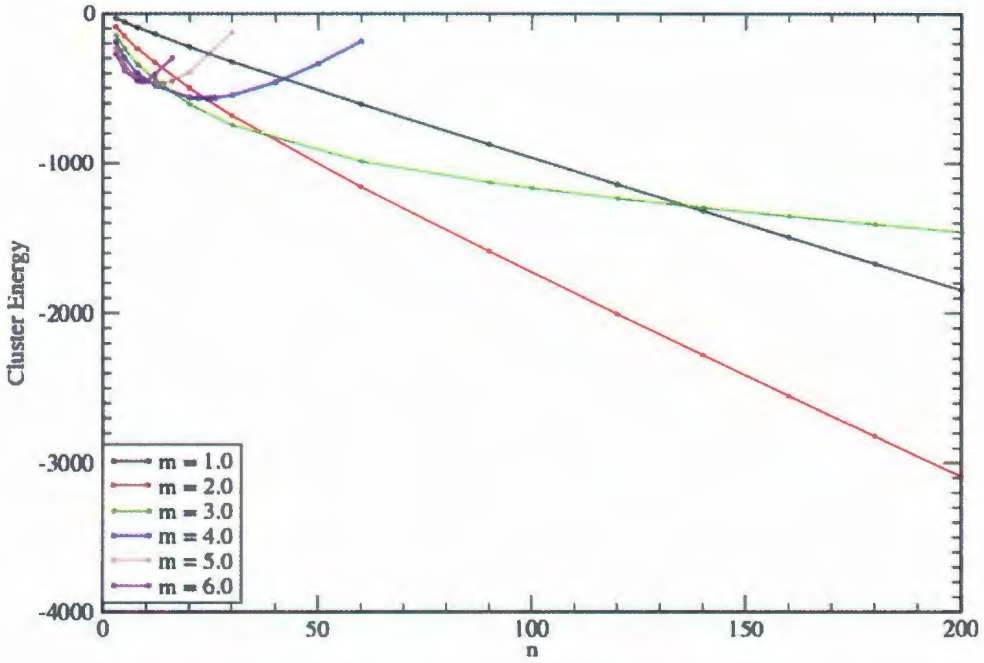

Figure 2.9: The potential energy for clusters of size $n * m$ at zero temperature.

2.4 Monte Carlo Simulation (MC)

We perform MC simulation to model the dipolar system as a 2D system of 2500 interacting disks, where each disk represents a chain composed of 50 particles directed along the would be z-axis. In the simulations, each pair of chains must interact with each other via one of two possible potentials. A hard sphere potential at $r = 1\ \sigma$ followed by a stacked dipolar interaction, or a hard sphere at $r = 0.866\ \sigma$ followed by a staggered dipolar interaction. Formally, we report all quantities in reduced units, e.g. the reduced temperature is $k_B T\sigma^3/A_D$, reduced pressure is $P\sigma^6/A_D$. For simplicity, we set $\sigma = 1$, $k_B = 1$, and $A_D = 1$. For the rest of this section, we describe MC simulation in general, and we will be referring to the disk as an object. We employ a square simulation box of length L_B. As is commonly done, we implement periodic boundary conditions in the system to eliminate the surface effects.

2.4.1 Periodic Boundary Conditions

Periodic boundary conditions simply mean that if a particle steps outside of simulation box, it is made to re-enter the box from the other side. The following provides a more careful way of thinking about it. The simulation box is replicated throughout space to create an infinite array of identical boxes. As an object moves in the original box, its image in each of the neighbouring boxes moves in the same way. As one of the objects leaves the original box, its image will enter the original box from the opposite face. By this method, the walls are removed, and there are no surface objects. In Fig. 2.10, the grey box is the original box of length L_B, while the white boxes around the central one are images for the original one in all directions. As an object leaves the central box, its images move across their corresponding boundaries. As a result, the number of objects will be the same in each box, and the number density in the central box is conserved. On the other hand, using the periodic boundary conditions does not require storing the coordinates of all images during the simulation [9, 10].

2.4.2 Potential Truncation

In MC, calculating the total potential energy requires calculating all the pairwise distances between the objects in the system. This must include the interaction between each object and the images located in the surrounding boxes. In this case, the total number of pairwise distances is infinite, and of course is difficult to calculate in practice. Therefore, we create a region which has the same size and shape as the basic simulation box. This new box is constructed via the "minimum image convention", where the first object is located at the center of this box, as shown in Fig. 2.11. Then, the first object will interact with the other $(N-1)$ objects and images whose centers are located within this box. Again, this

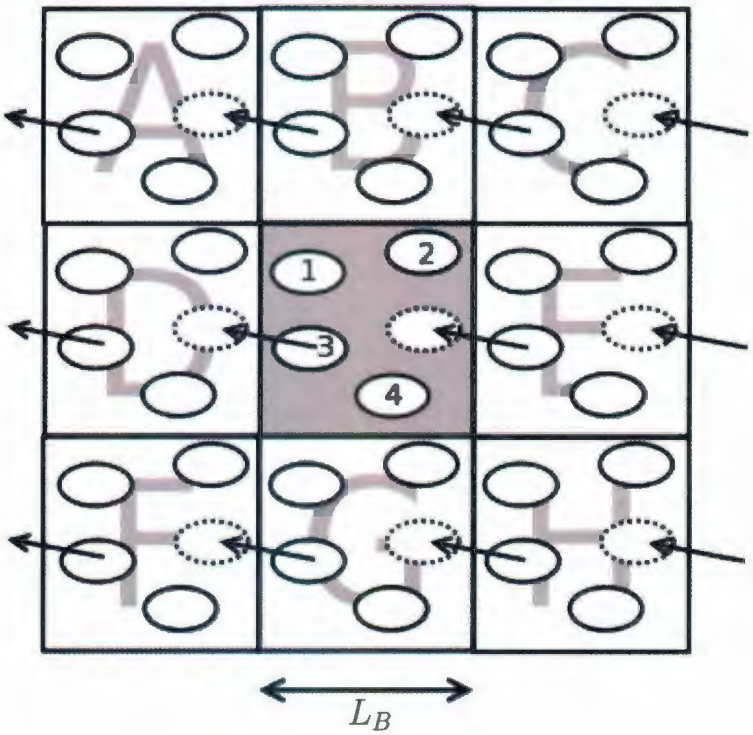

Figure 2.10: An example of a 2D boundary system as adapted from [10]. Each object can enter and leave any box across one of the four walls

strategy will be applied for each object in the original box. Finally, using the minimum image convention in MC involves $\frac{1}{2}N(N-1)$ terms due to the pairwise interactions [9, 10].

Although, using the minimum image convention reduces the infinite number of interactions to $\frac{1}{2}N(N-1)$ interactions, this number is still too large. For a system of 2500 objects, we need to calculate the potential around 3 million times in each step. Due to the fact that the largest contribution to the potential comes from the closest neighbours to the object of interest, we can apply radial cutoff. This means that the potential is zero for $r \geq r_c$, where r_c is the cutoff distance or cutoff sphere's radius. One restriction must be considered when we determine the cutoff distance, which is $(r_c \leq L_B/2)$. In Fig. 2.11, the dashed circle represents the cutoff circle, so the objects 3 and 5_B contribute to the potential of object 1 because their centers are located within the cutoff circle. While objects 2_E and 4_E do not contribute because their centers are located outside the cutoff

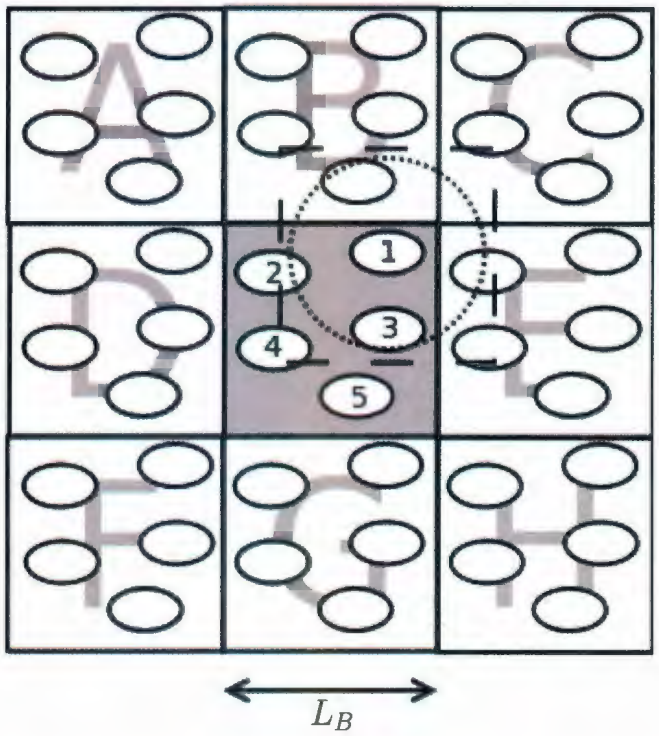

Figure 2.11: The minimum image convention for a 2D system, as adapted from [10]. The dashed square represents the new box constructed for object one using the minimum image convention. The new box contains the same number of objects as the original box. The dashed circle represents a potential cutoff.

circle.

In fact, even if we use potential cutoff, we would still need to compute all $\frac{1}{2}N(N-1)$ pair distances to decide which pairs can interact. Therefore, the potential cutoff is not so helpful for systems of large number of objects, like ($N > 1000$). As a result, we still need an efficient method to speed up the calculations and to save the CPU time. Basically, there are two main techniques to save the CPU time, Verlet List and Cell List techniques. In this work, we use the Verlet List techniques, and it is described in detail in appendix A.

Our potentials behave as $1/r^3$ at large distances (a fairly long range interaction), and so to calculate the system energy accurately, one would be better served using a technique like the Ewald summation method. Therefore, although we set $r_c = L_B/2$, we can not

guarantee that we have not suppressed any phase from emerging (particularly one with periodic, anisotropic order) or introduced any artifacts. However, the experimental work on this system shows that the phases are isotropic on longer length scales, and the local structural length scales in the system to be considerably smaller than our cutoff.

2.4.3 The Metropolis Method

The Metropolis method is the heart of MC simulation. We start this method by moving the first object a uniform random displacement along each of the coordinate axes. The maximum displacement that the object can move is δr_{max} in either x and y directions, as represented in Fig. 2.12, and it equals 0.15 σ for most of the simulations in this thesis, where σ is the object's diameter. The new position of the first object is obtained by using δr_{max} and **RANF(DUMMY)** as in Eq. 2.16, where RANF(DUMMY) is a library function for generating uniform random numbers on (0,1) [10],

$$\begin{aligned} RXNEW &= RX(I) + (2.0 * RANF(DUMMY) - 1.0) * \delta r_{max} \\ RYNEW &= RY(I) + (2.0 * RANF(DUMMY) - 1.0) * \delta r_{max} \\ RZNEW &= RZ(I) + (2.0 * RANF(DUMMY) - 1.0) * \delta r_{max} \end{aligned} \tag{2.16}$$

where $RXNEW$, $RYNEW$ and $RZNEW$ are the new proposed coordinates of the object I, while $RX(I)$, $RY(I)$ and $RZ(I)$ are the old coordinates.

Then, we calculate the total interaction energy for both the initial configuration (V_i) and the new configuration after moving the first object one step (V_f). At this time, we must use the energy test to decide if the first object's move is acceptable or not. There are two possible cases. First, if ($\delta V_{fi} = V_f - V_i \leq 0$), we accept the motion. If ($\delta V_{fi} > 0$), the motion can be accepted with a probability $\exp(-\beta\ \delta V_{fi})$, where ($\beta = 1/T$). In fact, this ratio also represents the Boltzmann factor of the energy difference, and it has a value in

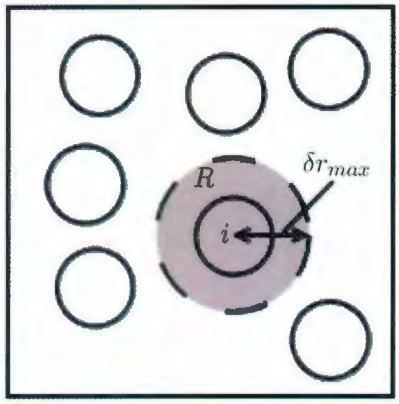

Figure 2.12: The grey region R represents the region where the object i can move in one step.

the range (0, 1). We compare the Boltzmann factor with the generated random number RANF(DUMMY). If $\exp(-\beta\ \delta V_{fi}) >$ RANF(DUMMY), the motion will be accepted, otherwise, the motion will be rejected. This procedure of accepting or rejecting the motion is illustrated in Fig. 2.13 [10].

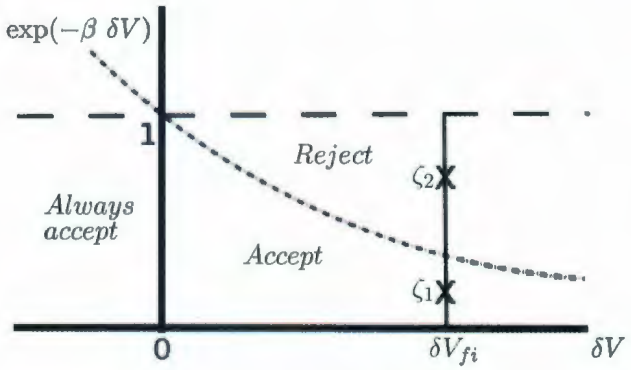

Figure 2.13: Accepting and rejecting rules in MC, as adapted from [10]. The motion will be accepted when at $\delta V_{fi} < 0$, or if $\exp(-\beta\ \delta V_{fi}) >$ RANF(DUMMY).

As a result, if the motion of the object of interest has been accepted, the new configuration will be considered again as an initial configuration. In contrast, if the motion of the object of interest has been rejected, the object remains at its old position and the old configuration is recounted as a new configuration.

In our 2D model of the colloidal system, our potential consists of two parts, the dipolar contribution and the hard-sphere potential. The hard sphere potential is zero for non-

overlapping spheres, and is infinite in the case of overlaps. Thus, any attempted move which generates an overlap is simply rejected and no energy criterion need be tested.

However, the parameter δr_{max}, which determines the size of the move of each object, should be an adjustable parameter during the simulation. If this parameter is too small, most of the objects' moves will be accepted, but the phase space will be explored slowly. Alternatively, if δr_{max} is too large, most of the moves will be rejected and again the phase space will be explored slowly. Therefore, δr_{max} is typically adjusted during the simulation so that about half the moves are accepted. We, however, use a criterion based on the mean square displacement (discussed below) to increase the efficiency with which we explore configuration space.

2.5 Structural Quantities

One goal of MC or MD simulations is to start from unstable configurations and end up with equilibrium configurations. The set of equilibrium configurations, i.e. coordinates of all the particles in the system, in turn is used to generate several quantities that describe the structure of the system. The structural quantities that we calculate are the pair correlation function (radial distribution function), structure factor, fraction of percolation, and cluster size distribution. We also keep track of the mean square displacement, a measure of the dynamics.

2.5.1 Pair Correlation Function

Pair correlation function $g(r)$ is defined as the probability of finding a pair of particles at distance r apart, relative to the probability expected for a completely random distribution (ideal gas state) at the same density. With this definition, $g(r) = 1$ for an ideal gas, and so any deviation of $g(r)$ from unity reflects correlations between the particles. The

theoretical formula of $g(r)$, as given in Eq. 2.17, can be found for the canonical ensemble by integrating the configurational distribution function over the positions of all particles in the system except two [10].

$$g(\vec{r_1}, \vec{r_2}) = \frac{N(N-1)}{\rho^2 Z_{NVT}} \int d\vec{r_3}\ d\vec{r_4}\ ...\ d\vec{r_N} \exp(-\beta\ V(\vec{r_1}, \vec{r_2}, ...\ \vec{r_N})). \tag{2.17}$$

In this equation, N is the total number of particles, ρ is the number density, and Z_{NVT} is the canonical partition function. For numerical calculations, Eq. 2.17 can be written in a discrete formula by taking the ensemble average over pairs, as follows,

$$g(r) = \frac{1}{\rho^2} \left\langle \sum_i \sum_{j \neq i} \delta(\vec{r_i})\ \delta(\vec{r_j} - \vec{r}) \right\rangle = \frac{V}{N^2} \left\langle \sum_i \sum_{j \neq i} \delta(\vec{r} - \vec{r_{ij}}) \right\rangle. \tag{2.18}$$

$g(r)$ is a very useful structural quantity for experimentalists, since neutron and X-rays scattering experiments on the fluids and light scattering experiments on the colloidal suspension give information about $g(r)$. Also, it is useful for theorists and simulators, where the theoretical predictions can be compared with numerical solutions to test theories.

The pair correlation function can also be used for calculating some thermodynamic quantities, such as energy and pressure for a system of interacting particles through Eq. 2.19 for a 3D system or Eq. 2.20 for a 2D system [10],

$$\langle \mathcal{A} \rangle = \left\langle \sum_i \sum_{j>i} a(r_{ij}) \right\rangle = \frac{1}{2} N \rho \int_0^\infty a(r) g(r) 4\pi r^2 dr, \tag{2.19}$$

$$= \frac{1}{2} N \rho \int_0^\infty a(r) g(r) 2\pi r dr. \tag{2.20}$$

Since our model is a 2D one, all the next details are written for a 2D system. The total energy (E) of a pairwise additive system includes two contributions: one comes from the ideal gas energy and second comes from the interaction potential $u(r)$,

$$E = Nk_BT + \pi N\rho \int_0^\infty ru(r)g(r)dr. \tag{2.21}$$

In our simulation, the interaction potential is divided into three different parts, hard sphere, pairwise interaction, and the long range correction potentials. The hard sphere potential contributes nothing to the potential energy since there are no overlaps, but does contribute to the pressure. For radial distance between hard sphere contact r_{min} and r_c (half the box), $g(r)$ is also calculated explicitly. Beyond r_c, the potential is known but $g(r)$ is not. The contribution from $r > r_c$ is important and is often used to correct the energy calculated directly from particles in the simulation box. Eq. 2.21 can then be written as [9, 10, 30],

$$E = Nk_BT + \pi N\rho \left(\int_{r_{min}}^{r_{cut}} ru_{dip}(r)g_{r\leq r_{cut}}(r)dr + \int_{r_{cut}}^{\infty} ru_{dip}(r)g_{r>r_{cut}}(r)dr \right), \tag{2.22}$$

u_{dip} is either stacked (u_s) or staggered (u_g) dipolar potential as presented in Eqs. 2.11 and 2.15. At large distances between the disks, there assumed to be no correlations between the disks and $g_{r>r_{cut}}(r) = 1$, and then Eq. 2.22 can be written as,

$$E = Nk_BT + \pi N\rho \left(\int_{\sigma}^{r_{cut}} ru_s(r)g_s(r)dr + \int_{0.866\sigma}^{r_{cut}} ru_g(r)g_g(r)dr + \int_{r_{cut}}^{\infty} ru_{dip}(r)dr \right). \tag{2.23}$$

Eq. 2.23 offers a way of checking consistency of results. The potential energy calculated directly from simulation should match that obtained through $g(r)$.

The pressure can also be calculated from $g(r)$. We begin with the following equation for the total pressure in a 2D system,

$$P = \frac{Nk_B}{V}T + \frac{1}{V}\langle \mathcal{W} \rangle , \tag{2.24}$$

$\mathcal{W}$ is called the 'internal virial', and it is related with the intermolecular pair virial function $w(r)$ and the interaction potential $u(r)$ according to the following relation,

$$\mathcal{W} = -\frac{1}{2}w(r) = -\frac{1}{2}r\frac{du(r)}{dr}. \tag{2.25}$$

Using Eq. 2.20, the total pressure is,

$$\begin{aligned} P &= \frac{Nk_BT}{V} - \left(\frac{1}{2}\right)\pi\rho\frac{N}{V}\int_0^\infty rw(r)g(r)dr \\ &= \rho k_BT - \left(\frac{1}{2}\right)\pi\rho^2\int_0^\infty r^2\frac{du(r)}{dr}g(r)dr \\ &= \rho k_BT - \left(\frac{1}{2}\right)\pi\rho^2\left(\int_0^\infty r^2\frac{du_{h.s}(r)}{dr}g(r)dr + \int_{r_{min}}^{r_{cut}} r^2\frac{du_{dip}(r)}{dr}g(r)dr\right) \\ &- \frac{1}{2}\pi\rho^2\int_{r_{cut}}^\infty r^2\frac{du_{dip}(r)}{dr}dr \end{aligned} \tag{2.26}$$

This equation is called either the pressure equation or the virial equation. The second term in this equation comes from the hard sphere contribution, and it is difficult to calculate directly from the integration. To simplify solving the hard sphere contribution, we introduce a new function called $y(r)$ as [30],

$$y(r) = \exp[u(r)/k_BT]g(r), \tag{2.27}$$

and the second term of Eq. 2.26 can then be written as,

$$\begin{aligned} P_2 &= -\left(\frac{1}{2}\right)\pi\rho^2\int_0^\infty r^2y(r)\exp\left(-\frac{u_{h.s}(r)}{k_BT}\right)\frac{du_{h.s}(r)}{dr}dr \\ &= \left(\frac{1}{2}\right)k_BT\pi\rho^2\int_0^\infty r^2y(r)\frac{d}{dr}\left[\exp\left(-\frac{u_{h.s}(r)}{k_BT}\right)\right]dr. \end{aligned} \tag{2.28}$$

The function $\exp(u(r)/k_BT)$ is a unit step function for the hard sphere model, therefore, the derivative of this function is a δ-function, and then P_2 equals,

$$\begin{aligned} P_2 &= \left(\frac{1}{2}\right) k_BT\pi\rho^2 \int_0^\infty r^2 y(r)\delta(r - r_{min})dr \\ &= \left(\frac{1}{2}\right) k_BT\pi\rho^2 \lim_{r\to r_{min}^+} r^2 y(r) \\ &= \left(\frac{1}{2}\right) k_BT\pi\rho^2 r_{min}^2 g(r_{min}), \end{aligned} \tag{2.29}$$

and the total pressure equals [10, 30],

$$\begin{aligned} P &= \rho k_BT + \left(\frac{1}{2}\right) k_BT\pi\rho^2 r_{min}^2 g(r_{min}) - \left(\frac{1}{2}\right)\pi\rho^2 \int_{r_{min}}^{r_{cut}} r^2 \frac{du_{dip}(r)}{dr} g(r)dr \\ &- \frac{1}{2}\pi\rho^2 \int_{r_{cut}}^\infty r^2 \frac{du_{dip}(r)}{dr} dr \\ &= \rho k_BT + \left(\frac{1}{2}\right) k_BT\pi\rho^2\sigma^2 g_s(\sigma) + \left(\frac{1}{2}\right) k_BT\pi\rho^2 (0.866\sigma)^2 g_g(0.866\sigma) \\ &- \left(\frac{1}{2}\right)\pi\rho^2 \int_\sigma^{r_{cut}} r^2 \frac{du_{dip}(r)}{dr} g_s(r)dr - \left(\frac{1}{2}\right)\pi\rho^2 \int_{0.866\sigma}^{r_{cut}} r^2 \frac{du_{dip}(r)}{dr} g_g(r)dr. \\ &- \frac{1}{2}\pi\rho^2 \int_{r_{cut}}^\infty r^2 \frac{du_{dip}(r)}{dr} dr \end{aligned} \tag{2.30}$$

2.5.2 Structure Factor

Basically, structure factor (or geometrical structure factor) is a mathematical quantity that describes how the material scatters incident waves. It is a very useful quantity to study the material structure for neutron and X-rays scattering. The structure factor can be derived by using both of Bragg and Laue conditions, and the final formula is given by [10, 31],

$$S(\vec{K}) = \frac{1}{N}\left\langle \sum_{j=1}^{N} \exp(i\vec{K}.\vec{r_j}) \sum_{j=1}^{N} \exp(-i\vec{K}.\vec{r_j}) \right\rangle. \tag{2.31}$$

In this equation, $\vec{K}$ is the wave vector in the reciprocal lattice and equals $\vec{K} = \vec{k} - \vec{k'}$ that happens in a case of constructive interference. $\vec{k}$ is the wave vector associated with the incident light, while $\vec{k'}$ is the wave vector associated with the scattered light. Moreover, structure factor also represents a Fourier transformation of pair correlation function, where ($|\vec{K}| = 2\ \pi/|\vec{r}|$). In fact, both structure factor and pair correlation function have the same data about the material structure, but each one is calculated in a different space. Therefore, it is easy to predict the shape of structure factor if you already know the shape of pair correlation function and vice versa. In computer simulation, there is one restriction about calculating the structure factor: $\vec{K}$ must equal a whole number of $2\pi/L$ in each direction as follows [10],

$$\vec{K} = \frac{2\pi}{L}(n_x, n_y, n_z). \tag{2.32}$$

L_B is the simulation box length, and n_x, n_y, n_z are integers.

2.5.3 Percolation

A system is called percolated when we have at least one cluster that spans the entire system. Percolation is an important feature in colloidal suspension because it has an effect on some physical properties such as viscosity, mean cluster size, and shear modulus [4]. As the system approaches percolation, the viscosity and mean cluster size increase rapidly. In the percolation regime, the system spanning cluster confers a finite shear modulus to the system [4].

The impact of percolation depends on the strength of the bonds between particles. Predicting when percolation will occur in a given model using analytical methods is not an easy task, and is often given over to computer simulation. However, using computer simulation requires determining the maximum distance between any two particles to be

considered neighbours. The following relation is commonly used: $d = \sigma(1 + \epsilon)$, where d is the distance between any two particles, σ is the particle's diameter, and ϵ is a small number chosen to account for numerical calculations. If the distance between any two particles is less than d, the two particles are considered in the same cluster; otherwise, they are not [26]. After that, we duplicate the simulation box in all directions. If the largest cluster connects with its copy and the duplicated system, the configurations is considered to be percolated, otherwise, the configuration is considered to not be percolated [32]. In our model we choose d to be the location of the maximum in $u_g(r)$.

Moreover, percolation is a sensitive quantity to parameters in the system such as volume fraction, temperature, and the bonds between the particles. There are some studies about the effect of these parameters on the percolation. One of these studies involves finding the critical volume fraction ϕ_c, where the percolation starts in the system. Then, ϕ_c can be used in someway to calculate some physical quantities such as conductivity, capacity, and permittivity [26].

2.5.4 Cluster Size Distribution

The cluster size distribution is a statistical quantity that gives the average number of clusters n_s of size s (containing s particles). Through statistical mechanics, n_s is related to the work of forming a cluster of size s through,

$$\Delta F(s) = -k_B T \ln\left(\frac{n_s}{n_1}\right), \tag{2.33}$$

where n_1 is simply the number of single particles or monomers. ΔF tells us about the appearance of new phase, and is, for example, a central quantity in classical nucleation theory. In this thesis, we use the appearance of a local minimum in ΔF at $s > 0$ to indicate the appearance of a new phase. This method was used in Ref. [33] to detect the

appearance of the cluster phase in a cluster-forming colloidal suspension.

2.5.5 Mean Square Displacement (MSD)

The mean square displacement ($\langle \Delta r(t)^2 \rangle$) is an important quantity since it gives an idea about the dynamical motion of the particles in the system. Actually, mean square displacement (MSD) is difficult to calculate experimentally or theoretically, instead it can be calculated only using computer simulation. However, MSD is a good indicator of the material structure. For example, if the system is solid, the MSD saturates to a finite value, while if the system is liquid, the MSD grows linearly with time. In general, MSD can be expressed as follows [9],

$$\left\langle \Delta r(t)^2 \right\rangle = \frac{1}{N} \sum_{i=1}^{N} \Delta r_i(t)^2. \tag{2.34}$$

In molecular dynamic simulation, MSD can be used to find the diffusion coefficient D [9], where

$$D = \lim_{t \to \infty} \frac{1}{6t} \left\langle \Delta r(t)^2 \right\rangle. \tag{2.35}$$

In Monte Carlo simulation, MSD only determines if the system is diffusive or not, and we can not find the diffusion coefficient because we do not deal with a real time. In addition, MSD gives an idea about changing the diffusion by increasing or decreasing the temperature or volume fraction. In MC and MD simulations, the system is considered a diffusive fluid if we can get a linear region of a length at least one diameter. Otherwise, we can not consider the system as a diffusive fluid, instead it could be solid or solid-like material.

We also use the MSD to roughly optimize δr_{max}, doing so by simulating a handful of state points spanning our isochores. We simulate each of the state points using a range of

δr_{max}, and select the δr_{max} that gives the longest MSD for a given number of MC steps. Generally, the optimal δr_{max} is not a strong function of T or area fraction. As a result, we fix δr_{max} to be 0.15σ.

Chapter 3

Structural Properties of a 2D Dipolar System (Phase Diagrams)

In this chapter, we present our simulations of our 2D model for dipolar system, where we account for the cases of chains being stacked or staggered with respect to each other. We present data over a range of temperature and area fraction in the context of possible phase diagrams proposed for similar systems in the literature. We explain the determination of the boundaries in the phase diagram by using different models such as the two state model, structure factor calculations, and cluster distribution.

3.1 Model and Simulation Details

In the previous chapter, we introduce both stacked and staggered dipolar interactions. We also show that the staggered dipolar interaction is attractive at short distances and repulsive at large distances, while the stacked dipolar interaction is repulsive at any distance. We simplify the motion of chains in the $z-$direction by allowing chains to either be level with the bottom, or displaced up by half a diameter. The staggered interaction is the energetically preferred arrangement, while the stacked naturally arises for second nearest neighbours as illustrated in Fig. 3.1. From this figure, chain 1 and chain 2 (as well as chain 2 and chain 3) interact via the staggered dipolar interaction. As a result, chain 1 will interact with chain 3 via stacked dipolar interaction.

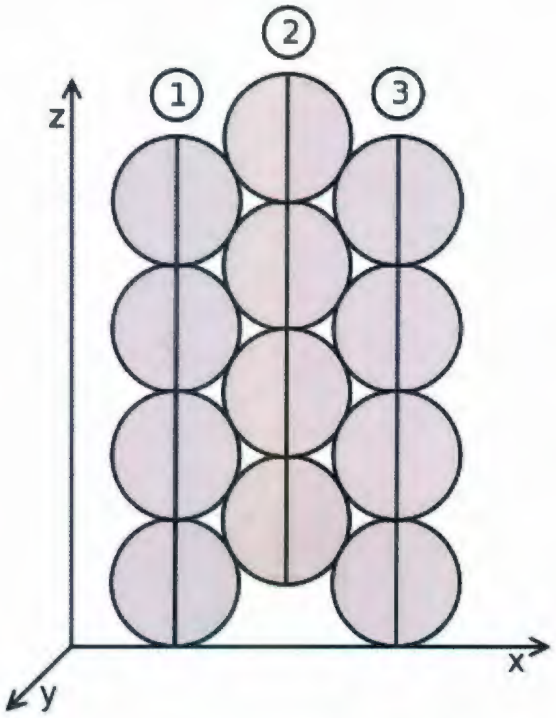

Figure 3.1: The coexistence of stacked and staggered dipolar interactions in a dipolar system. Chain 1 and chain 2 (as well as chain 2 and chain 3) interact via the staggered dipolar interactions, while chain 1 interacts with chain 3 via stacked dipolar interaction.

In our work, we assume that all colloids in each chain are fixed, so each chain moves in the system as one unit. In other words, the x and y positions are the same for all colloids in a single chain. Also, we assume that all the chains have the same length. Therefore, the system can be modeled as a 2D system of interacting hard disks, where each disk represents a chain of dipolar particles viewed along z-axis. Thus, the chains in Fig. 3.1 are exactly the same disks shown in Fig. 3.2.

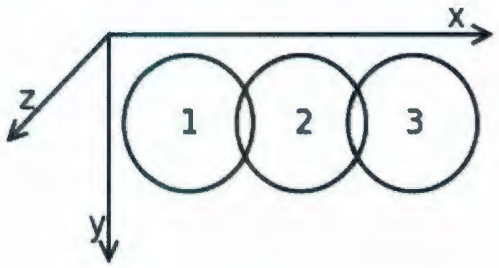

Figure 3.2: These disks represent the same chains as in Fig. 3.1 viewed along z-axis.

In our model, we identify the stacked and staggered dipolar interactions by labeling each disk by either 1 or -1. In the initial configuration, 50% of disks are labeled by 1 and the other 50% are labeled by -1. Before calculating the potential energy between any two disks in the system, we multiply each of the two labels together. If the product equals 1, the two disks interact via the stacked dipolar interaction, whereas if the result equals -1, the two disks interact via the staggered dipolar interaction. As a result, around half of the dipolar interactions in the system will be stacked and the other half will be staggered.

Permanently, fixing the label of each disk is not very helpful. For example, if a bunch of disks met together and they have the same label, they will not attract each other as it happens in the real system. Instead, they will repel each other due to the stacked dipolar interaction. In order to avoid this problem, during every trial MC displacement we give a 50% probability that the disk will also switch identity. The calculation of the energy of the trial configuration takes into account the proposed identity. In this way, our model will capture the local structure presented in the real system.

We perform MC simulation of $N = 2500$ disks. We start simulations at different values of area fractions ($A = 1\%, 10\%, 20\%, 30\%, 40\%, 50\%, 60\%, 70\%$) and a high temperature ($k_BT = 5$), where $k_B = 1$, where $A = (N\pi\sigma^2)/(4L_B^2)$. We initialize particle positions by placing them on a square lattice, which results in an unstable, high-energy configuration. The total number of MC steps per particle is different from one system to another, but it is in the range of $[10^6, 10^7]$. During the simulation, we save the value of the potential energy and the configuration after each 1000 MC steps per particle.

In the beginning of the simulation, the potential energy drops significantly, then it decays more slowly. After sufficient time, it fluctuates about a constant equilibrium energy value. At this stage, the system is considered a stable system at equilibrium, where

each disk can still move, generating a set of equilibrium configuration. From this set, we calculate structural quantities such as the pair correlation function, structure factor, cluster size distribution, fraction of percolating clusters, and mean square displacement. The calculation process is done by choosing 1000 different configurations for the same system at equilibrium, and then calculating the structural quantities averaged over these configurations. An additional requirement for establishing equilibrium is that the mean square displacement must exceed $1\sigma^2$, starting from a time after initial transients seen in the potential energy subside. Otherwise we must keep the simulation running in order to give the disks a chance to move more.

Once the results are accepted, we consider the final configuration at $T = 5$ as the initial configuration for a new simulation at $T = 4$. Again, we wait for the new equilibrium state in order to calculate the structural quantities. As the temperature decreases, and hence the thermal energy available to break bonds decreases, the number of MC steps required to reach equilibrium increases. We continue the process of decreasing the temperature and re-equilibrating for all area fractions until it takes longer than about two weeks to equilibrate. Fig. 3.3 presents all equilibrating state points. The lowest temperature that we studied is different from one isochoric system to another depending on speed of equilibration. For example, $T_{min}(A = 0.01) = 0.4$, while $T_{min}(A = 0.7) = 1.8$.

3.2 Computer Simulation Results

3.2.1 Energy and Mean Square Displacement

Fig. 3.4(a) shows the potential energy at equilibrium for area fraction 70%. From this figure, we obviously observe that the potential energy is constant at equilibrium, and it decreases by decreasing the temperature.

On the other hand, the MSD represents the exploration of configuration space, or

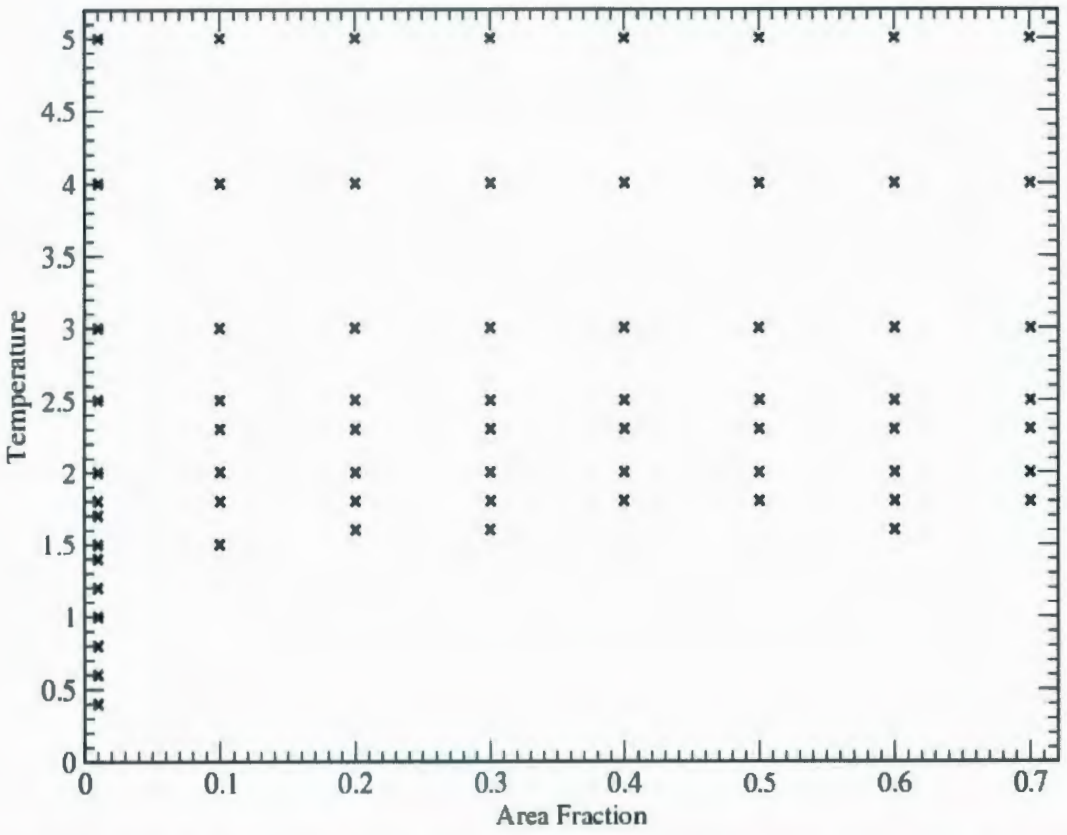

Figure 3.3: Each x sign in this figure represents a computer simulation experiment at specific values of temperature and area fraction.

structural relaxation. As the temperature decreases, the relaxation becomes slower. Fig. 3.4(b) shows the MSD behaviour as a function of the number of MC steps per particle at different values of temperature and at area fraction equal to 70%. The orange lines represent the MSD behaviour for an ideal diffusive fluid. We observe from the figure that this behaviour is roughly linear with slope one at temperatures $T = 5$ and 4, which means that the system at these temperatures is diffusive. As the temperature decreases, the slope of MSD decreases, which means that the diffusion of the particles decreases and the relaxation of the structure becomes slower. It is worthwhile mentioning that at very low temperatures, such as $T = 1.8$, or 2, most disks are trapped within clusters. Therefore, it is difficult for any disk to leave the cluster because the disks do not have enough thermal energy to overcome the attractive potential. At the same time, our model

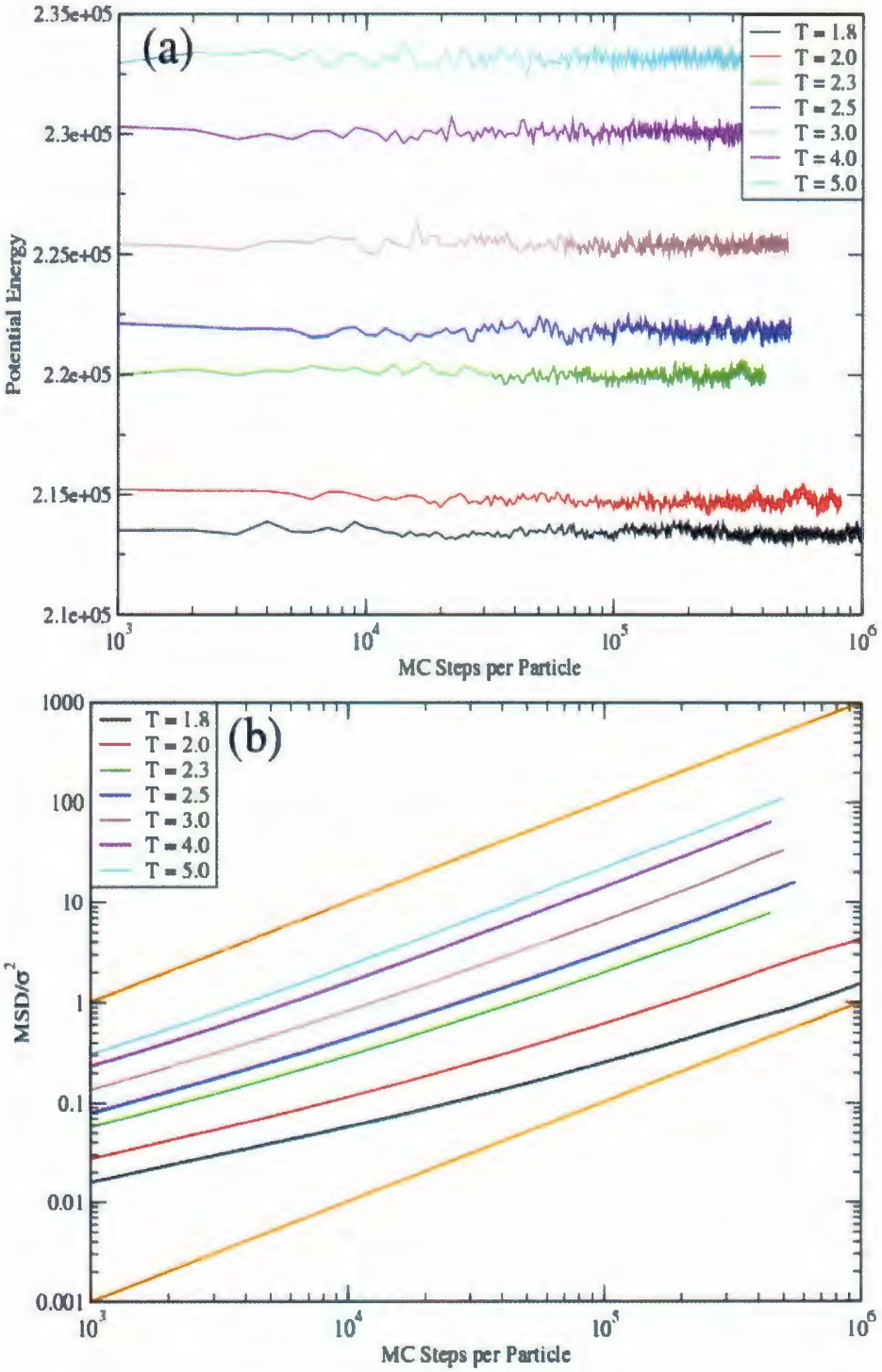

Figure 3.4: Fig. (a) and Fig. (b) represent the energy behaviour and mean square displacement as functions of MC steps at equilibrium for an area fraction that equals 70% and different values of temperature.

does not allow for the cluster to move as a one unit, instead, it deals with each disk alone. It would be worthwhile finding more advanced MC schemes that would overcome the rate limiting step of bond breaking and would allow faster equilibration.

3.2.2 Pair Correlation Function and Structure Factor

Fig. 3.5(a) shows the pair correlation function ($g(r)$) for an isochoric system of 70% area fraction. In this figure, the first peak reflects the correlation between first nearest neighbours at $r/\sigma = 0.866$, as presented by the red line in Fig. 3.5(b). The second peak reflects the correlation for the second nearest neighbour at $r/\sigma = 1.225$, as presented in the green line in Fig. 3.5(b). The third and fourth peaks are belong to the correlation between the disks at $r/\sigma = 1.732$ and 2.5, as illustrated by the blue and orange lines, respectively, in Fig. 3.5(b). We observe from Fig. 3.5(c) that as the temperature decreases, $g(r)$ progressively develops peaks at r/σ corresponds to the nearest neighbours' rank.

We conclude from the figure that there is no significant long-range correlation between the disks for $2.3 < T < 5.0$, i.e. the system is an isotropic fluid. At $T = 2.0$, we observe little peaks at further distances which means that the disks acquire greater long range order, i.e. have periodic order for longer distances. A further significant increase in peak heights happens when we decrease the temperature to $T = 1.8$, which means that at this temperature the disks become more and more correlated through the bonds formation. The significant difference in peak height over a fairly small range in T may occur as a result of a phase transition, but may simply be a continuous change. In the rest of this section, we introduce some possible methods to check whether or not there is a phase transition.

While $g(r)$ is very well suited to understanding particle correlations on the scale of a few particle diameters, the structure factor $S(q)$ more readily sheds light on longer scale

structuring of the fluid. We use $S(q)$ as a qualitative measure of cluster formation and to study the correlation between the clusters.

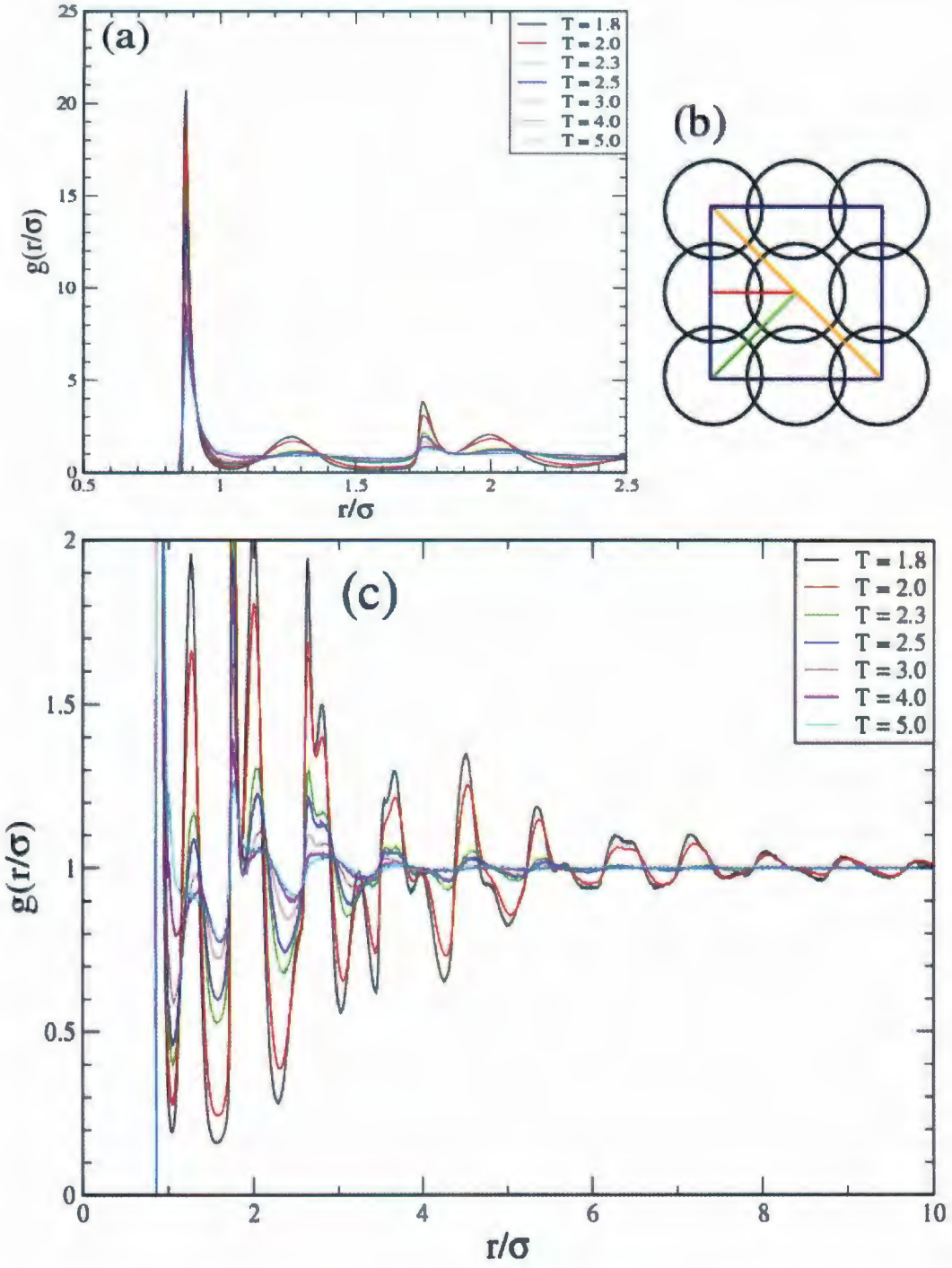

Figure 3.5: Fig. (a) shows the height of the first four peaks of $g(r)$ at area fraction equal to 70%, and (b) is a geometric figure to explain the position of the first four peaks. Fig. (c) shows $g(r)$ extended to further distances.

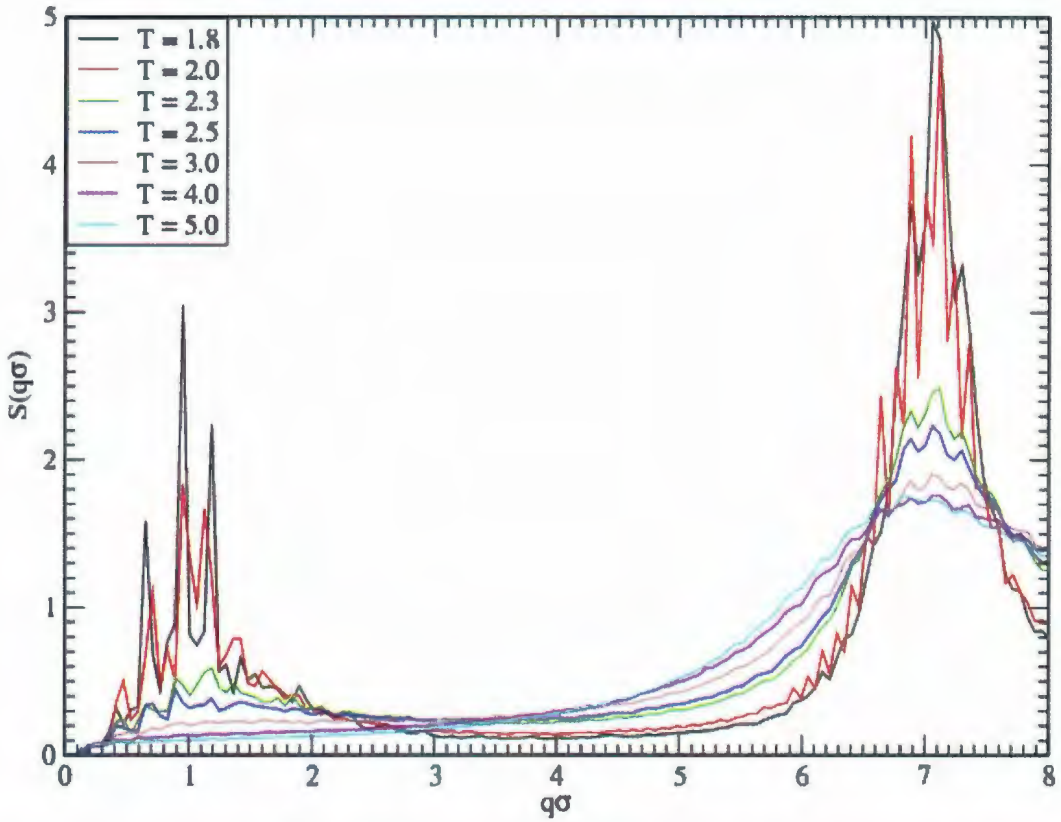

Figure 3.6: The structure factors calculated at equilibrium for an area fraction that equals 70% and a wide range of temperature.

Fig. 3.6 shows $S(q)$ for several T at 70% area fraction. We observe from the figure that $S(q)$ progressively develops a peak at wave vectors q associated with distances in real space, where $q = 2\pi/r$. In fact, obtaining a peak at small wave vectors ($q\sigma = 1$) is a strong confirmation of clustering in the system. Mainly, this peak reflects the nearest neighbour cluster-cluster distance. We can conclude from the figure that there is only weak clustering, or rather only weak cluster correlation at temperatures $T \in [2.3, 5]$. At $T = 2.0$, the peak becomes notable, which means that the clusters are more regularly spaced. At $T = 1.8$, the height of the peak increases significantly, and this supports the possibility of having a phase transition near this temperature. However, for a system at constant volume (or area) the phase change proceeds in general through a

region of coexistence. Therefore, to distinguish between a continuous change and a phase transition, more evidence must be gathered.

The second peak in $S(q)$, at $(q\sigma \approx 7)$, provides information about the local structure of the cluster. At $T > 2.3$, there are short, rounded, peaks belonging to the string fluid structure before forming the clusters. At $T = 2.0$, the amplitude of the peak increases significantly, and the peak shows strong local ordering. At $T < 2.0$ the system continues to be more periodic on the length scale of nearest neighbours. The jaggedness of the curves at low T is a reflection of the difficulty of sampling independent configurations, i.e. of equilibrating the system.

3.2.3 Potential Energy along Isochores

We plot in Fig. 3.7 the potential energy as a function of T for our eight isochores. Fig. 3.7(a) shows the data for $A = 1\%$, which exemplifies the behaviour we might expect: an increasing slope as the liquid is cooled from the high T limit, and then a nearly linear regime at the lowest T as the system forms well separated ordered clusters. The linear behaviour arises because most particles will be participating in a harmonic solid, for which $U = Nk_BT$. How the potential energy makes this change may give some indication of the nature of the transformation.

As T is lowered, if there is a first order transition with little or no hysteresis, the potential energy will be that of the pure fluid until the temperature reaches the upper T limit for coexistence. At this point there is a break in slope and the potential energy is a combination of liquid and solid energies weighted according to the amount each of which should be present. At the lower coexistence T, there should again be a break in slope as the potential energy follows that of the solid. Hysteresis will only serve to make changes in energy more visible. If there is a second order transition, there should be a break in

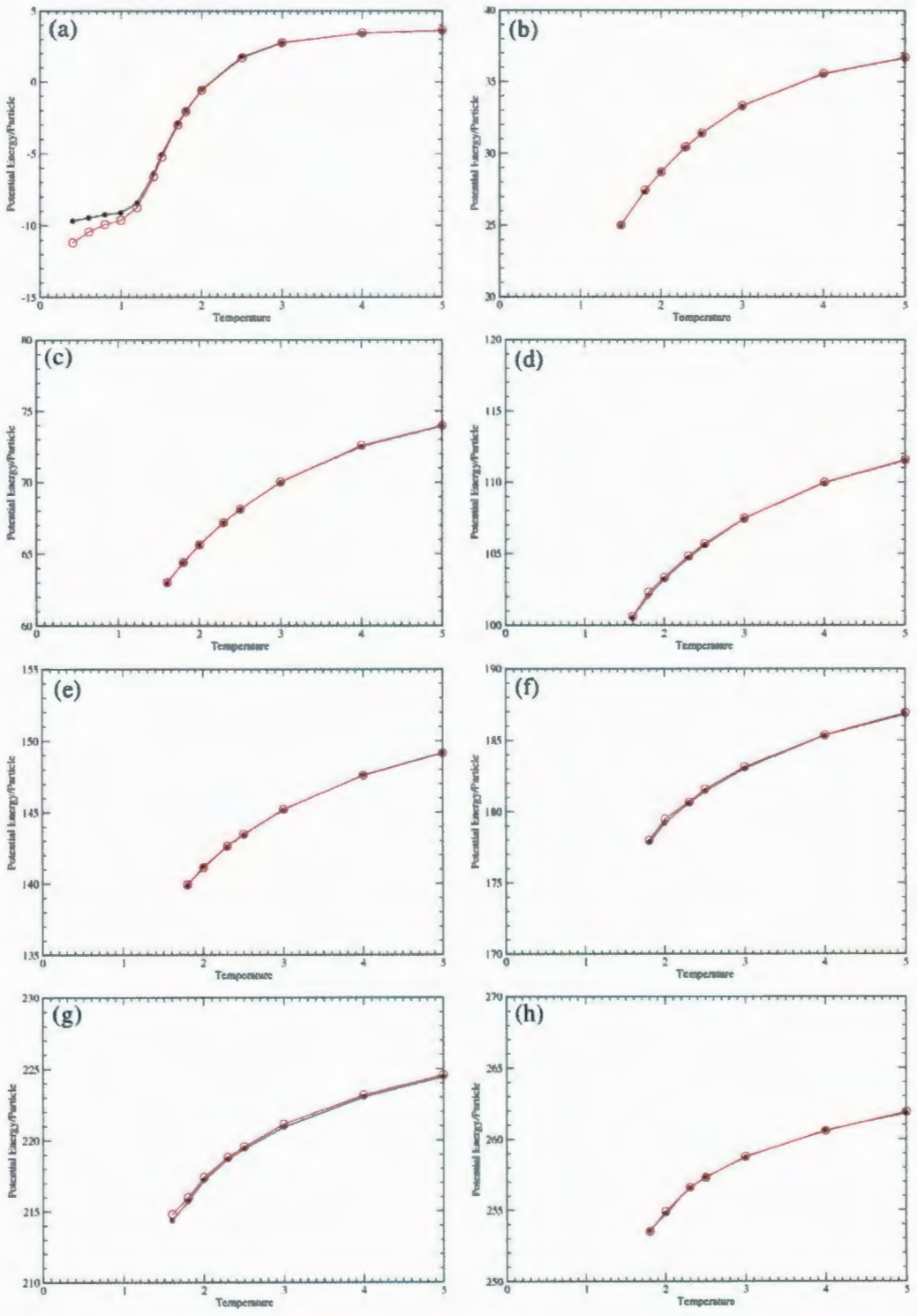

Figure 3.7: The black curves in this figure represent the potential energy that measured during the simulations, while the red curves represent the potential energy as calculated from $g(r)$ data at area fractions (a) A=1%, (b) A=10%, (c) A=20%, (d) A=30%, (e) A=40%, (f) A=50%, (g) A=60%, , (h) A=70%.

slope at a single temperature. For finite systems this transition will be smoothed out, and may appear as in the third scenario of a smooth change in the liquid's properties. For $A = 1\%$, there seems to be no break in slope. For higher area fraction up to and including 50%, there also appears to be no break in slope, even though we have probed deeply enough in T to see quite well-formed clustering, as we will see later. There may be evidence for a break in slope at $A = 70\%$. The lowest three data points seem to be roughly linear, at variance with the higher T behaviour, but this interpretation is tenuous.

Fig. 3.7 plots both the potential energy obtained directly from the pair potential during the simulation (plus tail correction), as well as indirectly from $g(r)$. In general, the agreement is rather good, and the discrepancy between the two methods can be used as an uncertainty estimate. The only place where there is a large discrepancy is for $A = 1\%$ at low T. The difficulty here is obtaining $g(r)$ with good sampling at all length scales. Here, we would treat the direct simulation data as trustworthy and work to improve $g(r)$ for the future.

3.2.4 2-State Model

In order to gain a better understanding of the nature of the clustering seen in our system, we use a simple two-state model [34]. Basically, there are two states available to a system with an energy difference ΔE, and the relative degeneracy of the higher energy state is Ω. As applied to our system, the lower energy, lower degeneracy state is a bond formed between two disks, while the higher state corresponds to broken or unfilled bond. The prediction of the model for the potential energy is

$$U = NE_1 + \frac{Nk_B\Omega\Delta E \exp(-\beta\ \Delta E)}{1 + \Omega \exp(-\beta\ \Delta E)} \tag{3.1}$$

while the heat capacity is given by

$$C_V = \frac{N k_B \Omega \beta^2 \Delta E^2}{\left(1 + \Omega \exp\left(-\beta \Delta E\right)\right)^2} \tag{3.2}$$

(see Appendix B for a derivation). A peak in heat capacity is predicted by the model, but the model, for example, does not predict the energy behaviour of a finite Ising model. We therefore consider it as a way to differentiate a continuous change and a second order transition in a finite system.

A Fit to Eq. 3.1 is shown in Fig. 3.8(a), and appears to be rather good. Fig. 3.8(b) shows the resulting C_V using Eq. 3.2, but using the fit parameters obtained from Eq. 3.1. The discrepancy at low T (below the C_V peak) can be accounted for by considering the fact that clusters behave to a first approximation as a harmonic solid. For a 2D harmonic solid, $C_V/Nk_B = 1$, which we see hold for our system (see Fig. 3.8). The fact that the two-state model captures the energetics of clustering is evidence that the clustering does not occur through a phase transition, but rather is a continuous process, at least at $A = 1\%$.

3.2.5 Pressure

MC simulations provides only configurational information, and it is therefore necessary to use $g(\sigma^+)$ and $g(0.866\sigma^+)$ in eq 2.30 to calculate the hard sphere contribution to the pressure. It is there essential that we have established that we recover the energy using $g(r)$. Calculating the pressure for our system is crucial in the sense that in a region of coexistence, the pressure along an isotherm is constant.

In Fig. 3.9, we plot the pressure as a function of area fraction for various isotherms. We see that the pressure is no where constant, this result is inconsistent with the phase coexistence reported in [8], at least in the usual sense of bulk phase separation. What we

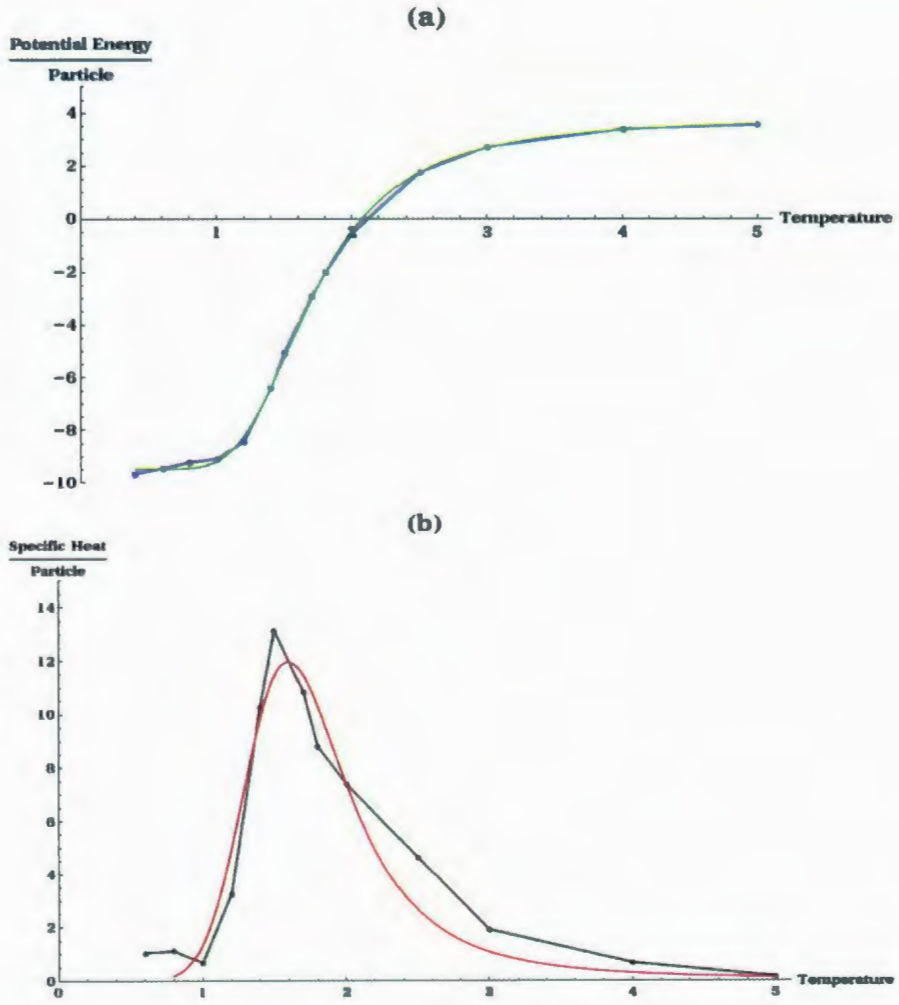

Figure 3.8: Fitting the computer simulation data of both potential energy and specific heat at area fraction that equals 1% with Eqns. B.5 and B.6.

see instead is an inflection (indicating a compressibility maximum), or possible break in slope, near $A = 40\%$. We see later that this feature coincides with the percolation line.

3.3 Phase Diagram

Fig. 3.10 shows the phase diagram for a 3D dipolar system converted to a 2D one that depends on temperature and area fraction, as obtained by Hynninen *et al.* [8]. The conversion factor from volume fraction to an area fraction for a dipolar system that composed of chains spanning from top to bottom equal to 3/2, and hence $A = 3/2\phi$, where

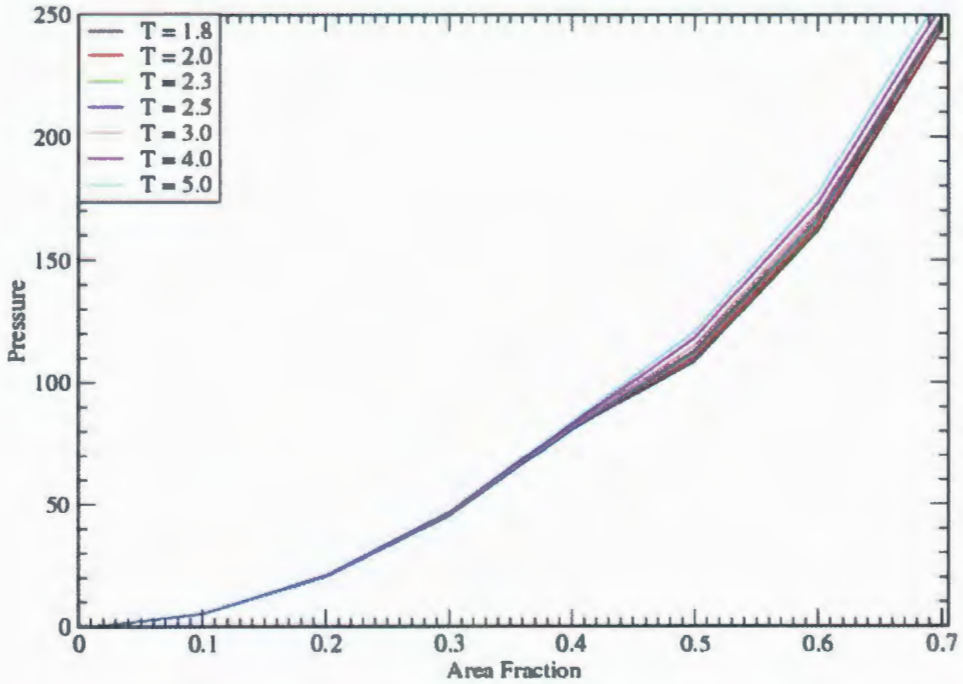

Figure 3.9: shows pressure behaviour as a function of area fraction for different ischoric systems.

A and ϕ are the area and volume fractions, respectively. We observe from this figure that the structure is a string (fluid) at $A < 70\%$ and $T > 0.3$. Decreasing the temperature below $T = 0.3$ does not change the fluid structure until it reaches the blue line where the fluid switches to a fluid-bct coexistence. We also observe that the general structure at a high packing fraction is a bct structure with less dependence on temperature.

Fig. 3.11 shows the phase diagram for a cluster-forming colloidal system affected by two competing interactions, depletion attraction and electrostatic repulsion, as obtained by Toledano *et al.* [33]. We observe from the figure that the general structure at high temperature and low area fraction is a fluid. Decreasing the temperature until it reaches the blue line switches the structure to a cluster phase. We can conclude from the blue line that the appearance of the cluster phase depends on the area fraction, appearing at higher T for higher area fraction. We also observe from the figure that increasing

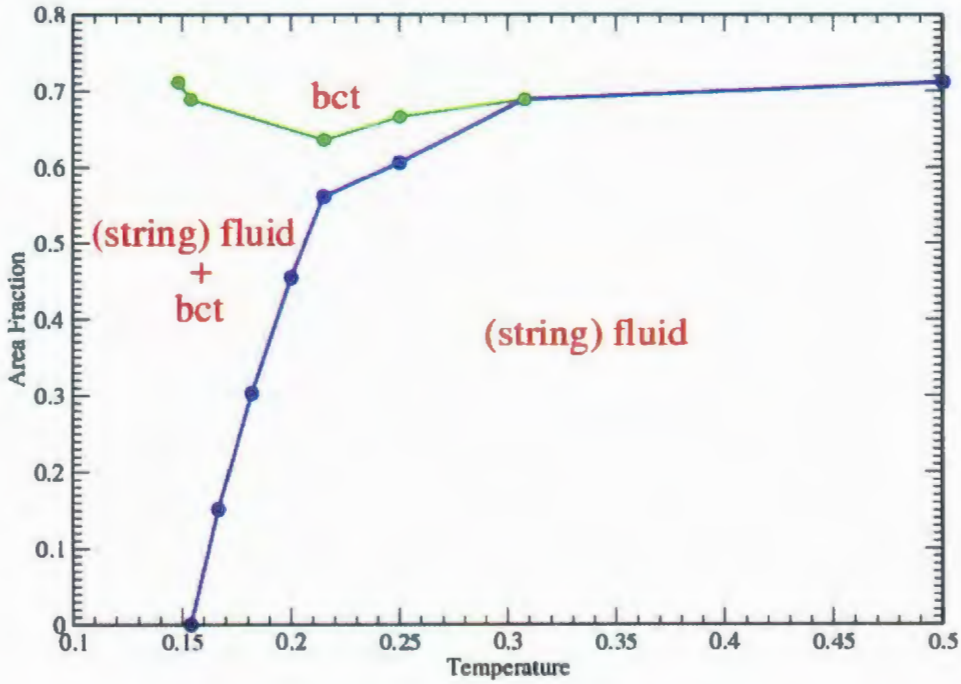

Figure 3.10: shows the phase diagram for dipolar rods system as a function of area fraction and temperature as obtained by Hynninen *et al.* adapted from [8].

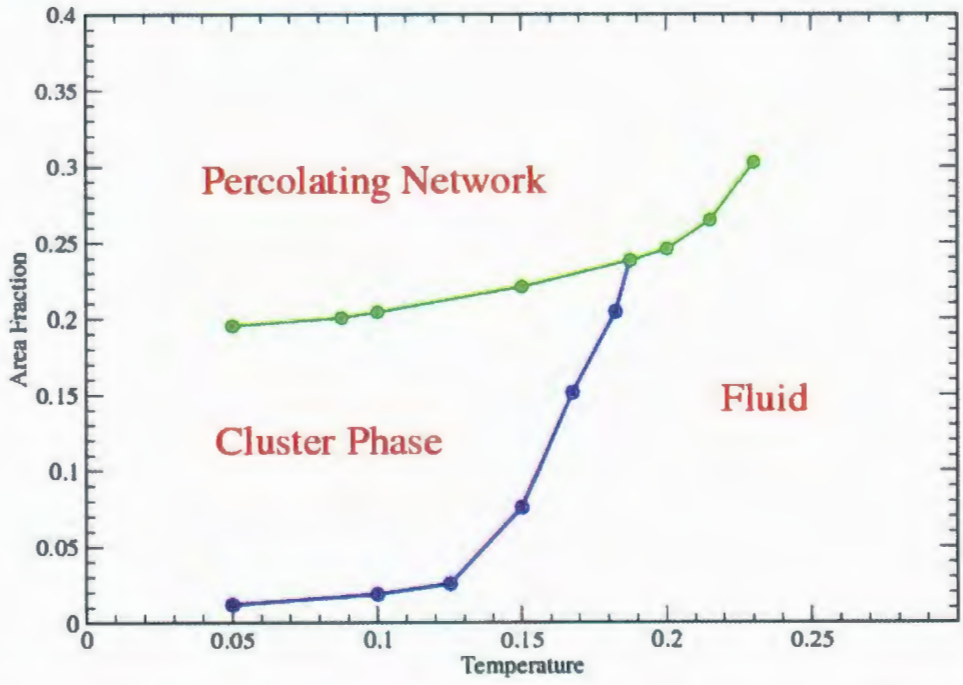

Figure 3.11: shows the phase diagram as adapted from [33] for a colloidal system with short-range depletion attraction and long-range electrostatic repulsion.

the area fraction until it reaches the green line switches both the fluid and the cluster phase to a percolating structure. The percolation line in this figure depends also on the temperature.

Fig. 3.12 shows our phase diagram for dipolar rods system as a function of temperature and area fraction. The solid blue line is a border that separates the fluid and cluster phase regions. Following Ref. [33], the line is defined along each isochore by the T at which $F(n)$ (the work of forming a cluster of size n) has at least a local minimum at some $n > 1$. The uncertainties in the figure are actually bounds on this temperature. The data for $F(n)$ are shown in the next section. The green line is the percolation line that is defined by state points that have a 50% probability of containing a spanning cluster, see Fig. 3.13. The dashed green line represents a reminder that the percolation line extends to lower temperatures, and separates the cluster phase region from the percolation network.

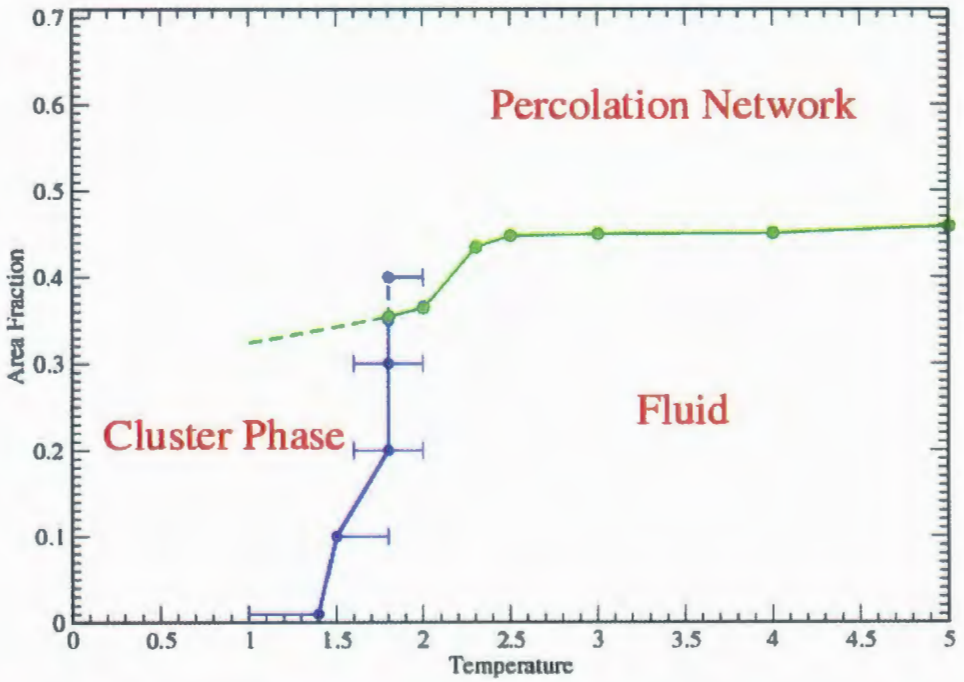

Figure 3.12: Phase diagram for dipolar rods system as a function of area fraction and temperature as obtained from our simulation data.

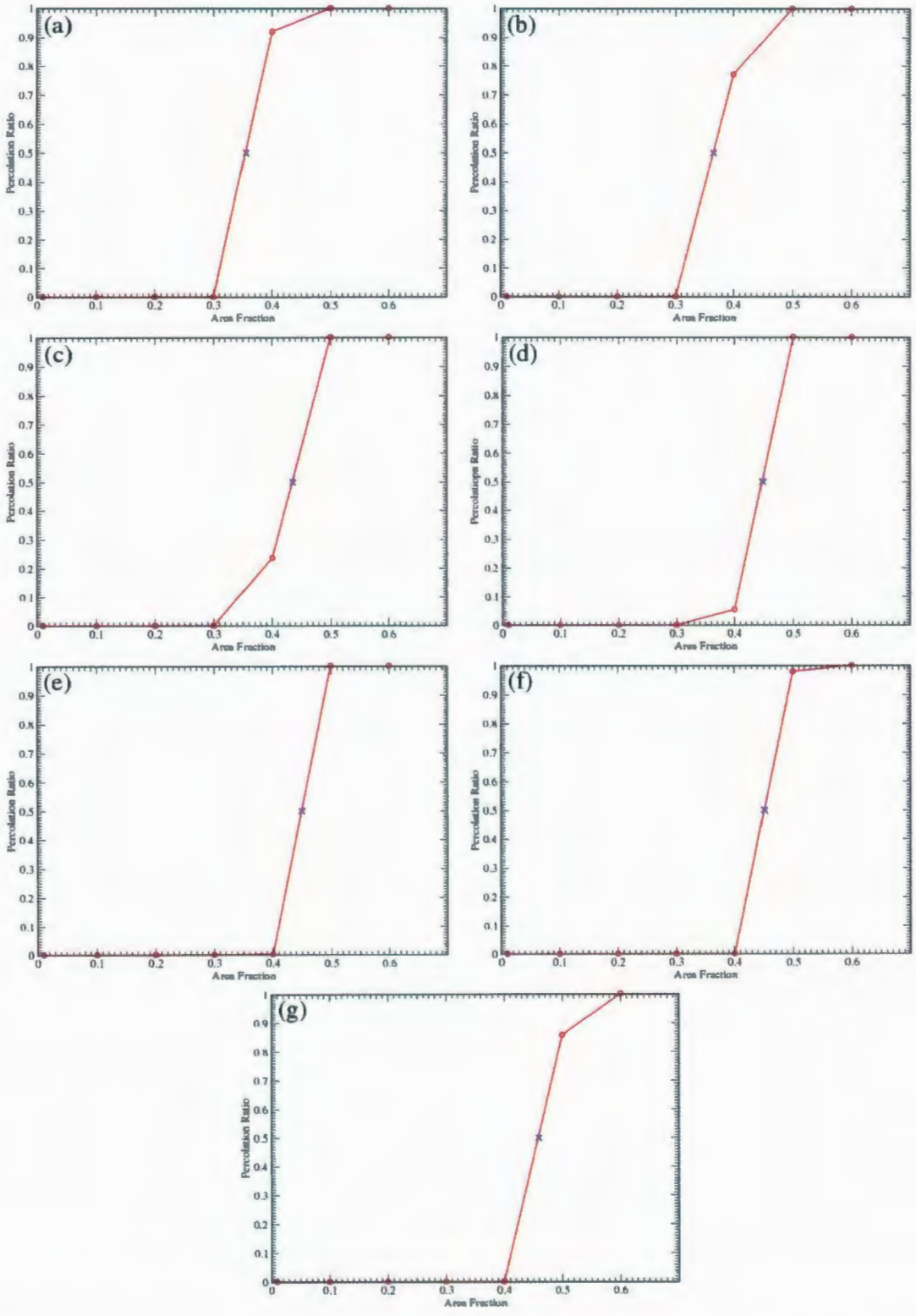

Figure 3.13: The percolation ratio as a function of area fraction at temperatures (a) T=1.8, (b) T=2.0, (c) T=2.3, (d) T=2.5, (e) T=3.0, (f) T=4.0, (g) T=5.0.

The two phase diagrams from the literature provide an interesting basis for comparison. Qualitatively, our model differs from and shares common features with those behind the other phase diagrams. The difference between ours and that of Hynninen is that ours is 2D with chains always formed, while their is a 3D model with chains only formed at low T. In other words, the system at high temperature could be either dispersed colloid or system of very short chains. In our model, we perform the simulation with 50 particles in each chain even at very high temperature. Therefore, we expect to see the cluster phase and the fluid-bct coexistence at temperatures much higher than those temperatures recorded in Fig. 3.10. On the other hand, the phase diagram presented in Fig. 3.11 is not for a dipolar system. However, in the regime where chains are well formed, both models should yield very similar results. That is, if their interpretation is correct, we should also see phase coexistence at low to moderate area fraction once crystallite become common.

The model behind Fig. 3.11 is one of competing attraction and repulsion resulting in clustering. The clusters they we see, however, are not crystallite (but this fact alone is not sufficient to abandon the idea of coexistence since the coexistence could be one between liquid and gas). It is not clear what kind of transition the cluster phase line represents, or whether it is simply the case of an unambiguous convenient thermodynamic demarcation separating the fluid into two regions with qualitatively different limiting behaviours.

3.4 Isochoric Data

We present isochoric data in Figs. 3.14-3.29, including snapshot configurations, $g(r)$, $S(q)$ and $F(n)$ where appropriate. At area fractions 1%, the configuration changes from a string fluid to compact cluster phase of size four, where the system becomes one composed of only clusters at $T = 1.0$. $g(r)$ at this area fraction does not show long range correlations

between the disks. At area fraction 10%, the system behaves similar to the system of 1% area fraction except that the cluster size is bigger here and the cluster phase appears at higher temperature. $g(r)$ also shows longer range correlation between the disks.

The clusters at area fractions 20% and 30% tend to grow in one dimension with thickness about 2 or 3 disks. Here, we also can distinguish the appearance of the cluster phase from $F(n)$. $g(r)$ shows longer range correlation between the disks by either increasing the area fraction or decreasing the temperature. $S(q)$ shows the correlation between the clusters and how the clusters become more equally spaced by decreasing the temperature. At area fractions from 40% to 70%, $g(r)$ shows longer and longer range correlation between the disks, and the second peak of $S(q)$ at $q\sigma \approx 7$ becomes higher, which means that the local structure of the clusters becomes more compact. $F(n)$ at high area fractions does not capture the cluster phase because the clusters will be percolating, and the system becomes one composed of only very big clusters.

Here, we briefly point out some features worth noticing. Snapshots from $A = 30\%$ and $A = 40\%$ bear the lowest T at a strong resemblance to the pictures in Figs. 1.5(a) and 1.5(b), respectively (nominally 23% and 38% area fractions), although we do not perform quantitative comparison. Also notable are the large peaks in $g(r)$ and $S(q)$ corresponding to nearest neighbour separation indicating crystallite structure. However, the strong peaks seem to bear no impact on the smoothness of the potential energy curves in Fig. 3.7. Phase separation is accompanied by a large peak in $S(q)$ at $q = 0$. In our case, we see a peak at finite q, a hallmark of clustering.

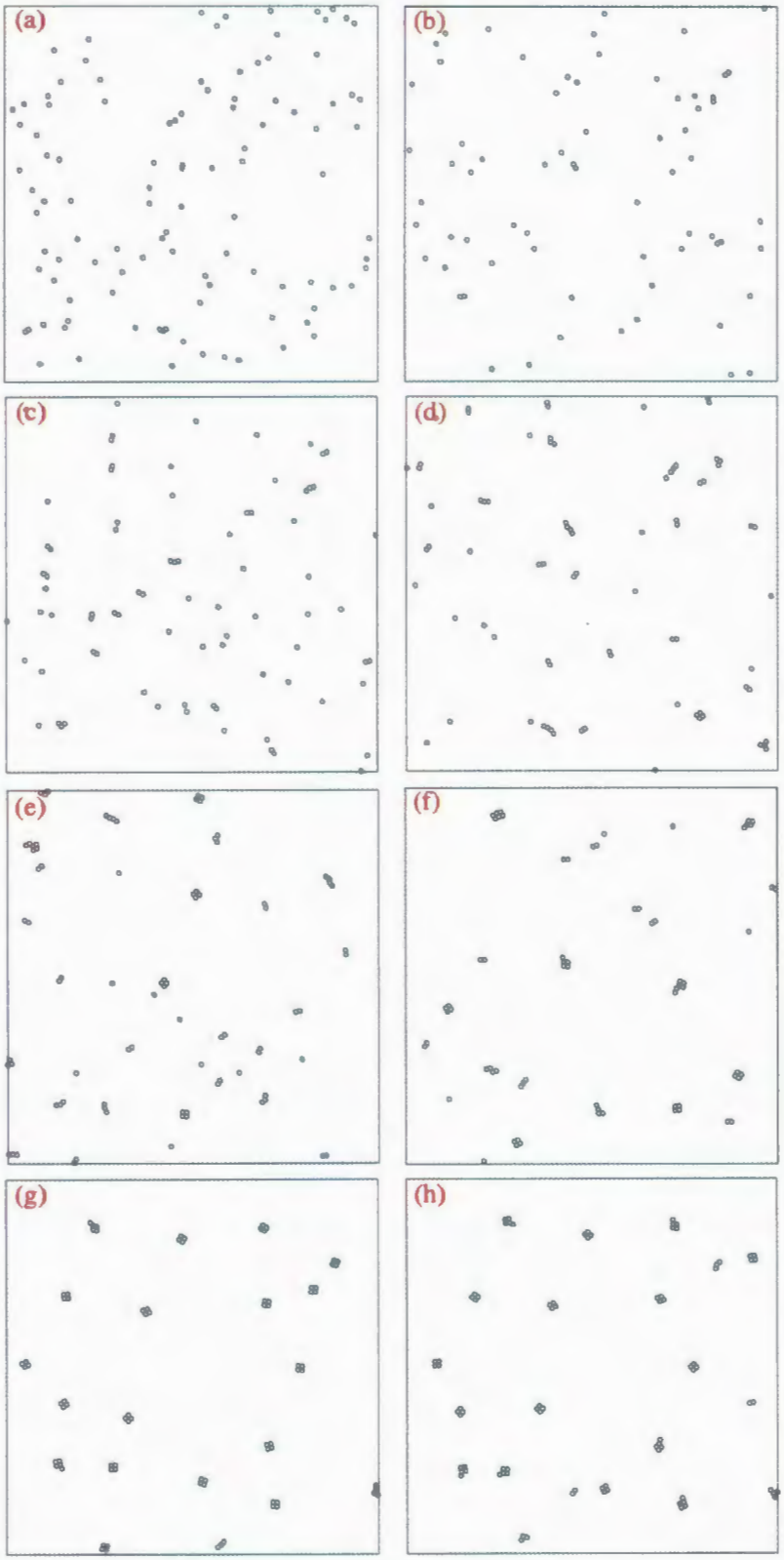

Figure 3.14: Stable configurations for an isochoric system of an area fraction that equals $A = 1\%$ and temperatures (a) T = 5.0, (b) T = 3.0, (c) T = 2.0, (d) T = 1.8, (e) T = 1.5, (f) T = 1.4, (g) T = 1.0 and (h) T = 0.6. One quarter of the simulation box is shown for visibility.

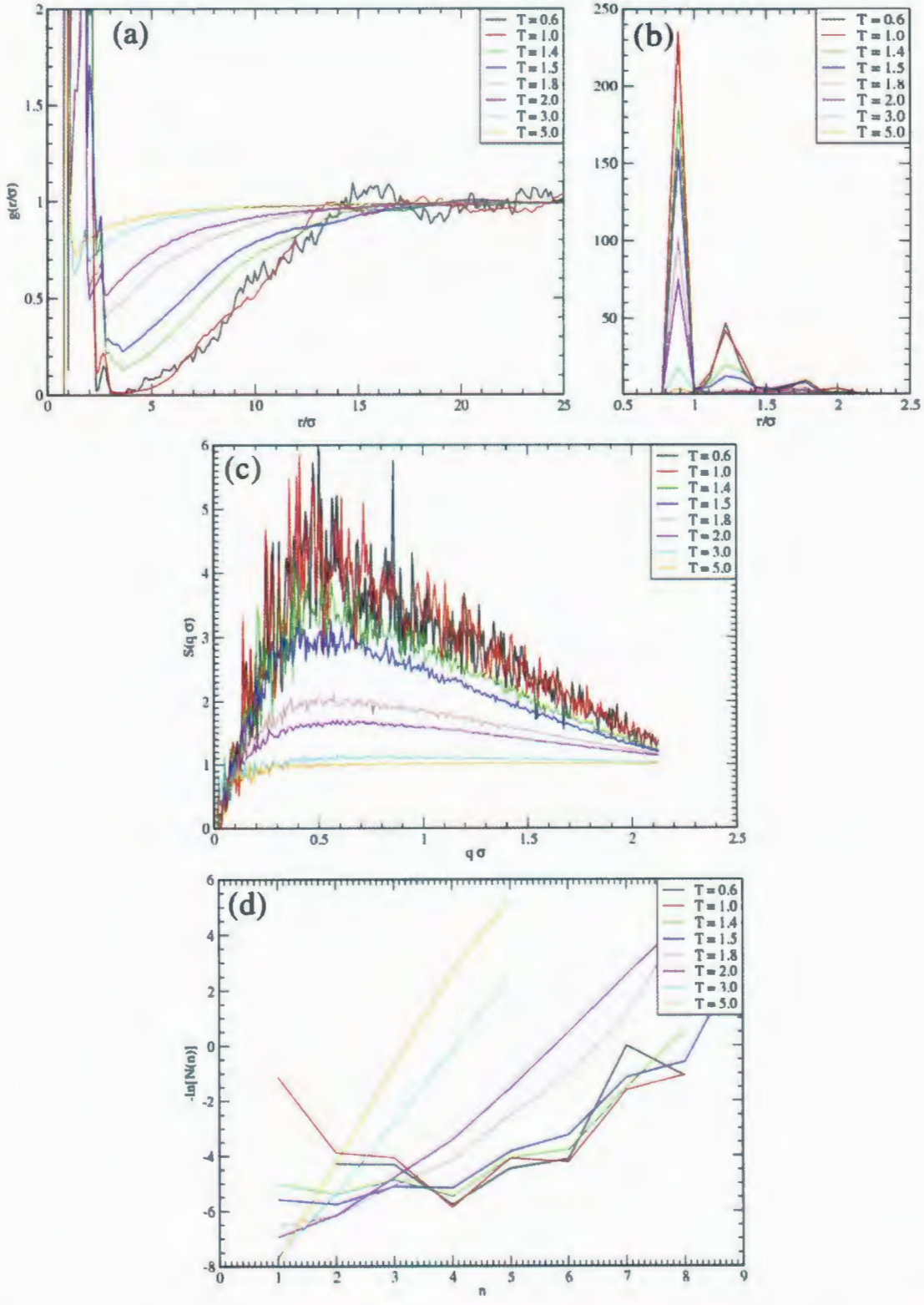

Figure 3.15: Fig. (a) shows $g(r)$ for an area fraction that equals $A = 1\%$, while Fig. (b) shows the height of the first few peaks. Fig. (c) shows the structure factor for the same area fraction, and Fig. (d) shows the work done on the system to form clusters.

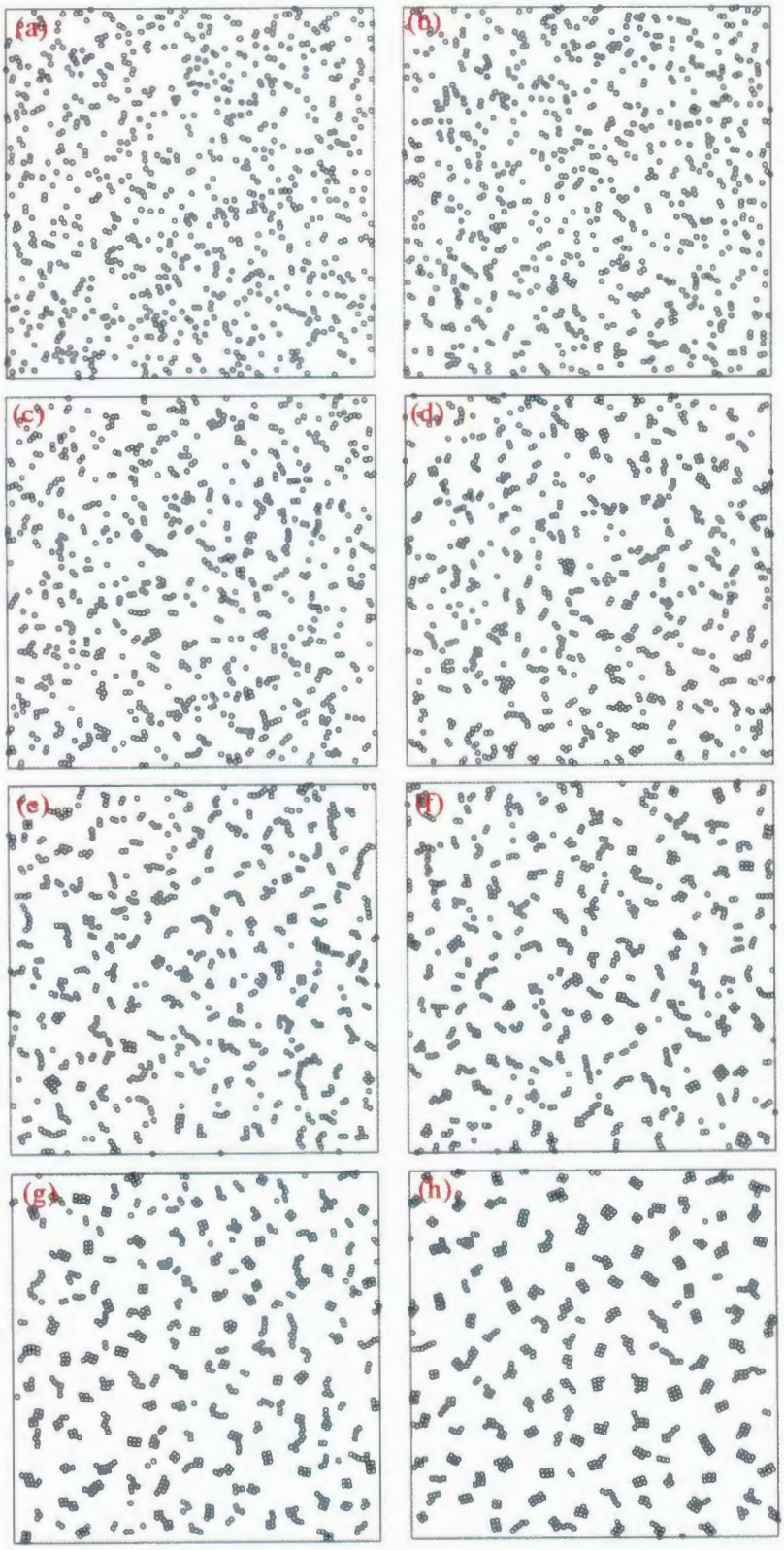

Figure 3.16: Stable configurations for an isochoric system of an area fraction that equals A = 10% and temperatures (a) T = 5.0, (b) T = 4.0, (c) T = 3.0, (d) T = 2.5, (e) T = 2.3, (f) T = 2.0, (g) T = 1.8 and (h) T = 1.5. One half of the simulation box is shown for visibility.

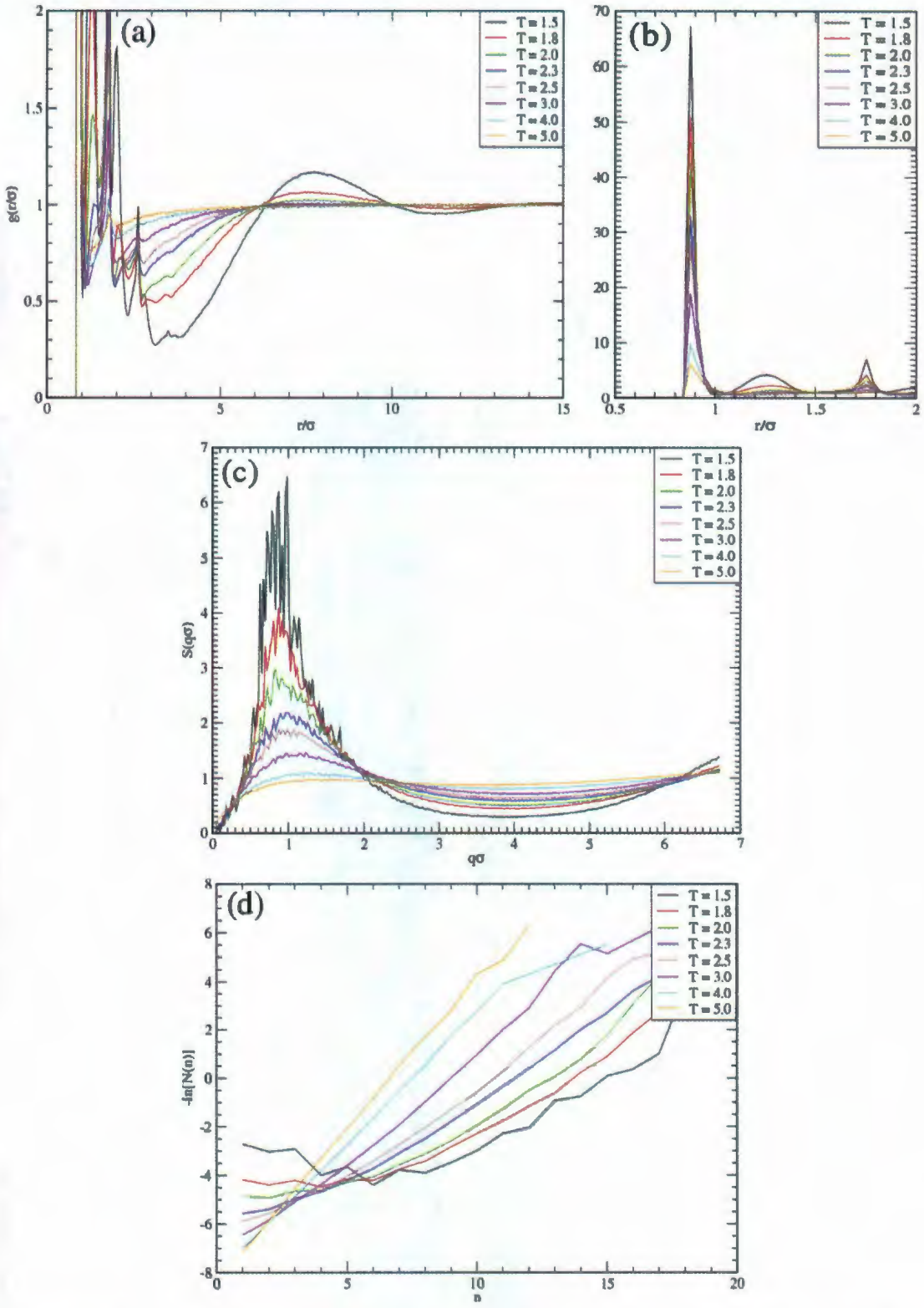

Figure 3.17: Fig. (a) shows $g(r)$ for an area fraction that equals $A = 10\%$, while Fig. (b) shows the height of the first few peaks. Fig. (c) shows the structure factor for the same area fraction, and Fig. (d) shows the work done on the system to form clusters.

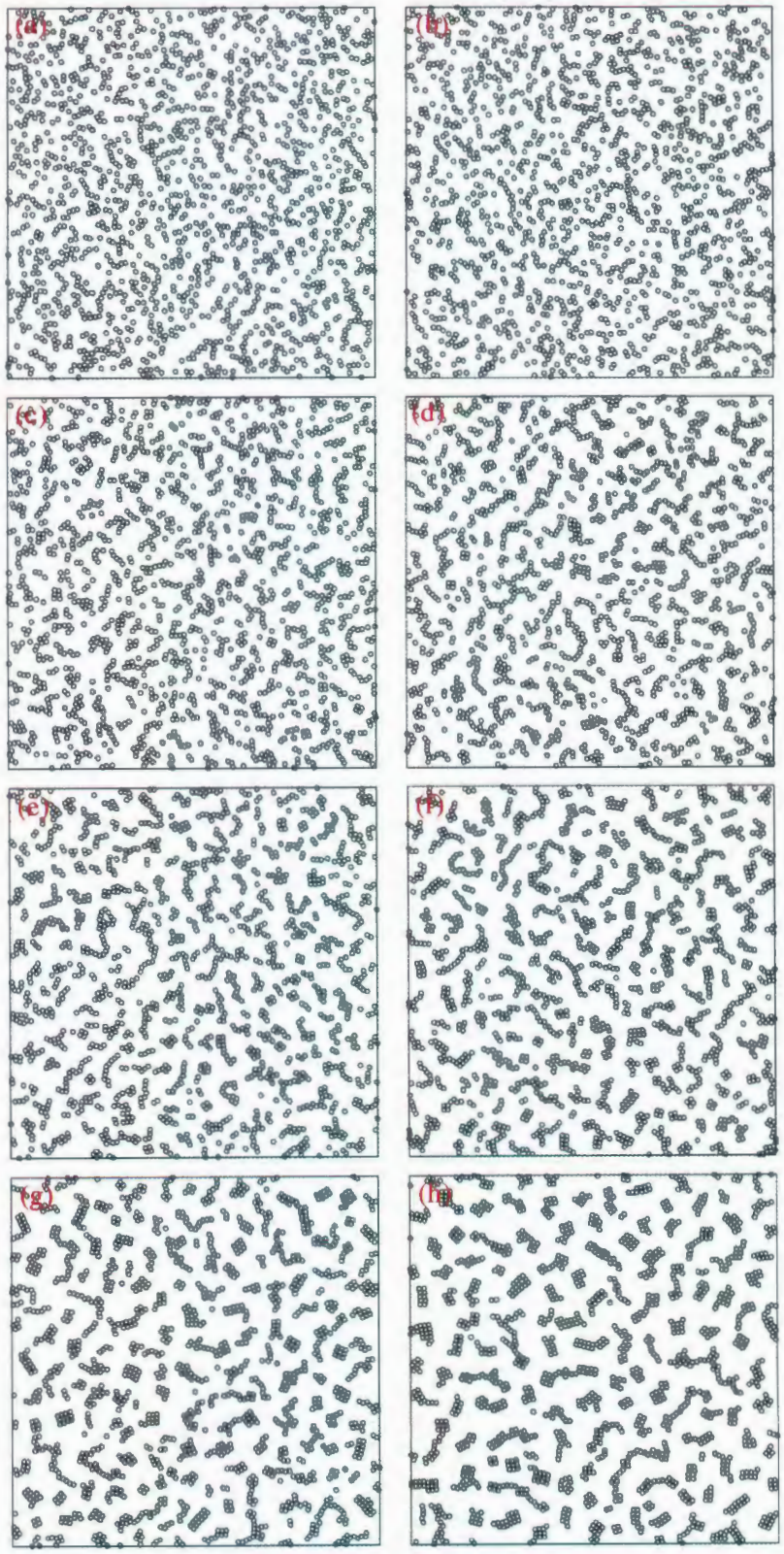

Figure 3.18: Stable configurations for an isochoric system of an area fraction that equals $A =$ 20% and temperatures (a) T = 5.0, (b) T = 4.0, (c) T = 3.0, (d) T = 2.5, (e) T = 2.3, (f) T = 2.0, (g) T = 1.8 and (h) T = 1.6.

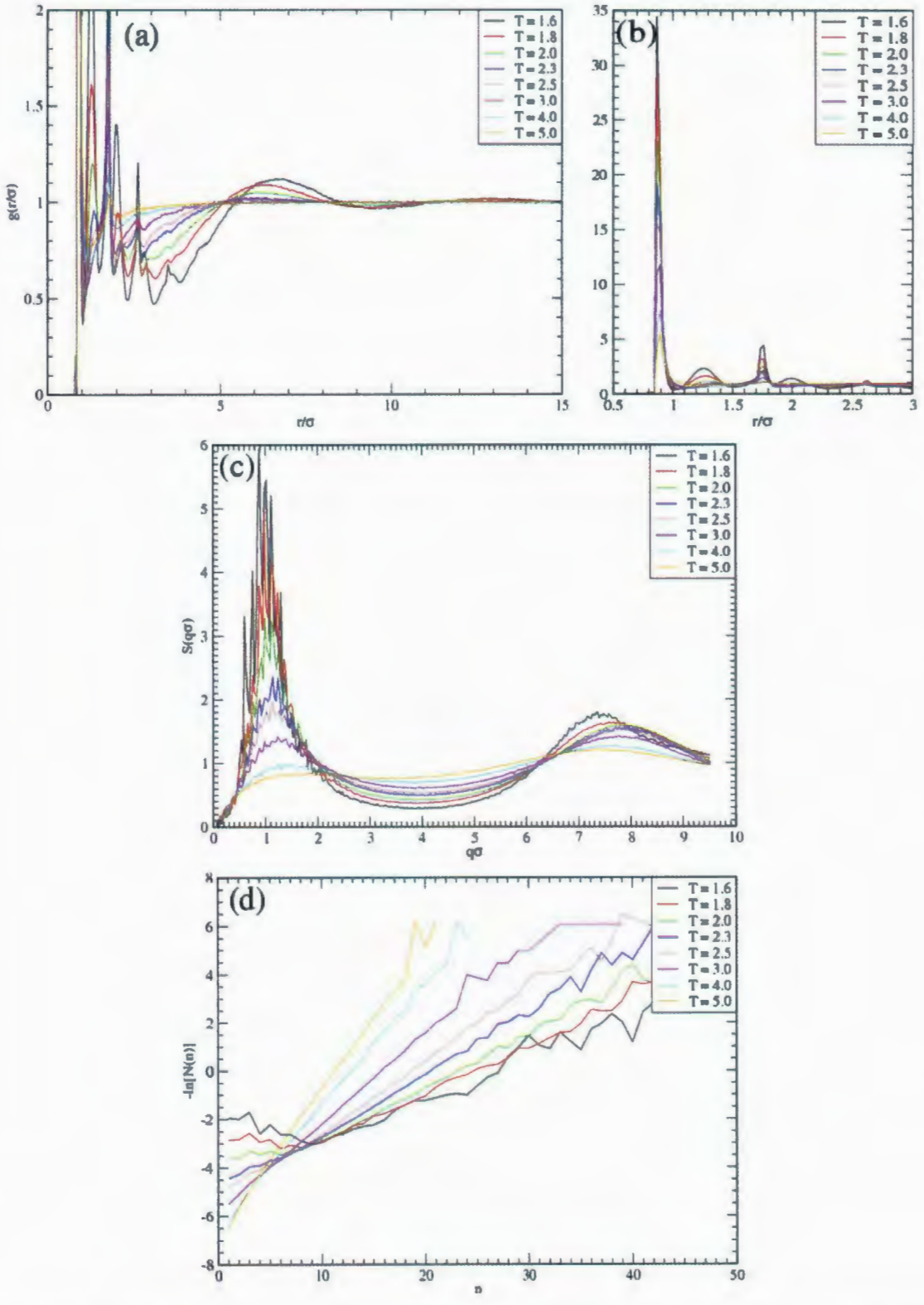

Figure 3.19: Fig. (a) shows $g(r)$ for an area fraction that equals $A = 20\%$, while Fig. (b) shows the height of the first few peaks. Fig. (c) shows the structure factor for the same area fraction, and Fig. (d) shows the work done on the system to form clusters.

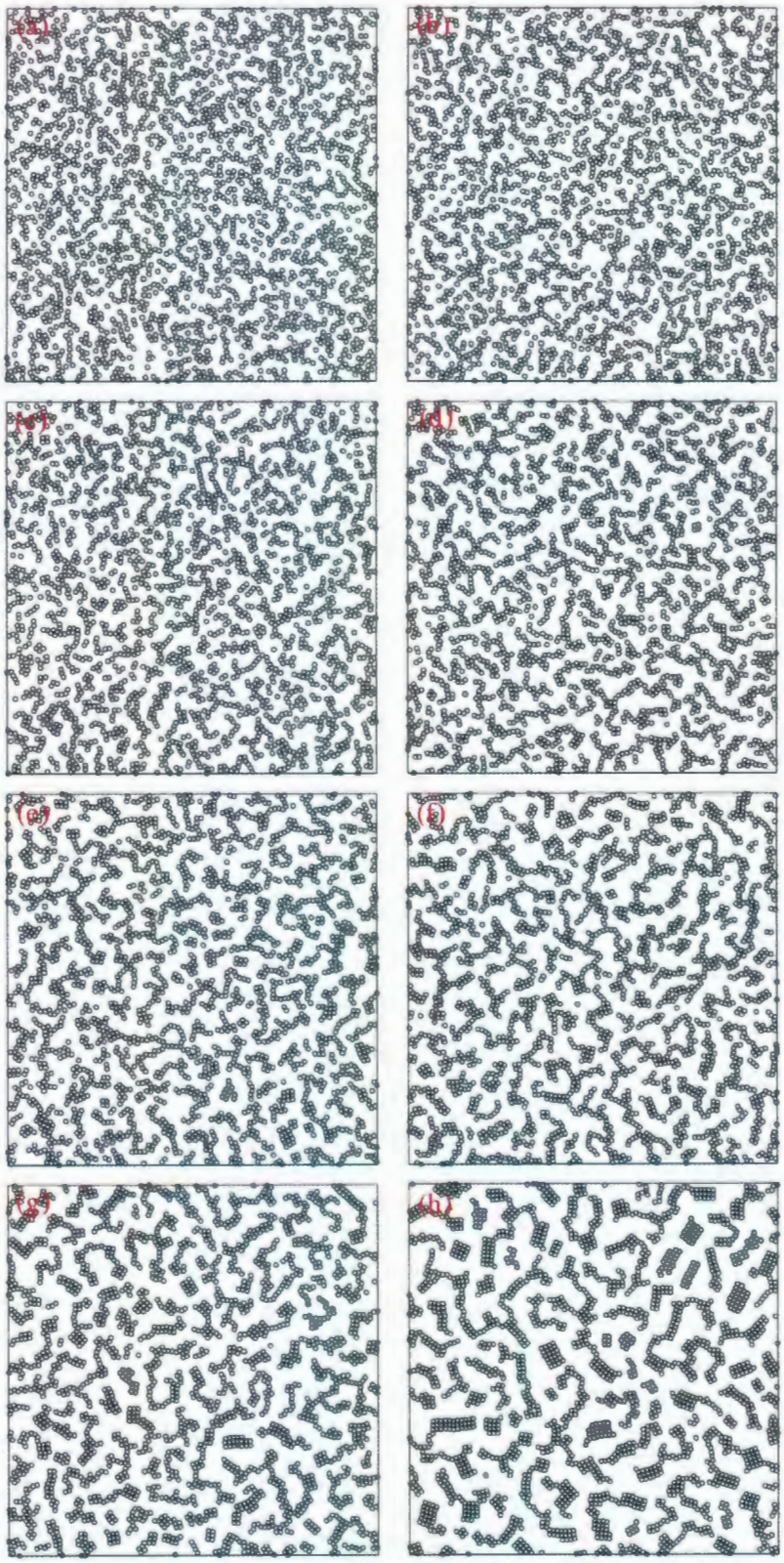

Figure 3.20: Stable configurations for an isochoric system of an area fraction that equals $A =$ 30% and temperatures (a) T = 5.0, (b) T = 4.0, (c) T = 3.0, (d) T = 2.5, (e) T = 2.3, (f) T = 2.0, (g) T = 1.8 and (h) T = 1.6.

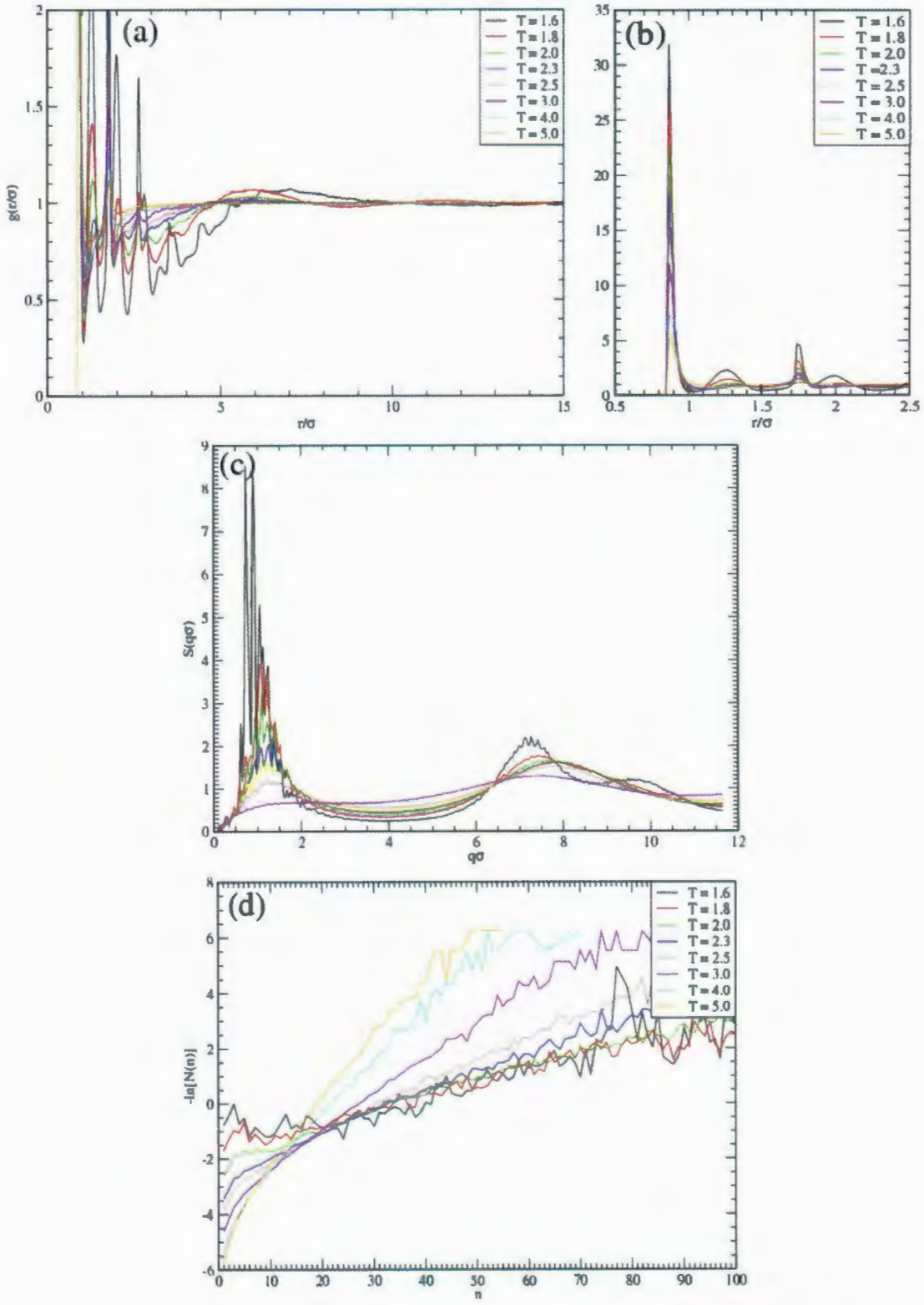

Figure 3.21: Fig. (a) shows $g(r)$ for an area fraction that equals $A = 30\%$, while Fig. (b) shows the height of the first few peaks. Fig. (c) shows the structure factor for the same area fraction, and Fig. (d) shows the work done on the system to form clusters.

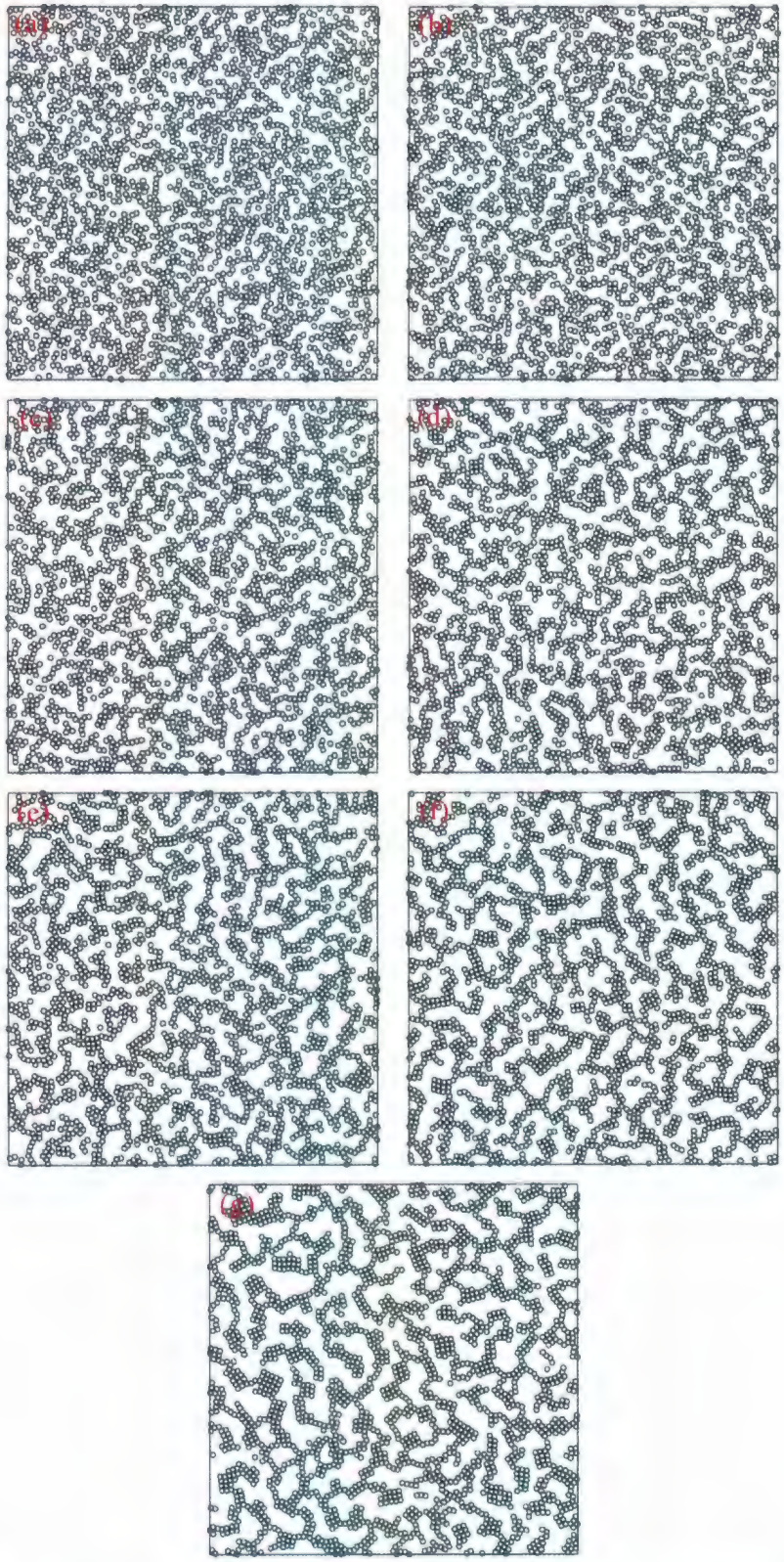

Figure 3.22: Stable configurations for an isochoric system of an area fraction that equals $A =$ 40% and temperatures (a) T = 5.0, (b) T = 4.0, (c) T = 3.0, (d) T = 2.5, (e) T = 2.3, (f) T = 2.0 and (g) T = 1.8.

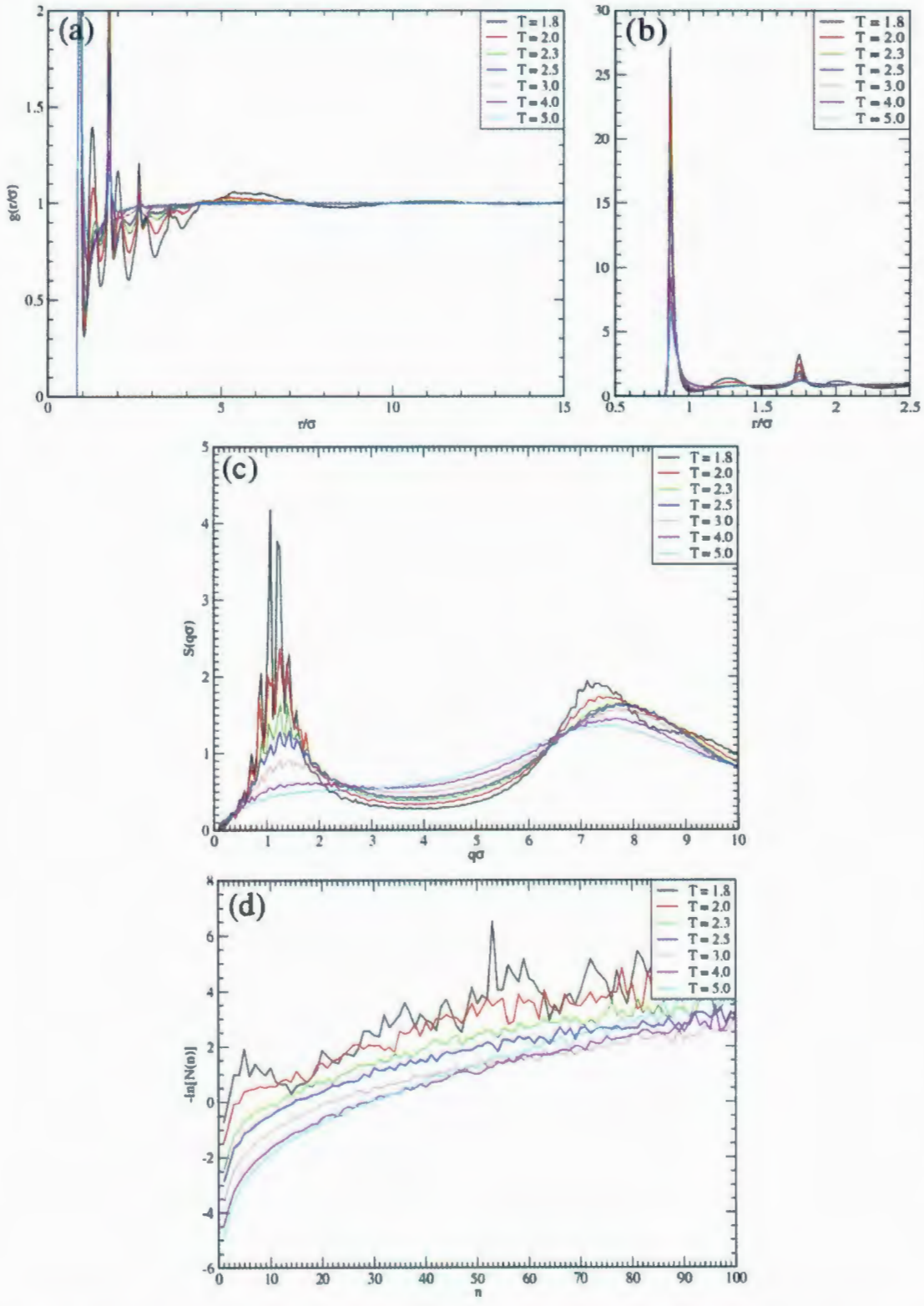

Figure 3.23: Fig. (a) shows $g(r)$ for an area fraction that equals $A = 40\%$, while Fig. (b) shows the height of the first few peaks. Fig. (c) shows the structure factor for the same area fraction, and Fig. (d) shows the work done on the system to form clusters.

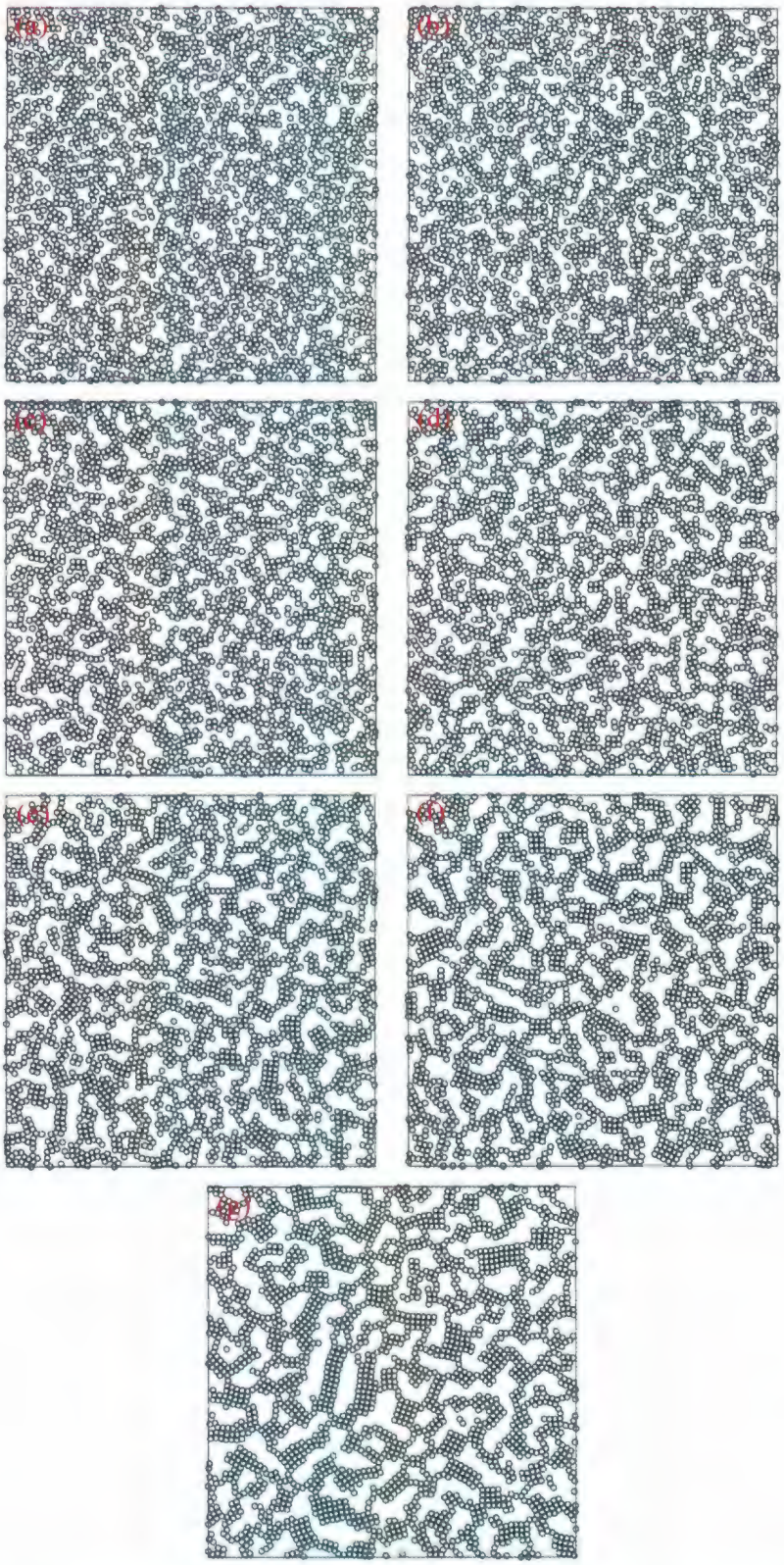

Figure 3.24: Stable configurations for an isochoric system of an area fraction that equals $A = 50\%$ and temperatures (a) T = 5.0, (b) T = 4.0, (c) T = 3.0, (d) T = 2.5, (e) T = 2.3, (f) T = 2.0 and (g) T = 1.8.

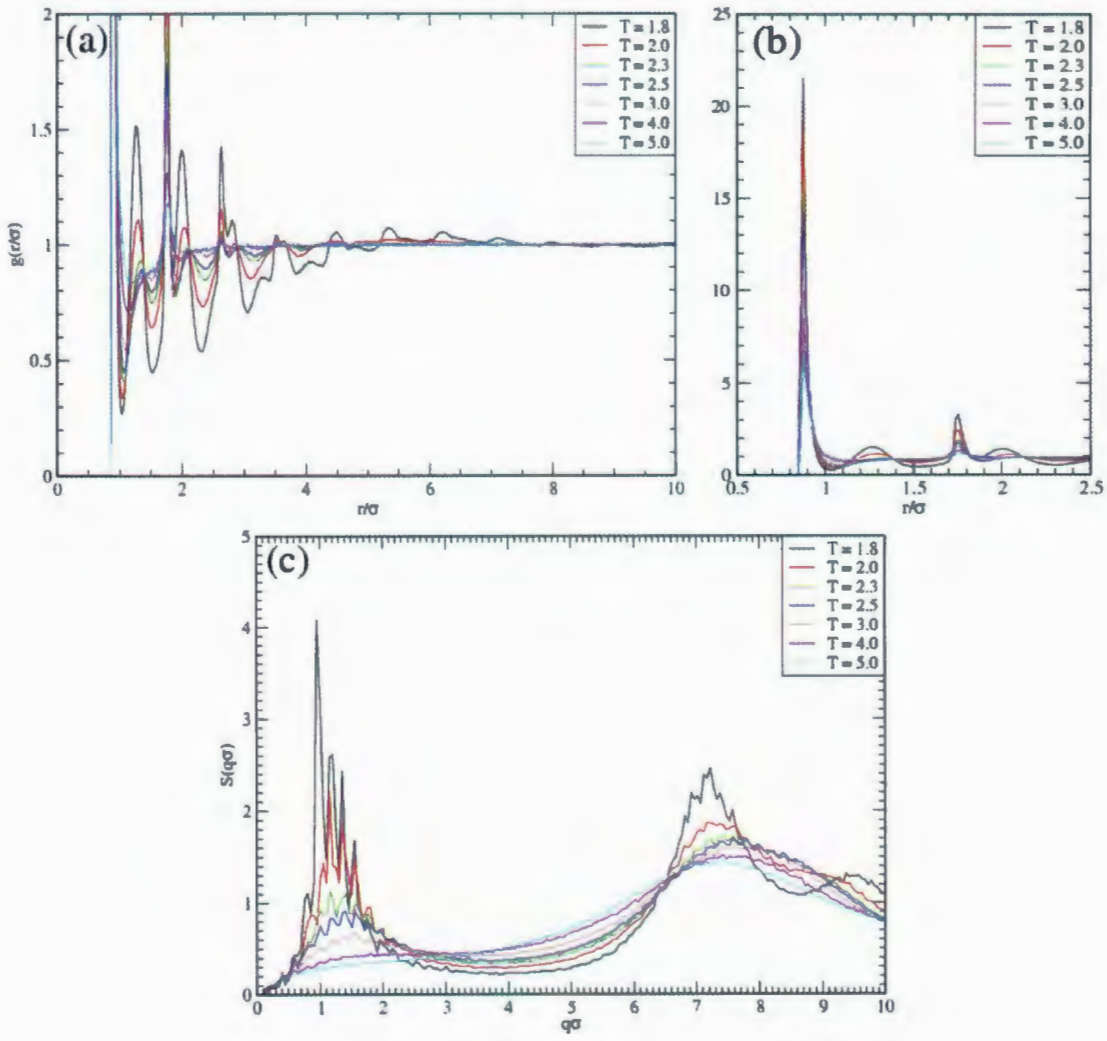

Figure 3.25: Fig. (a) shows $g(r)$ for an area fraction that equals $A = 50\%$, while Fig. (b) shows the height of the first few peaks. Fig. (c) shows the structure factor for the same area fraction.

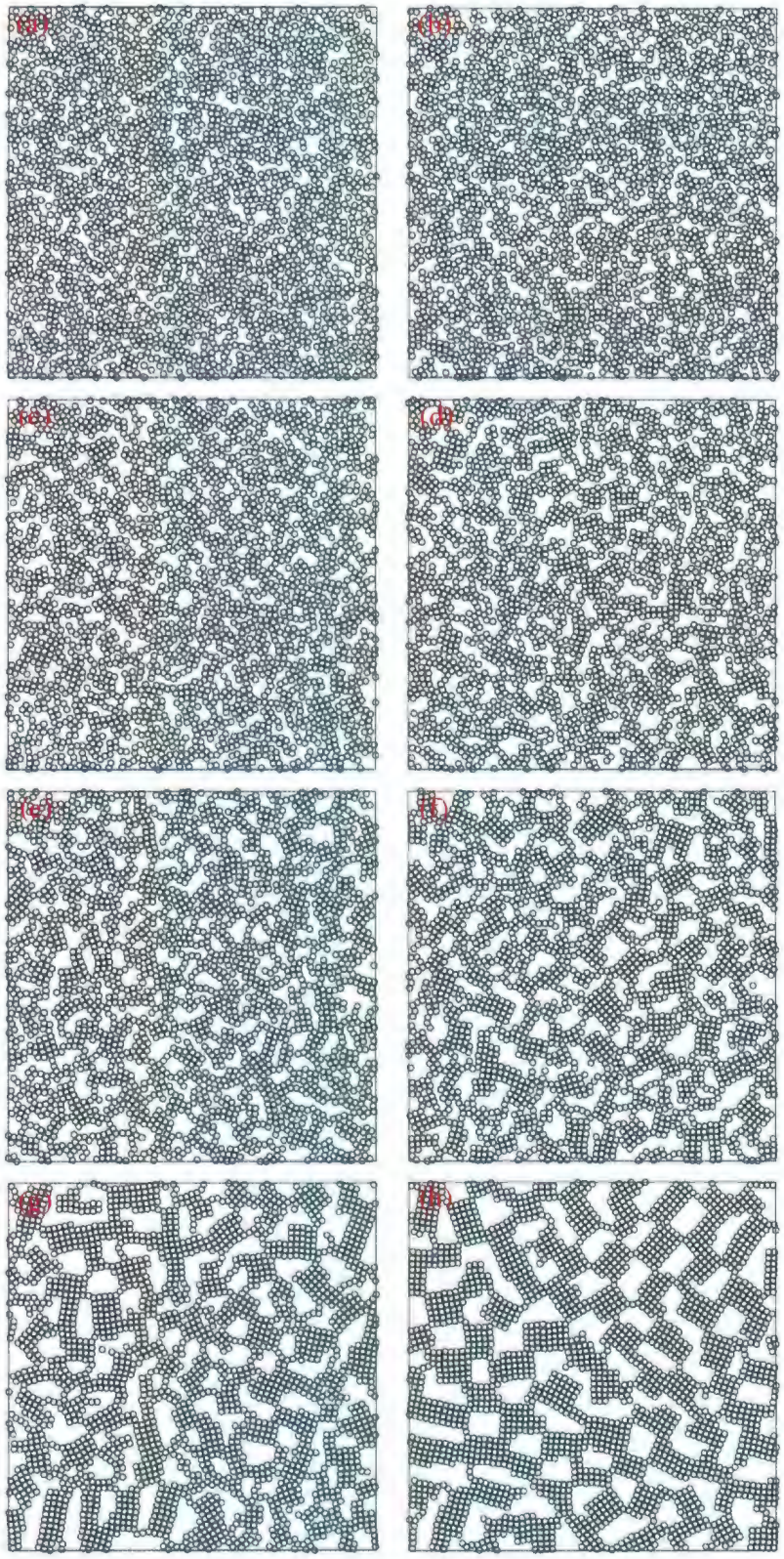

Figure 3.26: Stable configurations for an isochoric system of an area fraction that equals $A = 60\%$ and temperatures (a) T = 5.0, (b) T = 4.0, (c) T = 3.0, (d) T = 2.5, (e) T = 2.3, (f) T = 2.0, (g) T = 1.8 and (h) T = 1.6.

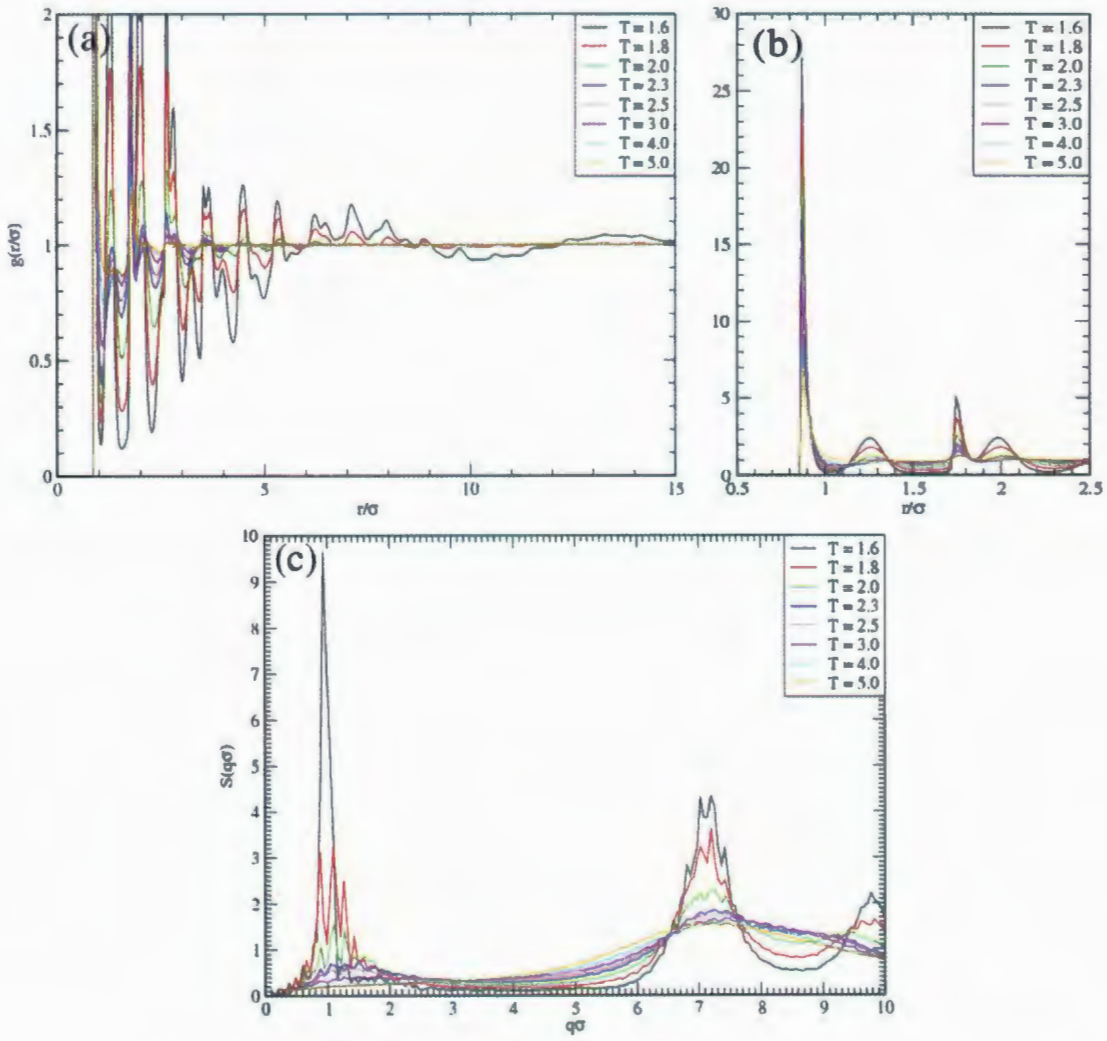

Figure 3.27: Fig. (a) shows $g(r)$ for an area fraction that equals $A = 60\%$, while Fig. (b) shows the height of the first few peaks. Fig. (c) shows the structure factor for the same area fraction.

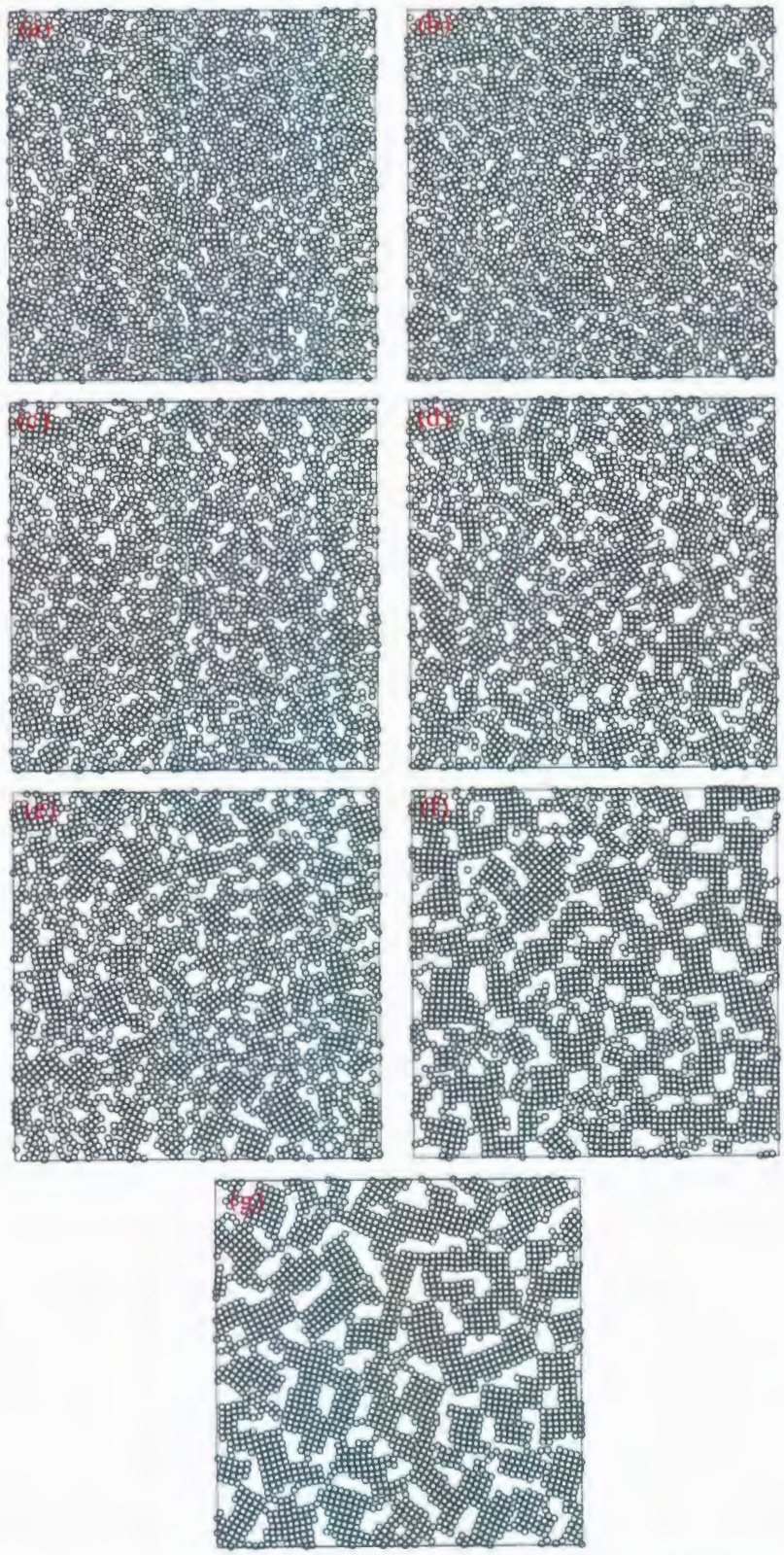

Figure 3.28: Stable configurations for an isochoric system of an area fraction that equals A = 70% and temperatures (a) T = 5.0, (b) T = 4.0, (c) T = 3.0, (d) T = 2.5, (e) T = 2.3, (f) T = 2.0 and (g) T = 1.8.

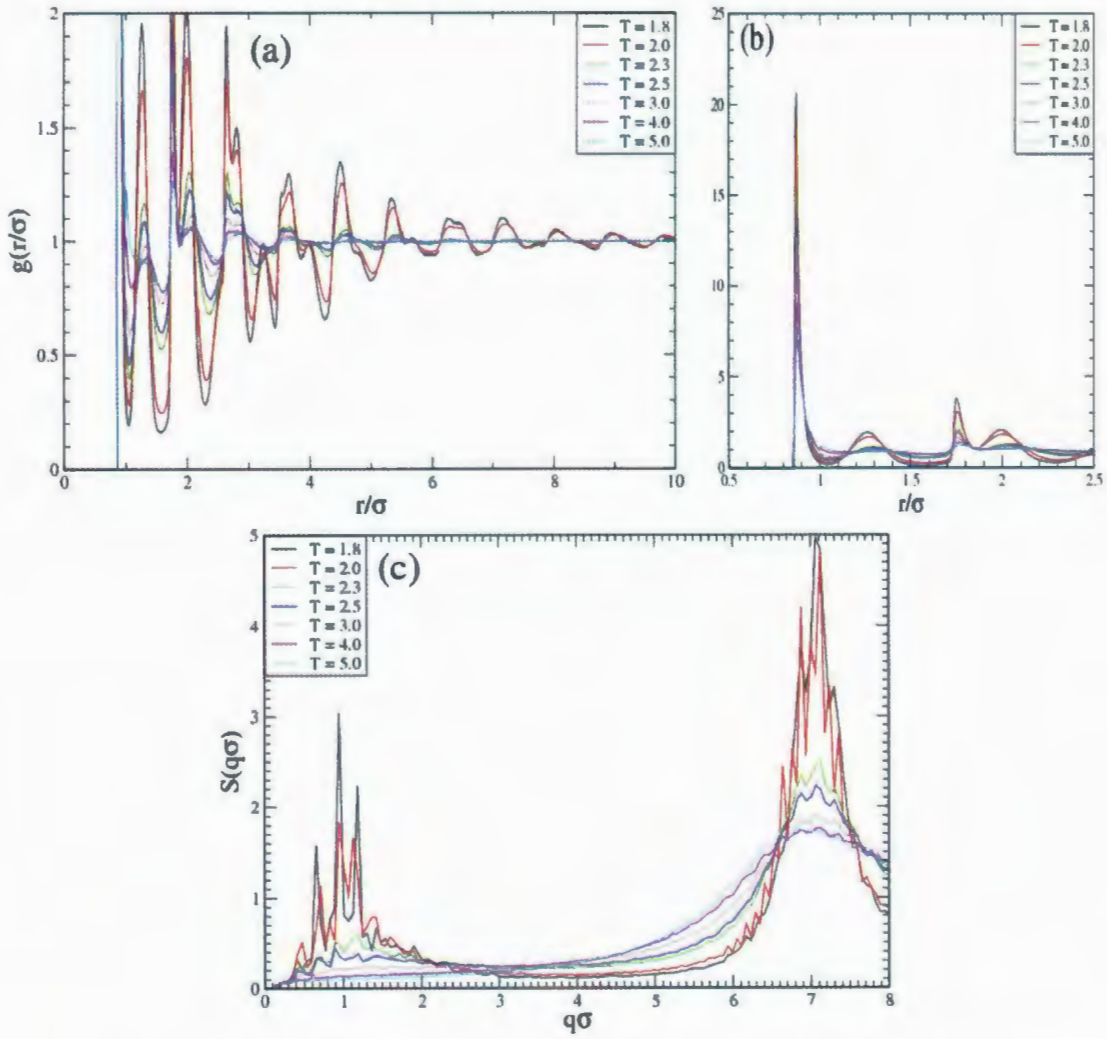

Figure 3.29: Fig. (a) shows $g(r)$ for an area fraction that equals $A = 70\%$, while Fig. (b) shows the height of the first few peaks. Fig. (c) shows the structure factor for the same area fraction.

Chapter 4

The Void Phase

In this chapter, we will introduce the void phase produced by two experimental groups, Kumar *et al.* and Agarwal *et al.*, at low volume fraction ($< 1\%$). After that, we will discuss some physical interactions that could be responsible for producing the void phase, such as dipolar interaction, Yukawa interaction, and van der Waals interaction. Then, we will introduce some "toy" mathematical potentials that we simulate in order to gain a qualitative understanding for the features of the potential that gives rise to the void phase. At the same time, we will present different results obtained from simulating each physical or mathematical potential.

4.1 The Experimental Void Phase

In 2005, Kumar *et al.* reported the discovery of a new phase, called the void phase, by applying an external electric field on a colloidal suspension at very low volume fraction ($< 1\%$), as shown in Fig. 4.1. At the beginning, the colloids interact with each other via dipole-dipole interaction to form anisotropic structure called dipolar rods. These dipolar rods are simply chains of colloids connected head-to-tail with each other along the external electric field direction.

At the same time, Kumar *et al.* assumed that all the other forces and potentials

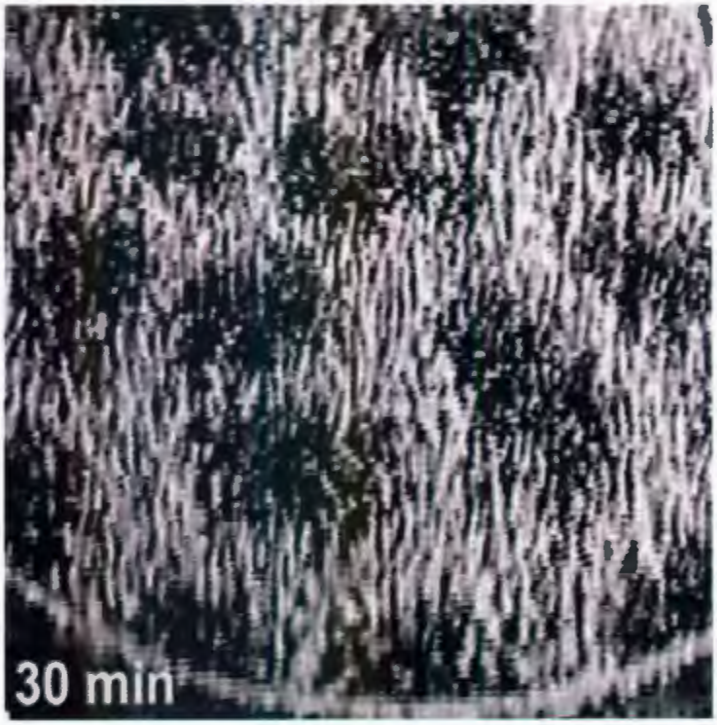

Figure 4.1: Formation of cellular patterns (or voids) in the plane perpendicular to the field direction as a result of pure dipolar interaction as Kumar *et al.* assumed in their work.

are suppressed in the system. This means that the dipole-dipole interaction is the only potential necessary to produce this phase. On the other hand, Agarwal *et al.* reproduced the void phase also at a very low volume fraction, as shown in Fig. 4.2. In contrast, they did not assume the absence of other forces and interactions in the system. Agarwal *et al.* expect that both repulsions (e.g. the Yukawa interaction) and attractions (arising from van der Waals interactions), in addition to the dipolar interaction, may play a role in producing the void phase, and not necessarily the dipolar interaction alone.

4.2 Simulating Physical Potentials

We perform MC simulation to model a 2D dipolar system of 2500 disks, where each disk represents a chain of 50 particles directed along the external electric field. As in Chapter 3, both stacked and staggered dipolar interactions are identified in the dipolar system.

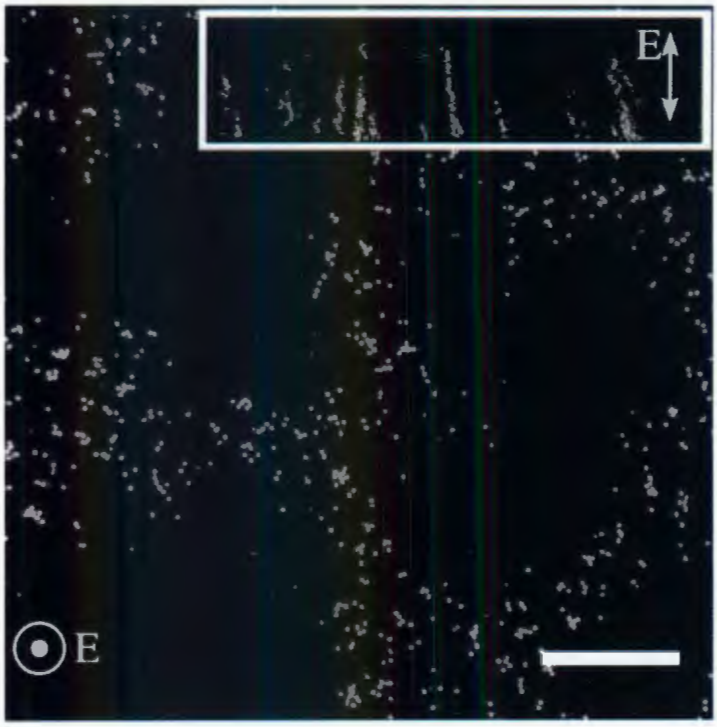

Figure 4.2: Formation of cellular patterns (or voids) in the plane perpendicular to the field direction. Agarwal *et al.* expect that all of dipolar interaction, Yukawa interaction, and van der Waals interaction could be behind the void phase.

We perform the first MC simulation at a volume fraction equal to 0.66% and using only the dipolar interaction, which is given in the following equation that is equivalent to the treatment of the dipolar interaction given previously,

$$\frac{U(r,\theta)}{k_B T} = \alpha \left(\frac{\sigma}{r}\right)^3 \left(1 - 3\cos^2\theta\right), \tag{4.1}$$

where α is called the dipolar strength, and $k_B T$ is called the thermal energy, we set σ to be equal to 1. The strength of the dipolar interaction is relative to the thermal energy. Many simulations were done using the dipole-dipole interaction controlled by α at different values of α, but we did not get the void phase using this potential at any value of α. Essentially, extending the results of Chapter 3 to a slightly lower area fraction, we obtain a homogeneous fluid at low α, and a continuously changing to a *bct* cluster gas

at high α. At this point, we confirm that using the dipolar interaction is not enough to produce the void phase, but is only responsible for forming clustered dipolar rods. Therefore, we added both of Yukawa ($U_Y(r)$) and van der Waals ($U_V(r)$) interactions to the dipolar interaction. Yukawa interaction, given in Eq. 4.2, is a repulsive potential and it arises in the dipolar system as a result of charged colloids. In contrast, van der Waals interaction, given in Eq. 4.3, is an attractive potential and it arises normally between all particles as a result of the electrons' motion around the nuclei.

$$\frac{U_Y(r)}{k_BT} = \epsilon\frac{\exp[-\kappa(r-\sigma)]}{r/\sigma}, \tag{4.2}$$

$$\frac{U_V(r)}{k_BT} = -\frac{\nu}{r^6}. \tag{4.3}$$

where ϵ is a constant prefactor that depends on the colloidal charge number Z, κ^{-1} is the Debye screening length, and it equals 16^{-1} as measured by Agarwal *et al.*, ν is a constant prefactor that depends on the colloids' density, radius, and material composition. Many simulations were done at different values of α, ϵ, and ν. The general results are not very different from using the pure dipolar interaction, where the resultant structures are either homogeneous, heterogeneous, or *bct* cluster gas, rather than void phase, similar to Fig. 3.14. Perhaps of interest is a set of simulations where we use a van der Waals-like attraction of $-\nu'/r^2$, i.e. a much longer range attraction. Although we can not motivate this form for the attraction on physical grounds, we do find that the system exhibits a void-like structure while it is equilibrating. At $\alpha = 10$, $\epsilon = 100$, and $\nu' = 0.015$, the total interaction potential presented in Fig. 4.3 creates unstable voids, as appears in Fig. 4.4. Unstable voids means that this phase can be seen at an earlier time of the simulation. After several thousand MC steps, the void phase evolves to a cluster phase. These intermittent voids bring up the possibility that the phase may arise as an arrested

non-equilibrium state.

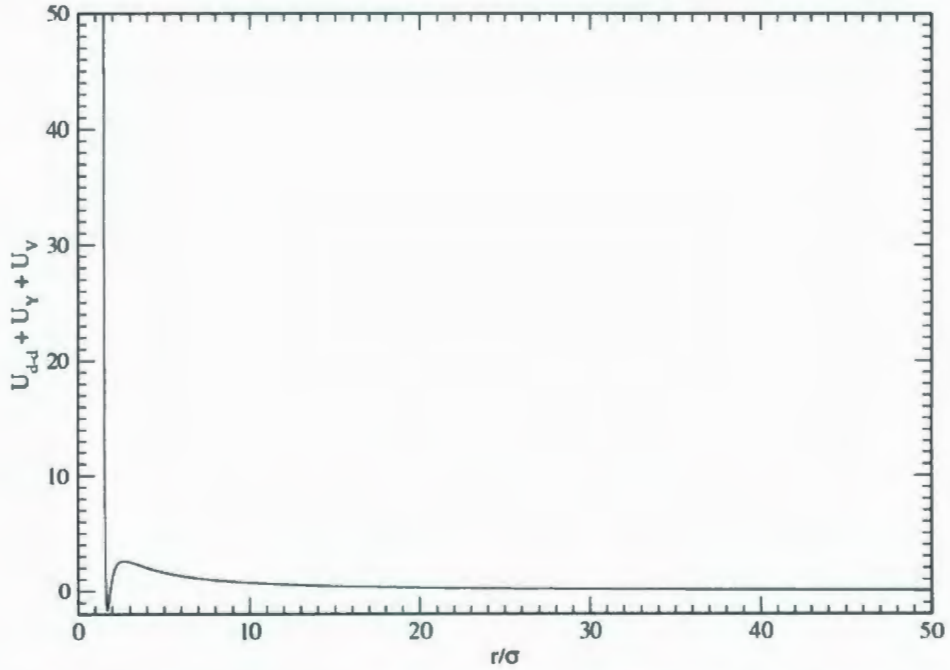

Figure 4.3: A total interacting potential includes three different potentials, dipolar, Yukawa, and van der Waals ($-\nu'/r^2$) interactions.

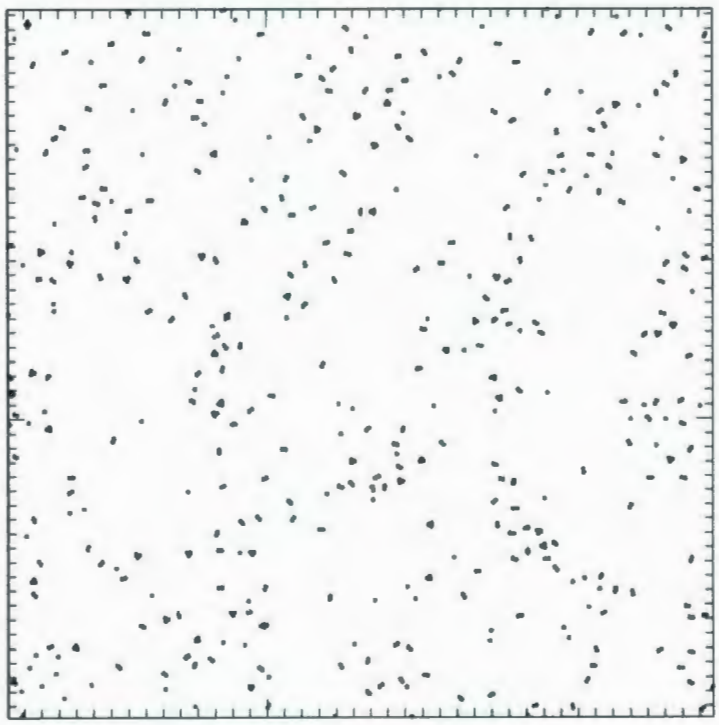

Figure 4.4: Unstable void phase obtained by simulating dipolar, Yukawa, and van der Waals ($-\nu'/r^2$) interactions together.

Having unsuccessfully searched for parameters that may yield a void phase, we make a departure from the physically realistic potentials and seek to gain a broader understanding of what may give rise to voids by utilizing toy potentials in the next section.

4.3 Simulating Mathematical Potentials

In the previous experimental results, the void can be described as a particle-free domain enclosed completely by particle-rich walls. Also, the walls are diffusive, where we can see some small clusters a few chains in size, and many separated chains. On the other hand, the wall's thickness is estimated to be about 10 σ, while the void size is about 50 σ to 70 σ, where σ is the colloid's diameter. Therefore, we expect that the void potential could have a short range attractive part that extends to few σ's in order to allow the forming of small clusters. Then, it is followed by a repulsive part that extends to a distance of about 10 σ or 15 σ in order to form walls of this size. The last part of the void potential is a weak repulsive part that extends to a distance of about 70 σ to make the walls this distance apart. Fig. 4.5(a) shows our prediction for the mathematical void potential,

We observe from Fig. 4.5(a) that there are five parameters that can change both the strength and the range of each part in the mathematical function. The parameters A, D, and E determine the strength of each part in the mathematical function, while B and C determine the range of the 1st and 2nd part in the mathematical function. The range of the last part is fixed and it equals 70 σ. The total number of simulations using this function was 243. Indeed, we did not get the void phase by using this mathematical function. Instead, we got a stable diffusive cluster phase for all simulations as presented in Fig. 4.5(b). These clusters are arranged periodically in the space, and this result is not reported in any previous work. Interestingly, the characteristic size of these clusters

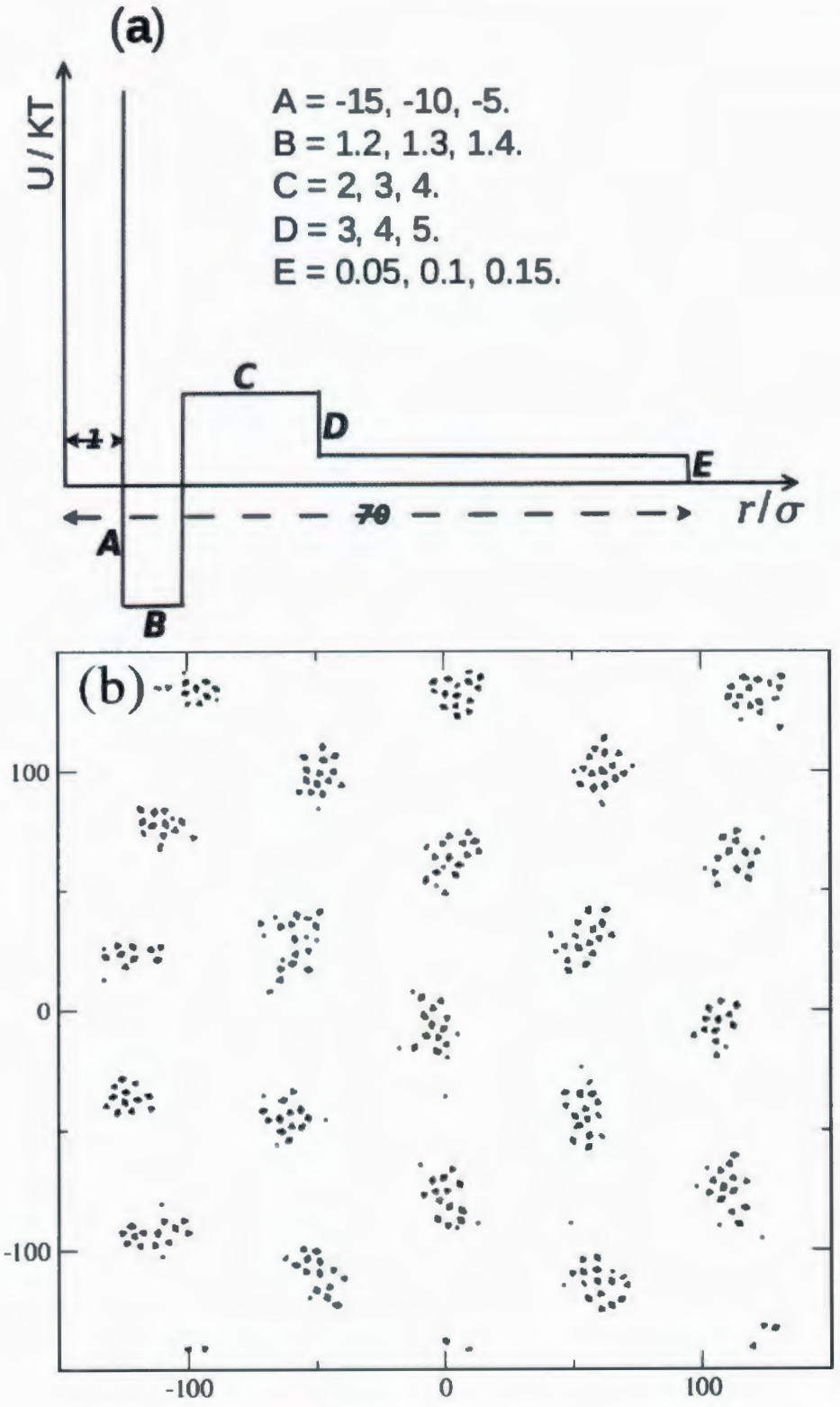

Figure 4.5: Fig. (a) is the first mathematical function that estimated for the void potential. It includes a strong attractive part at short distances, and a weak repulsive part at long distances. A relatively strong repulsive part is located in between the two parts. While Fig. (b) is the diffusive cluster phase obtained as a result of simulating the first mathematical function presented in Fig. (a).

scales with the strong middle range repulsion, while the spacing between the clusters scales with the weak long range repulsion.

We observe from Fig. 4.5(b) that there are small clusters produced as a result of the attractive part of the mathematical function at short distances. The average distance between the clusters is about 70 σ, which is produced as a result of the weak repulsive part. The average size of the cluster is about 10 σ, which is produced as a result of the relatively strong repulsive part.

At this point, we become very sure that the void phase can be obtained as a result of a repulsive potential, while the attractive potential has only a role in forming small compact clusters inside the walls. Therefore, we create a new mathematical function of only a repulsive interaction as shown in Fig. 4.6

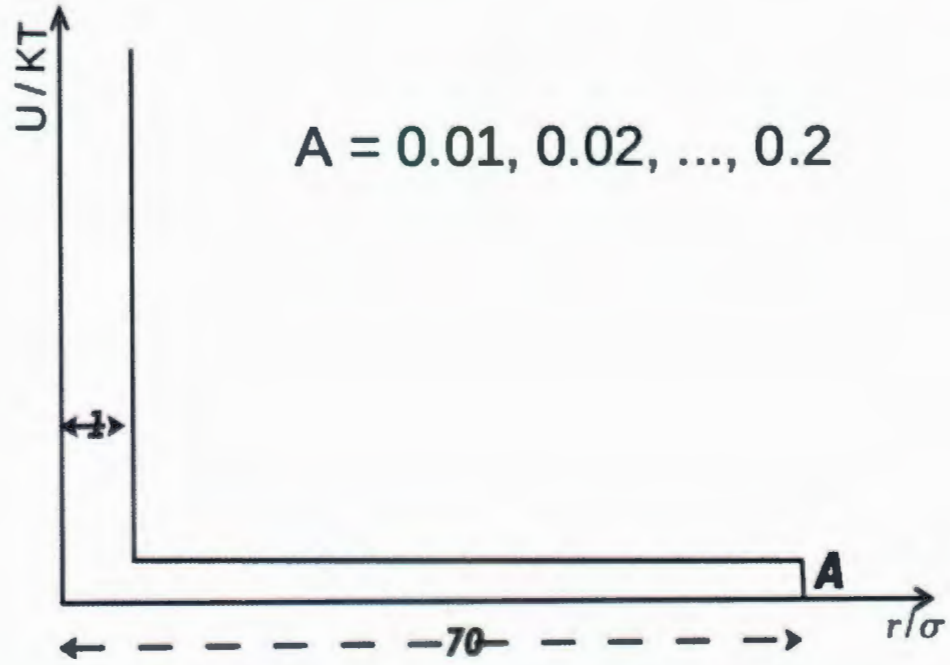

Figure 4.6: The second mathematical function that estimated for the void potential. It includes only a repulsive part that extends from 1 σ to 70 σ.

In this mathematical function, the repulsive interaction extends from $r = 1\ \sigma$ to

$r = 70\ \sigma$. The parameter A changes from 0.01 to 0.2, and it controls the strength of the repulsive interaction. Also using this mathematical function, we do not get the void phase, but rather a fluid for $A \leq 0.05$, as in Fig. 4.7(a), and for $A \geq 0.06$ a diffusive cluster phase, with clouds of particles separated by a distance about 70 σ, as in Fig. 4.7(b). The formation of loose clusters in the absence of attraction is interesting. The mechanism for its arising can be explained by considering that the system consists of soft disks of diameter 70 that can overlap if sufficiently compressed. In Fig. 4.7(b) we see that it only takes about 10 such disks to occupy most of the available space. Any disk added to the system can lower the number of overlaps it creates by locating itself very near to a disk, overlapping with that disk only. Thus, the clustering in Fig. 4.7(b) results from the system reducing overlaps, and not from any attraction.

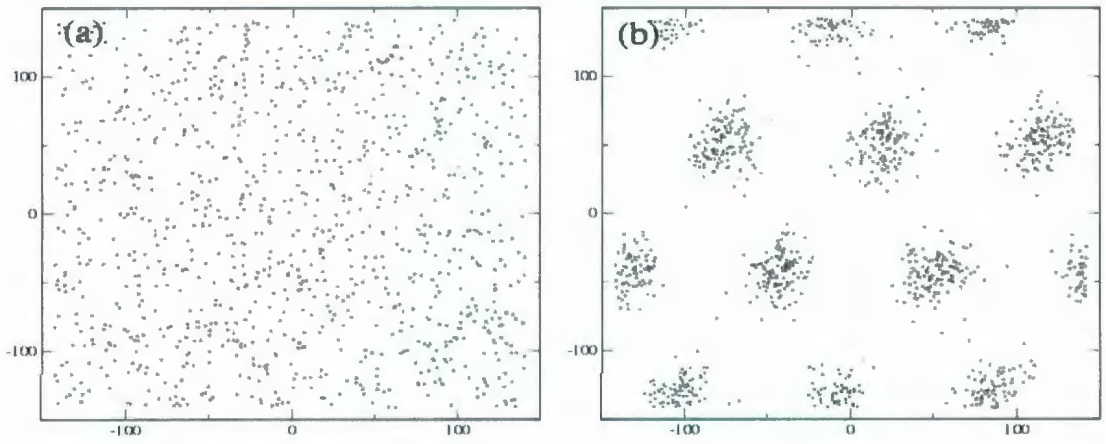

Figure 4.7: Fig. (a) is the configuration obtained by using the mathematical function shown in Fig. 4.6 at ($A \leq 0.05$), while Fig. (b) is the configuration obtained at ($A \geq 0.06$).

The third mathematical function that we simulate includes two repulsive parts, as shown in Fig. 4.8(a). The first part is a strong short range that varies from $r = 1\ \sigma$ to $r = A\ \sigma$, where $A = 3,\ 6,\ 9,\ 12$, or 15, while the second part is a weak long range that varies from $r = A\ \sigma$ to $r = 70\ \sigma$. The strength of the first part also is varied from $B = 1$

to $B = 5$, while the strength of the second part is varied from $C = 0.1$ to $C = 0.5$.

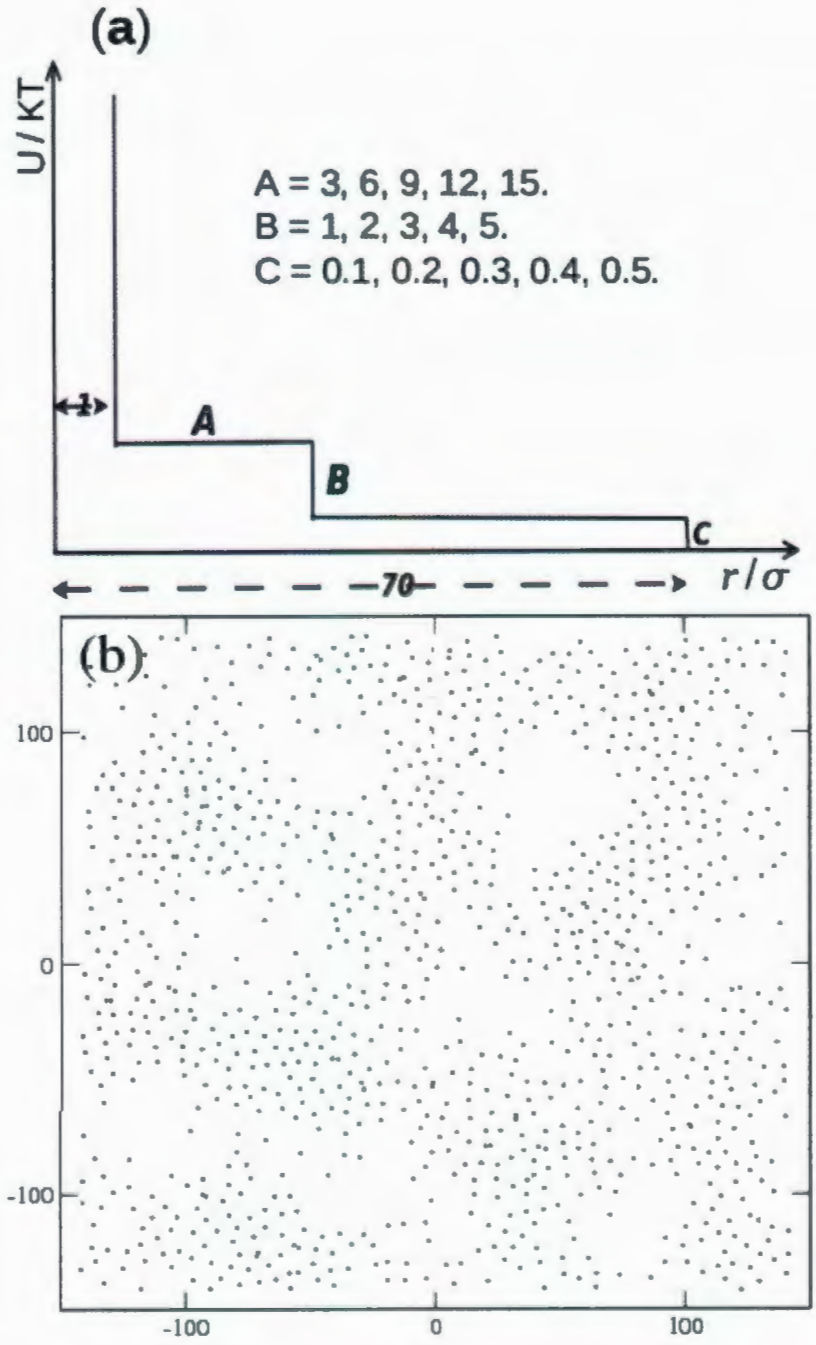

Figure 4.8: Fig. (a) is the third mathematical function of two repulsive parts that estimated for the void potential. The first part extends from $r = 1\ \sigma$ to $r = A\ \sigma$, while the second part extends from $r = A\ \sigma$ to $r = 70\ \sigma$. Fig. (b) is the void phase obtained by simulating the mathematical function, presented in Fig. (a), at $A = 6$, $B = 5$, and $C = 0.2$.

The rational for introducing an additional shorter range repulsion is that we wish to

somehow spread out the particles within the clustered area in Fig. 4.7(b), affording the clouds the opportunity to contact and thus form diffusive walls as seen in experiment. Simulating the third mathematical function gives different kinds of structures at different values of A, B, and C. The most interesting result was at $A = 6$, $B = 5$, and $C = 0.2$, where we see a stable void phase. This is presented in Fig. 4.8(b). From this figure, we can observe voids of diameter about 50 σ, which is very close to the results reported by Kumar *et al.* and Agarwal *et al.*. The only difference is that the wall thickness in our simulation is about 40 σ to 50 σ, which is much bigger than the results obtained experimentally.

Subsequently, we add a very weak attractive potential at a short distance into the third mathematical function, as shown in Fig. 4.9, in an attempt to compress the walls. Unfortunately, we do not get good results, instead we lose the void phase at all values of the new parameters D and E, and the system reverts to being either homogeneous or comprised of compact clusters.

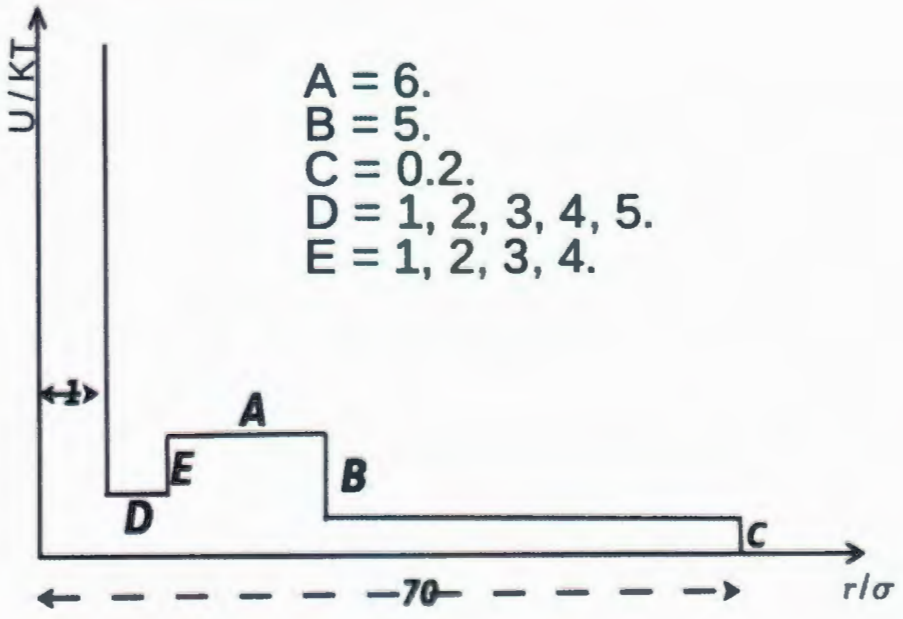

Figure 4.9: An improved shape for the third mathematical function after adding a weak attractive potential at a short distance.

The fourth mathematical function that we simulate also includes two repulsive parts, as shown in Fig. 4.10(a). The first part extends from $r = 1\ \sigma$ to $r = A\ \sigma$, where A changes from 1 to 10. The second part decays linearly from $r = A\ \sigma$ to reach *zero* at $r = 70\ \sigma$. The strength of the first part changes from $B = 0.4$ to $B = 1.0$. We expect that the first repulsion will form walls of thickness $A\ \sigma$, while the second repulsion will make the walls about 70 σ apart.

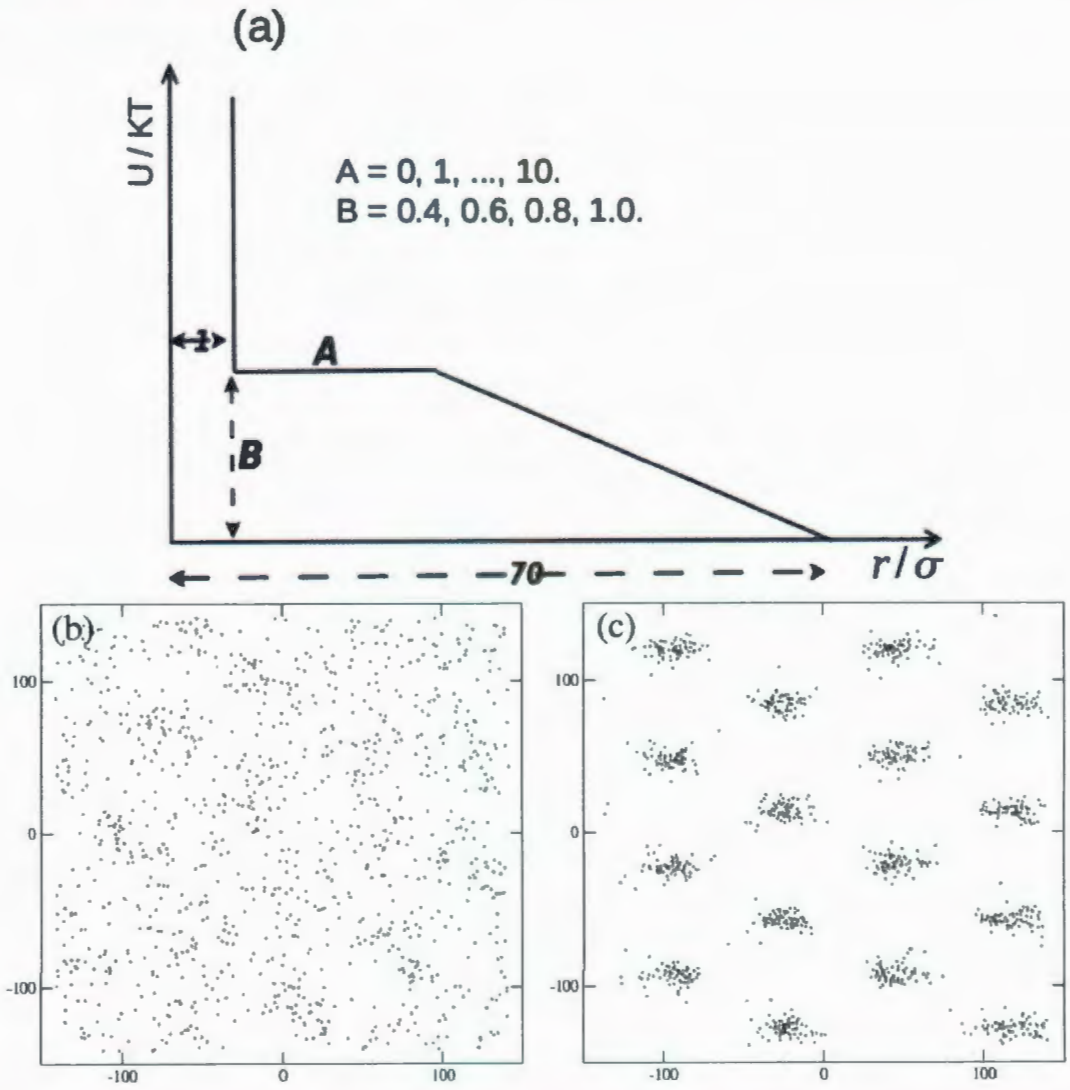

Figure 4.10: Fig. (a) is the fourth mathematical function of two repulsive parts that estimated for the void potential. The first part extends from $r = 1\ \sigma$ to $r = A\ \sigma$, while the second part decays linearly from $r = A\ \sigma$ to reach *zero* at $r = 70\ \sigma$. Fig. (b) is the configuration obtained by using the fourth mathematical function at ($B \leq 0.6$), while Fig. (c) is the configuration obtained at ($B \geq 0.8$).

In fact, the results are not what we expect. We found that the parameter A does not play a significant role in the resultant structure, while the parameter B is the important one. The resultant structures using the fourth mathematical function can be divided into two main categories. The first one is a heterogeneous structure obtained at any of the values chosen for A and $B \leq 0.6$, as we see in Fig. 4.10(b), whereas the second one is a diffusive cluster phase obtained at any of the values chosen for A and $B \geq 0.8$, as we see in Fig. 4.10(c). A qualitatively, new feature is the anisotropy of the shape of the diffusive clusters.

The fifth mathematical function is very similar to the previous one, but we replace the linearly decaying part by $1/r$ decaying part, as shown in Fig. 4.11

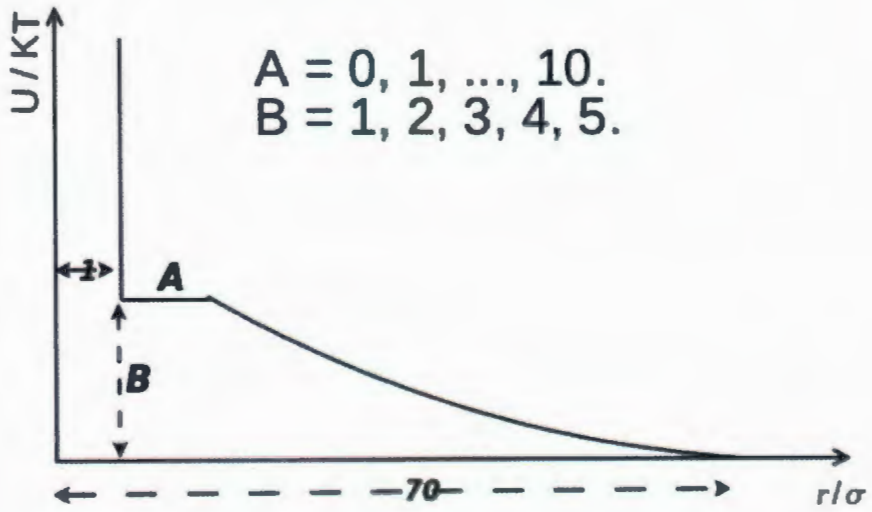

Figure 4.11: The fifth mathematical function of two repulsive parts estimated for the void potential. The first part extends from $r = 1\ \sigma$ to $r = A\ \sigma$, while the second one is decaying as $1/r$ from $r = A\ \sigma$ to reach *zero* at $r = 70\ \sigma$.

Here also, we did not get the void phase. Instead, the resultant structures can be divided into three main groups. The first one is obtained at low values of A, where the structure is a homogeneous fluid, as we see in Fig. 4.12(a). The second one is obtained at high values of A and low values of B, where the structure is a heterogeneous fluid, as

we see in Fig. 4.12(b). Finally, the third one is obtained at high values of A and high values of B, where the structure is a homogeneous diffusive cluster crystal, as we see in Fig. 4.12(c).

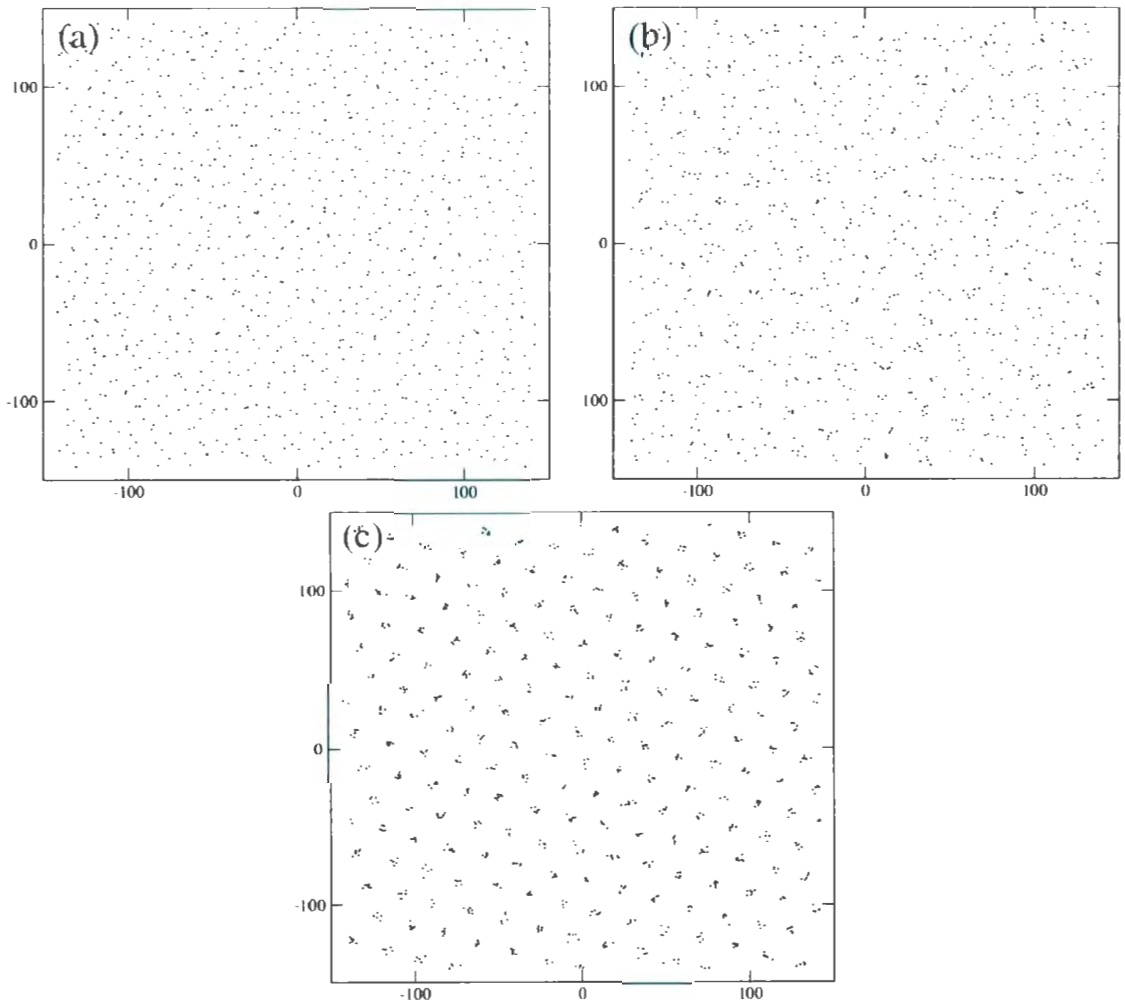

Figure 4.12: Fig. (a) is the configuration obtained by using the fifth mathematical function, shown in Fig. 4.11, at $A = 4$ and $B = 3$. Fig. (b) is the configuration obtained at $A = 10$ and $B = 2$. Finally, Fig. (c) is the configuration obtained at $A = 10$ and $B = 5$.

Chapter 5

Discussion, Conclusions and Future Work

An electrorheological fluid is a suspension of non-conducting particles of few micrometers size in an electrically insulating fluid and responds to an external electric field. The electric field induces dipole moments in the colloids that align parallel to the field if $\epsilon_p > \epsilon_s$, or anti-parallel to the field if $\epsilon_p < \epsilon_s$. In either case, the particles interact with each other through a dipole-dipole interaction for which dipole moments are the same. In the presence of a strong external electric field, the colloids will attract and repel each other in such a way as to form long chains along the external electric field direction. Experimentally, when the external electric field is sufficiently large, the system becomes one composed of such chains.

However, a cumulative interaction arise between the chains as a summation of all dipole-dipole interactions between all particles in each two chains. This resultant chain-chain dipolar interaction can be divided into two main types. First, the stacked interaction arises when the particles of any chains encounter the particles in another chain "face to face". This interaction has a feature of a strong short range repulsion and a weak long range repulsion (see Figs. 2.3 and 2.5). The second interaction is the staggered case that arises when the particles in the second chain are shifted a distance of $\sigma/2$ in the $z-$direction and it has a feature of strong short range attraction and weak long range

repulsion (see Figs. 2.6 and 2.8). The competing attractive and repulsive interactions lead to finite clustering, an effect that has importance in other colloidal systems.

This thesis deals mainly with using Monte Carlo simulation to understand a dipolar system under the influence of an external electric field. In this regime, the system effectively becomes two dimensional when viewed down the field axis, and the chains appear as disks in a plane. These disks tend to attract at short distances and repel at larger distances, leading to the formation of finite clusters of square symmetry packing. The first goal in this thesis is studying the structural properties of the 2D fluid across a wide range of area fraction and temperature. The second goal is to determine whether the dipolar interaction can produce the void phase at low volume fraction, or whether additional interactions are required. On the other hand, several classes of toy mathematical potentials are simulated at low volume fraction to gain a better understanding of what may drive the formation of the void phase.

5.0.1 Phase Diagram

With regards to the phase behaviour of the system, Ref. [8] reports that most of the fluid region (low to middle values of packing fraction) at high fields (low T) is occupied by phase coexistence between the bct crystal and a very low density fluid or gas, as shown in Fig. 3.10. However, unlike typical bulk phase coexistence, the solid phase is not contiguous, but rather broken up into clusters.

A difficulty in this picture is revealed when we consider the interaction between chains, and see that the short range attraction and long range repulsion lead directly to clustering. Even if all the disks representing the chains were locally crystalline, the sample as a whole would be inhomogeneous, with crystallites repelling one another and tending not to form a single body.

In more concrete terms, in a region of phase coexistence the equilibrium pressure is a constant, i.e. the pressure along an isotherm does not change with packing fraction. We clearly see that the pressure increases with increasing packing fraction, presumably because of the cluster-cluster repulsion (see Fig. 3.9). Therefore, we disagree with the picture of phase coexistence.

Additionally, the change-over from the high T fluid at 1% area fraction to a gas of clusters of mostly size four, is well described by a simple two-state model (see Fig. 3.8). No recourse to a phase transition is required. We do not have sufficient low T data to examine this scenario at higher packing fractions, but in principle the two-state model may not do a good job as clusters interact more strongly. We see at 1% that the two-state model does not capture the harmonic solid behaviour of clusters.

On the other hand, the free energy of cluster formation does seem to indicate some first order character to clustering. Already at area fraction 30%, we see a separate minimum developing in $\Delta F(n)$ at $n > 1$, indicating a free energy barrier between small, fluid-like clusters and larger ones. At lower packing fraction, the free energy curves seem to make a continuous change from having a minimum at zero cluster size to having a minimum at finite cluster size.

Thus, there appears to be some difficulty in describing phase coexistence in clustering systems in terms of the usual framework of, say, bulk phase separation between gas and crystal at constant volume.

In the literature for colloidal systems that exhibit clustering, there exists a simpler framework in which the fluid is carved into three regions: a percolated fluid, a cluster fluid, and a simpler fluid, as shown in Fig. 3.11. The cluster fluid is defined as one having a local minimum in $\Delta F(n)$ at $n > 1$, but not having a percolating cluster. Any

formal phase coexistence between the fluid and the eventual crystal phase at high packing fraction would occur in the percolated region, where it is perhaps less difficult to think of coexistence as occurring in the usual sense.

We present our results within this second framework. Our pressures do show either an inflection (implying a compressibility maximum) or a discontinuous change in slope near the percolation line, where the presence of a spanning cluster has an impact on the properties of the system, and so this framework does have practical, physical meaning (see Fig. 3.9). If we stretch the interpretation of the kink in the pressure to be the flat region expected during phase coexistence, then we can at least conclude that the region of coexistence occurs at significantly higher packing fraction than that suggested by Ref. [8].

We do acknowledge that using the pressure to directly test for coexistence is somewhat problematic in that the system is finite in size and obtaining true equilibrium may be challenging in simulation. Finite size systems tend to smooth out any apparent transition, and the interfacial energy between two phases may be non-negligible. However, the system seems to quite easily form crystallites, and obtaining equilibrium between clusters and a rare fluid should not be a problem, i.e. it should be fairly easy for the cluster fluid to equilibrate. Where the problem may likely occur is at higher area fractions, where we see something more like crystallites coexisting with a dense fluid. In this case, fully equilibrating the system might result in bulk phase separation between clustered crystallites and a clustered fluid, see e.g. Fig. 3.28(f).

Therefore, we conclude that at least the portion of the phase diagram covered by our cluster fluid, the system is not described by bulk phase coexistence in the usual sense.

5.0.2 Void Phase

It is quite apparent that chains of dipolar hard spheres do not yield a void phase. Adding van der Waals or Yukawa interactions can change the bonding energy relative to the repulsive barrier and change to some degree the location of the peak of the repulsive barrier. However, nothing in our systematic varying of parameters yields the void phase.

Using simpler toy potentials, we can partially recover the void phase. Loose clustering of particles can be achieved with repulsions only. An additional repulsion at short range causes the particles within loose clusters to be further from each other. An appropriate balance between these two repulsions gives a void phase (see Fig. 4.8(b)).

If indeed the experimentally seen void phase does arise in part from some additional intermediate range repulsion, it is difficult to see what could be physically causing it. Perhaps dielectric forces may play a role, e.g. the liquid may be attracted to the regions occupied by colloids because of the difference in the electric field caused by the presence of the colloids, but this is speculation.

We also note the possibility of the void phase arising from non-equilibrium effects. Initial void structures driven by, say, some non-equilibrium hydrodynamic effect may become kinetically trapped. Whatever the cause, it must not play a significant role at higher packing fractions because there simple dipolar chains do reproduce, at least qualitatively, the structures seen experimentally.

5.0.3 Future Work

The low T behaviour of the model is of interest. The anomalous pressure behaviour near percolation, as well as the expected heat capacity peaks will help sort out questions about the nature of the cluster fluid and whether there is coexistence between the crystal and the dense fluid.

To study low temperatures, it would be worthwhile to implement some MC scheme that incorporates trial moves other than just small, single particle displacement. The hope is to reduce or avoid the time required for particles to break free of their bonds in order to explore configuration space.

Since the repulsion decays as $1/r^3$ for large r, i.e. slowly, it would be prudent implement a specialized technique, such as Ewald sums, to more accurately determining the energy - at least as a check to make sure we are not artificially suppressing qualitative changes in phase behaviour.

With regards to the void phase, a finer study of the toy potentials that do recover something close to the void phase is worthwhile. Determining the relationship between potential parameters and features of the structures seen, or even when transitions take place, would help in elucidating properties of the ingredients that will produce the void phase and that are missing from the current model.

We also need to explore ideas behind additional forces in the systems, like dielectrophoresis, or possible non-equilibrium effects that may be important to the formation of voids.

To confirm the presence or lack of a first order transition, we also wish to study the system in a constant pressure ensemble. If free energy barriers to transformation are low, as they appear to be here, we should see any phase transition occur with very little hysteresis.

Bibliography

[1] D. Fennell Evans and Hakan Wennerstrom, *The Colloidal Domain Where Physics, Chemistry, Biology, and Technology Meet.* (VCH 1994).

[2] W. B. Russel, D. A. Saville and W. R. Schowalter, *Colloidal Dispersions*, Cambridge University Press, 1989.

[3] Robert J. Hunter, *Introduction to Modern Colloid Science.* Oxford Science Publications, 1993.

[4] Richard A. L. Jones, *Soft Condensed Matter.* Oxford University Press, 2007.

[5] H. A. Barnes, J. F. Hutton and K. Walters, *An Introduction to Rheology.* Elsevier Science Publishers, 1989.

[6] Jacob N. Israelachvili, *Intermolecular and Surface Forces: With Applications to Colloidal and Biological Systems.* Academic Press, 1985.

[7] Anand Yethiraj and Alfons Blaaderen, Nature (London) **421**, 513 (2003).

[8] A. Hynninen and M. Dijkstra, Phys. Rev. E **72**, 051402 (2005).

[9] Daan Frenkel and Berend Smit, *Understanding Molecular Simulation: From algorithms to Applications.*San Diego, Academic Press, 1996.

[10] M. P. Allen and D. J. Tildesely, *Computer Simulation of Liquids.* Oxford Science Publications, 1987.

[11] A. Qing, *Differential Evolution: Fundamentals and Applications in Electrical Engineering.* Wiley, 2009.

[12] R. Tao, J. T. Woestman, and N. K. Jaggi, Appl. Phys. Lett. **55**, 1844 (1989).

[13] T. C. Halsey and W. Toor, Phys. Rev. Lett. **65**, 2820 (1990).

[14] T. J. Klingenberg, F. van Swol, and C. F. Zukoski, J. Chem. Phys. **91**, 7888 (1989).

[15] R. Tao and J. M. Sun, Phys. Rev. Lett. **67**, 398 (1991).

[16] Tian Hao, *Electrorheological Fluid: The Non-aqueous Suspensions.* Elsevier, 2005.

[17] J. E. Stangroom, Phys. Technol. **14**, 290 (1983).

[18] A. van Blaaderen, MRS Bull. **23**, 39 (1998).

[19] W. Wen, N. Wang, H. Ma, Z. Lin. W. Tam, C. Chan, and P. Sheng, Phys. Rev. Lett. **82**, 4248 (1999).

[20] Anand Yethiraj, H. J. Thijssen, Alan Wouterse and Alfons Blaaderen, Adv. Mater. (Weinheim, Ger) **16**, 596 (2004).

[21] A. Kumar, B. Khusid, Z. Qiu, and A. Acrivos, Phys. Rev. Lett. **95**, 258301 (2005).

[22] Amit K. Agarwal and Anand Yethiraj, Phys. Rev. Lett. **102**, 198301 (2009).

[23] R. Tao and J. Sun, Phys. Rev. A **44**, R6181-R6184 (1991).

[24] R. Tao, Phys. Rev. E **47**, 423-426 (1992).

[25] James E. Martin, Robert A. Anderson, and Chris P. Tigges, J. of Chem. Phys, **110**, 4854, (1998).

[26] James E. Martin, Robert A. Anderson, and Chris P. Tigges, J. Chem. Phys, **108**, 3765, (1997).

[27] A. Yethiraj and A. Van Blaaderen, Int. J. Mod. Phys, **16**, 2328 (2002).

[28] David J. Griffiths, *Introduction to Electrodynamics*. (VCH 1994).

[29] J. Jackson, "Classical Electrodynamics", (Wiley, New York, 1998).

[30] J. P. Hansen and I. R. Mcdonald, *Theory of Simple Liquids*. (Academic Press, 2006)

[31] N. Ashcroft and N. Mermin, *Solid State Physics*, 1976.

[32] F. Sciortino, P. Tartaglia, and E. Zaccarelli, J. Phys. Chem. B, **109**, 21942-21953, (2005).

[33] J. C. Toledano, F. Sciortino and E. Zaccarelli Soft Matter, **5**, 2390-2398, (2009).

[34] R. K. Pathria, *Statistical Mechanics*, Second Edition, 1972.

Appendix A

Verlet List

In computer simulation work, most of the time is consumed in calculating the distances between the particles and the interaction potential in the case of Monte Carlo simulation (MC) or the force calculation in the case of Molecular Dynamic simulation (MD). For simulation work with pairwise additive interactions, we calculate the distances between each particle and all other particles in the system. Assuming that the system contains N particles, this means that we need to compute $N(N-1)/2$ pair distances in addition to the same number of interaction calculations if the interaction is not truncated. Even if the system is truncated, we still need to calculate $N(N-1)/2$ pair distances. As a summary, the time needed for any MC or MD simulations scales as N^2 regardless if the system is truncated or not [9, 10].

In fact, there is an efficient technique in terms of short-range interaction in order to speed up the calculation of interactions and to save the CPU time. In this technique, the potential cutoff sphere of radius r_c for each particle on the system is surrounded by another sphere of radius r_v. At the beginning of the simulation, all of the particles that are confined inside the outer sphere are listed in an array to be the neighboring list or the "Verlet list" for the central molecule. In this case, each particle in the system has its own list. The time needed to construct the Verlet list for each particle scales as N^2, and obviously no time was saved until this stage. In the subsequent stages, the distances

between those particles in the list with the central particle are just taken into account. All other interactions with those particles out of the list are excluded because they do not contribute in the energy or force calculations. This last operation scales as N, and the same lists would still be considered for a large number of steps. As soon as one of the particles displaced more than $(r_v - r_c)/2$, the list must be updated. Updating the list scales again as N^2, and another bunch of steps will be considered again using the updated list, which scales as N.

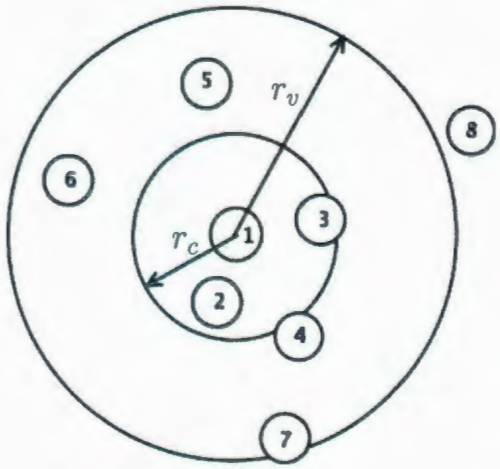

Figure A.1: Illustration of Verlet list and cutoff potential sphere. Verlet list contains all the particles inside the outer sphere. Just particles inside the inner sphere contribute in the interaction calculations.

Although all particles confined inside the outer sphere are considered to the neighboring list, those particles inside the inner sphere just contribute in the interaction calculations. One point must be considered that the layer between the two spheres should be thick enough in order to guarantee that no particle can penetrate through the layer to enter inside the inner sphere before updating the list. In more details, Particles 2, 3, 4, 5, 6 and 7 in Fig. (A.1) are on the list of particle 1. However, just particles 2 and 3 will contribute in the interaction calculations because they are inside the cutoff potential sphere. As the time goes on, particles 4, 5, 6 and 7 have a chance to enter inside the inner

sphere before updating the list and to share the interaction calculations. On the other hand, particle 8 is outside the list and it absolutely has no chance to join the interaction calculations with particle 1 before updating the list. In fact, particle 8 could enter inside the outer sphere before updating the list, but it can not enter inside the inner sphere. This is due to the fact that the layer is thick enough to make sure that list will be updated before penetrating the particle 8 through this layer.

As a conclusion, the time needed to finish the simulation work scales as N^2. While, the time needed for the simulation work using the Verlet list scales as N for most stages of the work except updating the list which scales as N^2. Optimizing both of r_c and r_v will make the computing time scales as $N^{3/2}$ or $N^{5/3}$, rather than N^2.

Appendix B

2-State Model

Consider a system with two energy states. The first state has an energy E_1 and degeneracy Ω_1, while the second state has an energy and degeneracy E_2 and Ω_2, respectively. The partition function (Q_1) for one disk is,

$$\begin{aligned} Q_1 = \Omega_i \sum_{i=1}^{n=2} \exp\left(-\beta E_i\right) &= \Omega_1 \exp\left(-\beta E_1\right) + \Omega_2 \exp\left(-\beta E_2\right) \\ &= \Omega_1 \exp\left(-\beta E_1\right)\left[1 + \Omega \exp\left(-\beta\ \Delta E\right)\right] \end{aligned} \tag{B.1}$$

where $\Omega = \Omega_2/\Omega_1$, and $\Delta E = (E_2 - E_1)$. The disks in the dipolar system are considered distinguishable particles because the position of each disk can be determined with infinite precision. As a result, the partition function for N-disks can be expressed as,

$$Q_N = Q_1^N = \left(\Omega_1 \exp\left(-\beta E_1\right)\left[1 + \Omega \exp\left(-\beta\ \Delta E\right)\right]\right)^N \tag{B.2}$$

The Helmholtz free energy for this system can be determined as follows,

$$\begin{aligned} F &= -k_B T \ln(Q_N) \\ &= -N k_B T \left[\ln\left(\Omega_1 \exp\left(-\beta E_1\right)\right) + \ln\left(1 + \Omega \exp\left(-\beta\ \Delta E\right)\right)\right] \end{aligned} \tag{B.3}$$

The entropy of the system can then be found as,

$$
\begin{aligned}
S &= -\frac{\partial F}{\partial T} \\
&= Nk_B \ln(\Omega_1) + Nk_B \ln(1 + \Omega \exp(-\beta\ \Delta E)) \\
&+ \frac{Nk_B \Omega \beta\ \Delta E \exp(-\beta\ \Delta E)}{1 + \Omega \exp(-\beta\ \Delta E)}
\end{aligned} \tag{B.4}
$$

and the internal energy of the system equals,

$$
\begin{aligned}
U &= F + TS \\
&= NE_1 + \frac{Nk_B \Omega \Delta E \exp(-\beta\ \Delta E)}{1 + \Omega \exp(-\beta\ \Delta E)}
\end{aligned} \tag{B.5}
$$

Finally, the specific energy of the system can be found as follows,

$$
\begin{aligned}
C_V &= \frac{\partial U}{\partial T} \\
&= \frac{Nk_B \Omega \beta^2 \Delta E^2}{(1 + \Omega \exp(-\beta \Delta E))^2}
\end{aligned} \tag{B.6}
$$